Endoscopic Optical Coherence Tomography: Design and Application

Thesis by

Jian Ren

In Partial Fulfillment of the Requirements

for the Degree of

Doctor of Philosophy

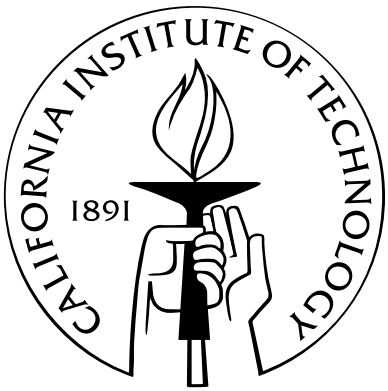

California Institute of Technology

Pasadena, California

2013

(Defended November 15, 2012)

This thesis is dedicated to my parents.

Acknowledgments

This dissertation would not have been made possible without the help, support, and encouragement from a group of amazing people who enabled me to make this labor of intellectual curiosity possible. I am fortunate to have had such a tremendous experience, both as a researcher and a professional. I am grateful to all who have helped me along the way.

My greatest appreciation goes to my advisor, Professor Changhuei Yang. I am thankful to him for introducing me to the interesting area of biomedical optical imaging. His expertise allowed me to rapidly immerse myself in this area; his vision and insight constantly inspired me in my research. More importantly, his intensive enthusiasm to the pursuit of engineering and science has always been motivating me to think creatively and act courageously.

Many other faculty members also had an impact on my work. I am indebted to Professor Mark Humayun, who was invaluable during the early stage of my research in ophthalmic imaging. He, too, frequently pointed me towards new opportunities. I would also like to thank Professor Yu-Chong Tai, Professor Azita Emami, Professor Chin-Lin Guo and Professor Hyuck Choo for being my committee and giving me many valuable suggestions.

To Jeff Brennan, who provided me both funding and access to the resources that are imperative for my research in the last two years, I give my sincere thanks. I have been greatly energized by his unmatched enthusiasm for both my dissertation and our collaboration. I am grateful for the opportunity of offering me a platform for interdisciplinary research.

And I would like to pay my heartiest thanks to my colleagues and friends at Caltech for their friendship and for the numerous technical discussions that inspired and continue to inspire my work throughout my graduate study. A far from complete list includes Qiang Lin, Jigang Wu, Xiquan Cui, Emily McDowell, Guoan Zheng, Shuo Pang, Ying Min Wang, Chao Han, Mooseok Jang. Ya-Yun Liu, Christine Garske, Agnes Tong, and Anne Sullivan have been helping me with many purchasing and administrative matters.

Finally, my deepest gratitude goes to my beloved parents, who embrace me with their endless love, patience and encouragement. Their wisdom, innocence, warmth and selflessness guided and continue to guide me out of the shadows into the sunlight of self-realization.

Abstract

This thesis presents an investigation on endoscopic optical coherence tomography (OCT). As a noninvasive imaging modality, OCT emerges as an increasingly important diagnostic tool for many clinical applications. Despite of many of its merits, such as high resolution and depth resolvability, a major limitation is the relatively shallow penetration depth in tissue (about 2∼3 mm). This is mainly due to tissue scattering and absorption. To overcome this limitation, people have been developing many different endoscopic OCT systems. By utilizing a minimally invasive endoscope, the OCT probing beam can be brought to the close vicinity of the tissue of interest and bypass the scattering of intervening tissues so that it can collect the reflected light signal from desired depth and provide a clear image representing the physiological structure of the region, which can not be disclosed by traditional OCT. In this thesis, three endoscope designs have been studied. While they rely on vastly different principles, they all converge to solve this long-standing problem.

A hand-held endoscope with manual scanning is first explored. When a user is holding a hand-held endoscope to examine samples, the movement of the device provides a natural scanning. We proposed and implemented an optical tracking system to estimate and record the trajectory of the device. By registering the OCT axial scan with the spatial information obtained from the tracking system, one can use this system to simply 'paint' a desired volume and get any arbitrary scanning pattern by manually waving the endoscope over the region of interest. The accuracy of the tracking system was measured to be about 10 microns, which is comparable to the lateral resolution of most OCT system. Targeted phantom sample and biological samples were manually scanned and the reconstructed images verified the method.

Next, we investigated a mechanical way to steer the beam in an OCT endoscope, which is termed as Paired-angle-rotation scanning (PARS). This concept was proposed by my colleague and we further developed this technology by enhancing the longevity of the device, reducing the diameter of the probe, and shrinking down the form factor of the hand-piece. Several families of probes have been designed and fabricated with various optical performances. They have been applied to different applications, including the collector channel examination for glaucoma stent implantation, and vitreous remnant detection during live animal vitrectomy.

Lastly a novel non-moving scanning method has been devised. This approach is based on the

EO effect of a KTN crystal. With Ohmic contact of the electrodes, the KTN crystal can exhibit a special mode of EO effect, termed as space-charge-controlled electro-optic effect, where the carrier electron will be injected into the material via the Ohmic contact. By applying a high voltage across the material, a linear phase profile can be built under this mode, which in turn deflects the light beam passing through. We constructed a relay telescope to adapt the KTN deflector into a bench top OCT scanning system. One of major technical challenges for this system is the strong chromatic dispersion of KTN crystal within the wavelength band of OCT system. We investigated its impact on the acquired OCT images and proposed a new approach to estimate and compensate the actual dispersion. Comparing with traditional methods, the new method is more computational efficient and accurate. Some biological samples were scanned by this KTN based system. The acquired images justified the feasibility of the usage of this system into a endoscopy setting.

My research above all aims to provide solutions to implement an OCT endoscope. As technology evolves from manual, to mechanical, and to electrical approaches, different solutions are presented. Since all have their own advantages and disadvantages, one has to determine the actual requirements and select the best fit for a specific application.

Contents

List of Figures

List of Tables

Nomenclature

CT	computed tomography
PET	positron emission tomography
OCT	optical coherence tomography
NA	numerical aperture
GRIN	gradient indexed
MRI	magnetic resonance imaging
KTN	potassium tantalate niobate
PSF	point spread function
NDT	non-destructive test
FWHM	full width half maxim
PNS	peripheral nerve stimulation
SNR	signal to noise ratio

Chapter 1

Introduction

Dependable diagnosis of diseases at their early stages is vital for providing appropriate therapeutic treatments in time. It will ultimately reshape the modern society by both improving clinical health care quality for patients and advancing fundamental understanding in life science. In the past several decades, non-invasive biomedical imaging techniques, such as X-ray computed tomography (CT) [1], positron emission tomography (PET) [2], medical ultrasonography [3], and magnetic resonance imaging (MRI) [4] pervasively played a vital role in many surgical and therapeutic procedures by aiding with image guidance [5–10].

There has been existing a significant diversification among the limitations of these techniques. Safety concerns have been widely raised and debated for PET/CT, PET/MRI, and CT[1], as they do have to expose patients to uncommonly high dose of radiation. Both the indirect ionizing radiation in the form of X-rays photon used in CT and the direct ionizing radiation in the form of positrons in are sufficiently energetic to have negative impact on cell chemical bonds, such as DNA double stand breaks [11]. These damages are occasionally not corrected properly by cellular repair mechanisms thus result in cancer [12]. The biological effects of these ionizing radiation is proportional to the absorbed energy or dose . The global average dose from natural background radiation is equal to $2.4\,mGy$ per year [13], while a typical CT can radiate $10 \sim 20\,mGy$ onto specific organs, and might increase dose to $80\,mGy$ for some specialized CT scans [14]. For PET/CT scanning, the combined dose may be significant as well, which is around $23 \sim 26\,mSv$ [15]. It can be seen that clinical exercise of such imaging approaches based on ionizing radiation needs proper justification.

Despite of the very powerful magnetic field (up to $3.0\,tesla$) deployed, MRI avoids the use of ionizing radiation. This is clinically preferable, as there is no evidence for biological harm from exposure to even very strong static magnetic fields [16]. However, MRI does prohibit some ferromagnetic object, which includes certain metallic implants, shell fragments, surgical prostheses, and ferromagnetic aneurysm clips. This is primarily because the interaction between the extremely

[1]Stand-alone PET is now very rare due to the clinical need for combining the functional images from PET and the structural images from CT or MRI.

strong magnetic field with such material can cause potential force and movement of these objects within the field and thermal damage originating from radio-frequency induction heating [17]. At the same time, peripheral nerve stimulation (PNS) is another limitation for MRI, where the rapidly switching magnetic field gradients introduces nerve stimulation that can cause a twitching sensation [18, 19].

Another practical barrier for the above imaging modalities except ultrasound is the cost of construction and maintenance of such imaging systems. For instance, the typical cost for a standard $3.0\,telsla$ MRI scanners would often be in the range of US$\$\,2 \sim 2.3$ million. Similarly, limitations to a broader clinical application of PET result from the high costs of cyclotrons, which is required for the production of short-lived radionuclides, and the special on-site chemical synthesis apparatus to provide the radiopharmaceuticals after radioisotope preparation [20].

Image resolution is of great concern when there is an attempt to disclose fine physiological structures for diagnosis purpose. Current high resolution CT has a resolution of up to $0.3 \sim 0.5\,mm$ [`SOMATOM Definition Edge™, Siemens AG`] [21], while the most state of art MRI systems have advanced to a comparable submillimeter resolution of $0.3 \sim 1\,mm$ [`MAGNETOM Trio, A Tim System™, Siemens AG` [22]. The resolution of medical ultrasound systems depends on the center frequency applied. There exists a trade-off between image resolution and penetration depth: sound waves with lower frequencies sound wave yield less resolution but can image deeper into tissue. For linear array transducers with parallel beams and a center frequency of $3 \sim 10MHz$, the typical axial resolution ranges from $0.3\,mm$ to $1.1\,mm$, while the typical lateral resolution ranges from $1.1\,mm$ to $2.8\,mm$ [23]. Therefore, when the need of disclosing some extra fine physiological structures arises, all of these above approaches will likely be incapable of providing sufficient resolving power to visualize those critical features, which are extremely important for diagnosis, surgery guidance, and treatment evaluation. For example, the squamous epithelium in the transformation zone of human cervix, which is of particular clinical interest as abnormal cell growth or dysplasia tends to begin there [24], has a $\sim 35\mu m$ thick lay structure on top of the submucosal membrane layers with a thickness of $\sim 150\,\mu m$. In the field of ophthalmology, as a promising treatment for open angle glaucoma [25], the surgery where an bypass stent is implanted into anterior chamber would be greatly improved if the collector ducts with a typical dimension of around or below $100\,\mu m$ can be visualized [26].

As an attempt to provide an alternative when facing those disadvantages of the above imaging approaches, optical coherence tomography (OCT), a non-invasive optical technique for sub-surface tissue imaging, has been proposed and implemented in the recent decades. Since its born, this method has thrived to an important clinical imaging modality. It provides some unique advantages over other imaging methods. First, OCT is capable of imaging tissue to a depth of a few millimeters [27] with up to subμm resolution [28]. Second, OCT utilizes near infrared light source with typical wavelength range from $\sim 800\,nm$ to $1300\,nm$, therefore avoids the high energy X-ray photon in CT

and the added negative ionizing radiation. The optical power required for OCT imaging is also safe enough for OCT to be used in sensitive tissue environments [29], such as human eye [30–33]. Additionally, while a standard OCT imaging apparatus is able to provide depth-resolved tomographic images, more advanced OCT imaging systems can offer extra functional information, such as tissue structural arrangement (via polarization-sensitive OCT) [34, 35], flow (via Doppler OCT) [36, 37], the spatial distribution of specific contrast agents (via molecular contrast OCT) [38, 39], and depth resolved spectral signatures (via spectral OCT) [40, 41].

1.1 History and application of OCT technology

OCT was first developed by Huang et al. in Fujimoto's group at MIT in 1991 [42]. Exhibiting *ex vivo* images of human retina and coronary arteries, this early demonstration promises a strong capability of OCT to image transparent and high scattering materials. Later in 1993, the first *in vivo* OCT images which disclosed retinal structures were published [30, 43]. Since then, OCT technique has received a rapid acceptance and attracted increasing attention of many research groups worldwide. In 1996, Carl Zeiss Meditec introduced the first commercial OCT instrument. In the recent decades, people realized that imaging in tissues, which are not as transparent as eyes, is possible with a longer wavelength which allows for reduced scattering and improved penetration [44, 45]. Thus OCT has been expanded to many clinical areas such as gynecology [46], pulmonology [47], gastroenterology [48], urology [49], and cardiology [50]. Though the first internal organs OCT imaging was demonstrated in 1997 [51], ophthalmic OCT is still the most successful application of OCT technique. Current commercial ophthalmic OCT systems are in common use for research and clinical practice. Nevertheless, the latest advance of this technology might be able to change the situation drastically.

In cardiology, current resolution and image contrast of OCT are very promising for improved characterization of coronary pathology. The potential resulted more in-depth understanding of factors associated with heart attack is very useful for the development of new therapeutic treatments. More importantly, imaging catheters have also been developed to gain minimally invasive access to the main coronary arteries. The latest Fourier-domain OCT systems with a increased imaging speeds < 100 frames per second can enable imaging long coronary artery segments following a saline injection. The clinical adoption of OCT in cardiology is expected to become more prevalent. High-speed OCT may have a significant impact on endoscopic and laparoscopic applications for early neoplastic changes surveillance as well. The high imaging acquisition can provide wide-field visualization of broad luminal surface areas to help early stage screening for focal disease. It is anticipated that this capability to noninvasively explore large tissue volumes could transform diagnosis dramatically. For example, recent research effort have been made to image human cadaver coronary plaque with

a resolution close to micrometer [52].

OCT has also played an increasingly important role in many industrial applications, which include non destructive testing (NDT) and material thickness measurements. Lately, a cross-sectional slice of the piece of art works was examined by OCT [53]. OCT provides a cross-sectional or even 3D image with no compromising on the sample. It also offers the freedom to select the depth for examination, which is superior compared to traditional techniques. OCT systems with feed-back also can be applied to control manufacturing processes by providing scanning into interiors of hard-to-reach spaces even in hostile environments, such as radioactive, cryogenic or extreme temperature. With high-speed data acquisition, or sub-micron resolution, it can be used to perform both real-time control and off-line measurement.

1.2 Overview of OCT operation

The operation principle behind OCT is analogous to that of ultrasound imaging, where acoustic waves are sent into a sample and the reflected pulsed sound echo is received and analyzed, then an axial profile for single transverse location in the sample can be generated. In OCT, optical wave is used instead. As light travels much faster than sound, the measurements for the intensity and echo time delay of light, which are back-scattered or back-reflected from various location within the imaged tissue, is achieved by optical interferometry within certain interferometer. Its depth resolving power comes from the optical coherence gating mechanism.

When low-coherence light is fed into a interferometer, the light beam will be divide into two parts by a beam splitter. The part that directed at the sample is called sample arm, containing the item of interest, the other one directed at a reference retro-reflector (such as a mirror) is called reference arm. When the two parts of beam reflected back from sample and the reference mirror, they are recombined at a beam combiner and captured by the interferometer. Then a interferogram is obtained by optical detector and analyzed to generate a depth profile (A-scan), which represents the reflectivity distribution along the light propagation direction.

By scanning the probing beam across the sample, a cross-sectional tomography (B-scan) can be acquired. 3D volumetric images can also be obtained by combining multiple cross-sections. Therefore, OCT data virtually depicts the variation in optical back scattering or back reflection in a cross-sectional plane or a volume within the imaged sample.

Based on two types of low-coherence interferometers, two main types of OCT have been developed, including time domain and frequency domain technique. They are distinct from each other by the light source and by the implementation of the interferometers.

1.2.1 Time domain OCT

The early OCT implementations [54], referred to as time domain (TD) systems, is implemented by an axially scanning mirror in the reference arm and detects all wavelengths simultaneously in a single element detector. A simple optical setup for a time domain OCT system utilizing a low coherence source and a Michelson-type interferometer is shown in Fig. 1.1.

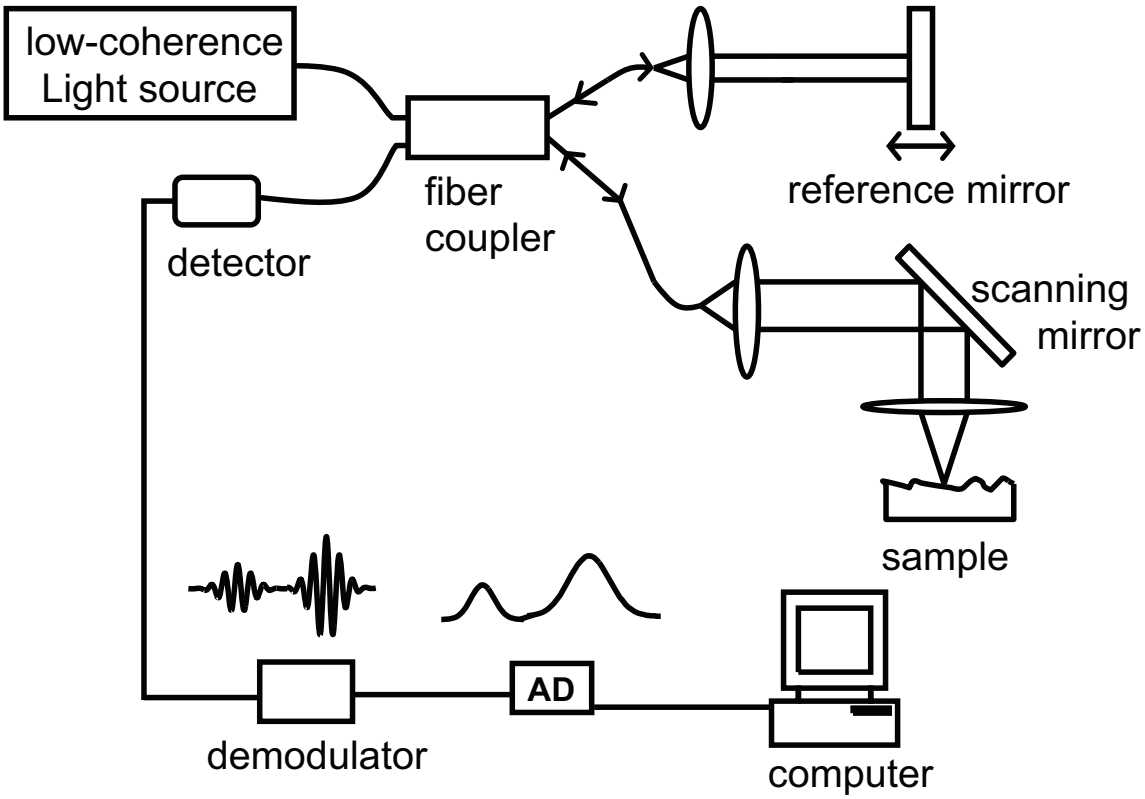

Figure 1.1: Simplified OCT system setup using a fiber based Michelson interferometer.

This system utilizes the property of low coherence interferometry: noticeable interference fringes are only generated when the path length difference is within the coherence length of the light source. The interference of the two light beams can be expressed in Eq. (1.1):

$$I_D = [R_s + R_r] + \hat{S}(\Delta x)\left[2\sqrt{R_s R_r}\cos(2\Delta x k_0)\right] \tag{1.1}$$

where Δx is the path length difference between reference and sample reflection locations; I_D is the power received at the detector; R_s and R_r are the power for sample and reference arm respectively; $\hat{S}$ is the coherent envelop function of the source; k_0 is wavenumber of the center frequency of the source. This equation shows that the output intensity from the interferometer is a function of the path length difference Δx. When the reference mirror is translated, the path length of the reference beam is scanned and yields a variable time delay. This will result in either destructive or constructive

interference at the beam combiner. Thus, the output intensity, the interferograms can be measured and recorded as Δx gets scanned. This would actually generate an auto-correlation if in a symmetric interferometer. The amplitude of the envelope varies for different path length differences, while the peak of the envelope occurs at path length matching (zero path length difference). If, otherwise, a coherent light source with long coherent length is used, the back-reflected beams will always interfere and generate an interferogram with constant amplitude. This would have revoked the ability of ranging the reflection location within the sample.

As mentioned above, when a low coherent light source is used, the interference fringes emerges onlywhen the reference and sample path lengths were matched to within the coherence length of the source. The coherence length, $l_c = 2\ln 2\lambda^2/(\pi\Delta\lambda)$, which is inversely proportional to the spectral bandwidth of the source, determines the axial resolution. One unique feature of this method is that this axial resolution is decoupled from the lateral resolution, which is otherwise determined by the sample arm collection optics.

1.2.2 Frequency domain OCT

In recent years, a new type of OCT imaging method - frequency domain OCT (FDOCT) [55, 56], also referred as Fourier domain OCT, spectral domain OCT (SDOCT) or spectral radar [57], has attracted a huge increase in attention due to significant benefit for actual biomedical application. In fact, the idea of Fourier domain OCT techniques can be traced back in 1995 [58], but the advantage of the Fourier domain technique was not broadly accepted and exploited until nearly a decade later. In 2003, several works almost simultaneously demonstrated FDOCT has several orders of magnitude improvement in system sensitivity, which includes theoretical calculation [59–61] and experimental results [62–64]. The clinical impact of this breakthrough was phenomenal because the significantly faster imaging speeds made imaging over very large tissue volume possible [65].

In Fourier domain OCT, the broadband interference is obtained by encoding the optical frequency with a spectrally scanning source or with a dispersive detector. It calculates the delay time by a Fourier transform of the interference spectrum of the light. The implementation of FDOCT is simple as the reference mirror is now immobilized. The acquired signal can be written as a function of frequency/wavenumber [2] and path length difference in Eq. (1.2).

$$I_D = [R_s + R_r] + \hat{S}(\Delta x)\left[2\sqrt{R_s R_r}\cos(2\Delta x \Delta k)\right] \tag{1.2}$$

where Δk is the wavenumber difference from the center wavenumber k. Eq. (1.2) is similar to Eq. (1.1) except Δk. One can realize that the period of the spectral oscillation of the acquired signal in k space is proportional to the path length difference Δx. A reflection comes from a location with

[2] Wavenumber is commonly used for convenience

shorter path length difference will produce a spectral oscillation with a frequency lower than that of a longer one. Hence, a Fourier transform of the spectral fringes will result in a depth profile similar to that acquried from TDOCT. A typical FDOCT system can have a signal to noise ratio (SNR) of more than $110\,dB$.

In time domain OCT, interferometric fringes are acquried by rapidly translating the reference reflector. The imaging speed is limited by the mechanical actuating of the reference mirror, which is typically below 16kHz. In contrast, Fourier domain OCT avoids the mechanical scanning of the reference arm and acquires all the reflected light from the sample simultaneously. As shown in Eq. (1.2), the optical path length difference between the scatters within sample and the reference reflections is now encoded by the frequency of the interferometric fringes. As implied in Eq. (1.2), signal resulting from all reflection can be acquired simultaneously as they are represented by different spectral oscillation frequencies. This way the reflection signal from any depth of the sample can be collected over the entire measurement time T. Therefor, FDOCT systems are intrinsically more sensitive than TDOCT systems. The SNRs for TDOCT and SDOCT can be compared for the same detector responsitivity, acquisition time, and depth scan range [59–61], as expressed in Eq. (1.3).

$$\begin{cases} \mathrm{SNR}_{TD} &= \frac{\rho T}{eN} P_{s_0} R_s \\ \mathrm{SNR}_{FD} &= \frac{\rho T}{2e} P_{s_0} R_s \end{cases} \tag{1.3}$$

where P_{s_0} is the sample arm power if the sample is fully reflective, R_s is the same sample reflectivity for both systems, ρ is the detector responsivity, e is the electron charge, N is the number of channels. From Eq. (1.3), one can clearly see the sensitive advantage of a FDOCT system over a TDOCT system is about a factor of $N/2$.

Depending on encoding the spectrum as a function of space or time, there are two varieties of FDOCT: 1) spectrometer based system [], where a grating is deployed to disperse the broadband light across a detector array, and 2) swept source OCT, also known as wavelength tuning interferometry (WTI) [66],optical frequency domain reflectometry (OFDR) [67], and optical frequency domain imaging (OFDI) [64], which uses a narrowband source rapidly tuned over a broad bandwidth to measure spectral oscillations in time with a high speed detector.

Spectral domain (SD) OCT

Spectral domain (SD) OCT [7] extracts spectral information by using a dispersive element to distributing different optical frequencies onto a detector stripe likelikes an array-type detector (Figure 2(a)). Therefore the information of the full depth scan is available within a single exposure.

However, SD-OCT systems commonly suffer from problem what is known as axial depth dependent sensitively fall off, which is not in Time domain OCT. Reflections from deeper locations will appears to be weaker reflections and the corresponding image quality will be degraded. This

disadvantage of SD-OCT reduces its ability to imaging of deep internal locations.

Swept source (SS) OCT

Swept source (SS) OCT [8] (Figure 1-2 (b)) uses a frequency tuneabletunable laser and a point source detector. It tries aims to combine some of the advantages of standard Time domain technique and Spectral domain OCT. For operation, the laser is rapidly swept across its frequency range for each sample location. Its detector records the interrference at each wavelength individually and encodes the spectrum as a function of time.

Compared to Spectral Domain OCT technology, Swept Source OCT does not suffer from inherent sensitivity degradation at longer imaging depths. Therefore, these systems are the preferred choice where long imaging depths are desired. One of the main drawbacks of the technique are is the nonlinearities in the wavelength scanning, especially at high scanning frequencies. Another main drawback is its limited axial range. By pushing the tuning sweeping speed very high, the coherence length associated with the instantaneous line-width will suffer.

1.3 Endoscopic optical coherence tomography

Endoscopy, another diagnostic imaging technique, that enables a clinician to peer through the body's passageways has long been in existence since the early 1900s [68, 69]. Endoscopy took a great leap forward in 1960s when fiber-optic endoscopes [70] were introduced. Since their inception, fiber-optic endoscopes have been used to diagnose lung cancer [71], examine the gastro-intestinal (GI) tract [72–74], inspect the interior of the colon [75–77], provide direct visualization and guide treatment of the vagina and cervix [78–80], explore the urinary tract for unusual foreign bodies and malignancies [81, 82], and evaluate the results of prostate cancer radiation therapy [83, 84]. From an operational point of view, a fiber endoscope uses a fiber-optic cable (or a bundle of glass or plastic fibers) to transfer the body cavity images. Fiber endoscopes are usually limited in transverse resolution as they can typically render at most 30,000 resolvable points. This is equivalent to a two-dimensional (2-D) image with 150×200 points. Fiber endoscopes also require the use of additional waveguides or fibers to illuminate the tissue under examination with visible light. Moreover, fiber endoscopes with a 2.0 mm biopsy channel are typically 5.9 mm in diameter (Olympus GIF-XP160 gastrointestinal videoscope). This usually limits their usage to wider body passageways such as the GI tract, colon, etc. Further, fiber endoscopes are useful only for superficial examinations as they do not offer any form of depth resolved imaging. A recently developed endoscope method, known as spectrally encoded endoscopy, uses a broadband optical source coupled with a diffraction grating via a single mode fiber [85]. The diffraction grating disperses different wavelengths angularly; these wavelengthes are then focused along a line using a front end focusing lens. This endoscope design is single-fiber-

based and may be used to create much more compact probes than other existing designs. However, depth perception is not possible in such kind of endoscopic systems.

A three-dimensional (3-D) endoscopic imaging modality that can render cross-sectional view of the internal tissue structure in the forward region ahead of the probe tip can substantially improve most forms of needle surgical procedures. This additional imaging dimension is important as it can help prevent surgical needles from perforating delicate tissue structures, such as blood vessels and nerves. In the last decade, endoscopic ultrasonography (or endosonography) has been popular among the physicians as it allows viewing real-time images of intra-abdominal organs. 2-D image slices acquired from endosonography can be manipulated to render 3-D viewing of internal structures as well. However, owing to the low spatial resolution of endoscopic ultrasound, its accuracy for imaging guided intervention, such as staging a tumor is questionable [86]. For instance, a 10 MHz, 64 element linear array, 13 mm wide ultrasound endoscopic probe offers spatial resolution of no more than 1 mm [87]. At this resolution, one can detect only moderate-sized (1 cm or larger in diameter) tumors. Further, we should note that smaller ultrasonic tips will render even poorer resolution. Endoscopic MRI that yields relatively higher spatial resolution compared to conventional MRI, CT, and endoscopic ultrasound, is another option for rather accurate 3-D imaging. However, large-size endoscopic MRI probes are required to achieve acceptable spatial resolution. For instance, 0.2 mm $\times$ 0.2 mm $\times$ 2 mm = 0.08 mm3 voxel size could be achieved by using a large (4 cm diameter loop coil) size endoscopic MRI system [88]. Notice that in addition to the large size of endoscopic MRI, which is in centimeters, the depth resolution is still in the millimeters - this defeats the purpose of the endoscope as an interventional device.

The OCT-based endoscopes are benefit from the relative ease of performing high-speed and high-resolution OCT systems. In the past decades, various types of OCT probes have been design and built with the target of specific applications. The important technical characteristics for design consideration of an OCT probe include the diameter, scanning range, field of view, speed, and flexibility. Based on their scan mode, OCT probes can be divided into two groups: side-imaging and forward-imaging probes.

The big benefit of in-vivo OCT imaging is its flexible probes and endoscopes, which is uniquely suited for non-invasively accessing to various lumens of the human body such as retina, cornea, arterial plaques, and cervical, et al.

1.3.1 Side-imaging probes

The first side-imaging OCT probe was a first reported in 1996 [10]. In Side-imaging endoscopic OCT systems [11-13], the OCT probe light is emitted from and collected at the side of the endoscope. The design of Side-imaging endoscopic OCT probe usually includes a rod mirror or prism attached to a rotation assembly, which deflect the emitted light on the side of the probe. For application,

side-imaging endoscopic OCT probes are suitable for imaging within a tubular organ.

1.3.2 Forward-imaging probes

In 1997, Boppart et al. reported 6.4 mm diameter lead zirconate titanate PZT cantilever-based handheld forward imaging instruments firstly [14]. Unlike side imaging OCT systems, forward-imaging OCT endoscopes [15-17] emit and collect light in front of the probe; the diameter are relatively larger than that of side-imaging imaging probes. For application, forward-imaging OCT probes are useful tool to provide tissue structural information forward of the catheter probe, such as for device placement or image-guided biopsy.

To date, most of the OCT endoscope/catheter systems are circumferential or side-scanning systems (2-6). By rotating the probe orientation rapidly, a cross-sectional view of the tissue can be generated. However, forward-imaging OCT endoscopic systems would be very useful in providing tissue structural information forward of the probe tip for the purpose of surgical guidance. Unlike side-imaging OCT systems, the implementation of such a forward-imaging system within a narrow probe poses very significant technological challenges, and the narrowest forward-imaging scope reported to date, without using our paired-angled rotation-scan technology, has been 2.4 mm wide, too large to fit within a surgical needle (7).

1.3.3 Penetration in blood

OCT penetration through blood is limited. This fact has been noted by researchers in the field of intravascular imaging since late 90's [89]. OCT signal attenuation by blood has been believed to be a result of the optical scattering rising from intracellular/extracellular refractive index mismatch between the cytoplasm of erythrocytes and serum for infrared light.

This belief was qualitatively verified in [90]. A reflector, as a target, was imaged by OCT in the presence of saline, blood (hematocrit [Hct], 35%), and lysed blood (Hct, 1%). As shown in Fig. 1 of the article, it was difficult to locate the reflector in presence of blood while signal intensity returned to values close to saline after the red cells were lysed. This implies that membranes or hemoglobin absorption is not the main source of near infrared attenuation by blood.

In the same work [90], OCT penetration depth in blood was investigated and quantified to be about $2\,mm$ by their experimental setup. A reflector was placed in a tubing with a diameter of $6\,mm$. The section of reflector imaged was about $2\,mm$ below inner surface of tubing. Once blood was introduced into system and circulated, OCT imaging of reflector was performed. After compounds were introduced into blood to balance the intracellular/extracellular index, an even higher contrast was achieved due to the reduced signal attenuation by scattering.

However, this result can not be regarded as an accurate estimation for OCT penetration depth

in real blood environments as it was achieved in a saline-diluted blood with an Hct of 35%. The authors stated several reasons why they did not use fresh blood. Second, the target imaged in the test was a metal reflector. One would expect a weaker signal for biological tissues like vessel wall.

A more close to practical applications but less quantitative test was carried in [89]. The impact of blood on OCT imaging, with and without saline injections, was compared. Immediately following a saline injection, nearly the entire wall of the aorta was visible. A small portion of the front was present in the image, obstructing the view of the vessel wall behind it. The second image was taken when blood filled almost half the lumen, resulting in an inability to identify the vessel wall in this region. When no saline injection was performed, the wall could only be delineated when the catheter was in direct approximation.

The most common ways to get a clear view for OCT examination in blood environment are saline flush and balloon occlusion [91, 92].

When saline flush is applied, the time span for clear OCT imaging is about 2-3 seconds [92–94] while the volume injected per bolus is about 8-10ml [92–95]. This relatively short window allows sampling of only discrete transverse segments, precluding continuous imaging of longer sections of vessel walls [92, 93]. Another problem with saline flush is that imaging during rapid variations in saline flow might produce a "wavy" appearance of the vessel wall [89]. In addition, saline delivery through the guide catheter to displace blood was inefficient for some tissue structures [94]. Several factors that influence the effectiveness of saline flush were discussed in [94].

With proximal balloon occlusion and continuous flushing, longer segments of vessel walls can be imaged. The LightLab system utilizes low pressure (0.5 atm) proximal balloon occlusion together with distal flush from the tip of the catheter. With balloon occlusion for 35 seconds and a pull-back rate of 1 mm/second, continuous imaging of a 35 mm coronary segment is possible [92]. The disadvantages for balloon occlusion are the relatively cumbersome configuration compared with current intra-vascular ultra-sound (IVUS) systems, possible transient ischemia in the territory of the artery under study, and some concerns about the local consequences of balloon inflation. Furthermore, inadequate displacement of blood can be a problem in vessels with a diameter of 3.5 mm or greater, where large bifurcations are present and in the presence of competitive flow from collaterals or bypass grafts [92].

A discussion on how to select the two different methods can be found in [89].

Since 1999, relying on saline flush or balloon occlusion, intravascular OCT imaging has been used to different applications, such as intra-arterial imaging [89] (1999), visualization of coronary atherosclerotic plaques [93] (2002), evaluation of intracoronary stenting [94] (2003), mechanical analysis of atherosclerotic plaques [95] (2004).

Saline flush or balloon occlusions have been remaining the dominating methods facilitating OCT imaging in blood environment until 2007 [91]. In a very recent review on cardiac OCT [92], several

methods were summarized, including saline flush, balloon occlusion, index matching, and replacement of blood with optically transparent hemoglobin-based blood substitute. The later two, index matching technique [90] and transparent substitute were rarely reported. Although they are potentially to be a elegant way to improve the penetration, current compounds for index matching do not increase penetration sufficiently for in vivo use, as admitted by the authors [90]. In the most recent paper (Dec 2008) reviewed here [96], saline flush was still employed to get a clear view for OCT imaging in order to investigate mechanical properties of vascular tissues.

Most reported cardiac OCT practices up to now are still using saline flush or balloon occlusion. Some other mitigation techniques have been investigated, such as index matching. Although appear to be promising, their practical applications haven't been reported yet.

A metal target, covered by 2mm deep diluted blood flow, was successfully located [90]. Without saline injection, vessel walls were able to be delineated when the catheter was in direct approximation as shown in [89]. Both of above imply there is a possibility that the forward-looking PARS probe can recognize the aortic valve in front of it while its tip is approaching to the near vicinity of the valve during a procedure of valvuloplasty.

References

[1] G. T. Herman, *Fundamentals of Computerized Tomography: Image Reconstruction from Projections*. Springer, 2009, p. 297 (cit. on p. 1).

[2] D. L. Bailey, D. W. Townsend, P. E. Valk, and M. N. Maisey, Eds., *Positron Emission Tomography: Basic Sciences*. Springer, 2005, p. 392 (cit. on p. 1).

[3] S. C. Richard, *Foundations of Biomedical Ultrasound*. Oxford University Press, 2006, p. 832 (cit. on p. 1).

[4] R. H. Hashemi, M.D., W. G. Bradley, Jr., and C. J. Lisanti, *MRI: The Basics*. Lippincott Williams & Wilkins, 2010, p. 385 (cit. on p. 1).

[5] K. T. Foley and M. M. Smith, "Image-guided spine surgery.," *Neurosurgery clinics of North America*, vol. 7, no. 2, pp. 171–86, Apr. 1996 (cit. on p. 1).

[6] R. D. Bucholz, K. R. Smith, K. A. Laycock, and L. L. McDurmont, "Three-dimensional localization: from image-guided surgery to information-guided therapy.," *Methods (San Diego, Calif.)*, vol. 25, no. 2, pp. 186–200, Oct. 2001 (cit. on p. 1).

[7] R. Ewers, K. Schicho, M. Truppe, R. Seemann, A. Reichwein, M. Figl, and A. Wagner, "Computer-aided navigation in dental implantology: 7 years of clinical experience.," *Journal of oral and maxillofacial surgery : official journal of the American Association of Oral and Maxillofacial Surgeons*, vol. 62, no. 3, pp. 329–34, Mar. 2004 (cit. on p. 1).

[8] A. H. Chan, V. Y. Fujimoto, D. E. Moore, R. T. Held, M. Paun, and S. Vaezy, "In vivo feasibility of image-guided transvaginal focused ultrasound therapy for the treatment of intracavitary fibroids.," *Fertility and sterility*, vol. 82, no. 3, pp. 723–30, Sep. 2004 (cit. on p. 1).

[9] J. T. Yap, J. P. J. Carney, N. C. Hall, and D. W. Townsend, "Image-guided cancer therapy using PET/CT.," *Cancer journal (Sudbury, Mass.)*, vol. 10, no. 4, pp. 221–33, 2004 (cit. on p. 1).

[10] J. Ricke, P. Wust, A. Stohlmann, A. Beck, C. H. Cho, M. Pech, G. Wieners, B. Spors, M. Werk, C. Rosner, E. L. Hänninen, and R. Felix, "CT-guided interstitial brachytherapy of liver malignancies alone or in combination with thermal ablation: phase I-II results of a novel technique.," *International journal of radiation oncology, biology, physics*, vol. 58, no. 5, pp. 1496–505, Apr. 2004 (cit. on p. 1).

[11] S. E. Polo and S. P. Jackson, "Dynamics of DNA damage response proteins at DNA breaks: a focus on protein modifications.," *Genes & development*, vol. 25, no. 5, pp. 409–33, Mar. 2011 (cit. on p. 1).

[12] E. J. Hall and D. J. Brenner, "Cancer risks from diagnostic radiology.," *The British journal of radiology*, vol. 81, no. 965, pp. 362–78, May 2008 (cit. on p. 1).

[13] J. M. Cuttler and M. Pollycove, "Nuclear energy and health: and the benefits of low-dose radiation hormesis.," *Dose-response : a publication of International Hormesis Society*, vol. 7, no. 1, pp. 52–89, Jan. 2009 (cit. on p. 1).

[14] D. J. Brenner and E. J. Hall, "Computed tomography–an increasing source of radiation exposure.," *The New England journal of medicine*, vol. 357, no. 22, pp. 2277–84, Nov. 2007 (cit. on p. 1).

[15] G. Brix, U. Lechel, G. Glatting, S. I. Ziegler, W. Münzing, S. P. Müller, and T. Beyer, "Radiation exposure of patients undergoing whole-body dual-modality 18F-FDG PET/CT examinations.," *Journal of nuclear medicine : official publication, Society of Nuclear Medicine*, vol. 46, no. 4, pp. 608–13, Apr. 2005 (cit. on p. 1).

[16] D. Formica and S. Silvestri, "Biological effects of exposure to magnetic resonance imaging: an overview.," *Biomedical engineering online*, vol. 3, no. 1, p. 11, Apr. 2004 (cit. on p. 1).

[17] (UCSF Medical Center), *Magnetic resonance safety policy of UCSF* (cit. on p. 2).

[18] M. S. Cohen, R. M. Weisskoff, R. R. Rzedzian, and H. L. Kantor, "Sensory stimulation by time-varying magnetic fields.," *Magnetic resonance in medicine : official journal of the Society of Magnetic Resonance in Medicine / Society of Magnetic Resonance in Medicine*, vol. 14, no. 2, pp. 409–14, May 1990 (cit. on p. 2).

[19] T. F. Budinger, H. Fischer, D. Hentschel, H. E. Reinfelder, and F. Schmitt, "Physiological effects of fast oscillating magnetic field gradients.," *Journal of computer assisted tomography*, vol. 15, no. 6, pp. 909–14, 1991 (cit. on p. 2).

[20] M. Berger, M. K. Gould, and P. G. Barnett, "The cost of positron emission tomography in six United States Veterans Affairs hospitals and two academic medical centers.," *AJR. American journal of roentgenology*, vol. 181, no. 2, pp. 359–65, Aug. 2003 (cit. on p. 2).

[21] A. Siemens, *SOMATOM Definition Edge* (cit. on p. 2).

[22] ——, *MAGNETOM Trio, A Tim System* (cit. on p. 2).

[23] G. e. díaz, *Ultrasound Physics : Main differences between Ultrasound and X-rays* (cit. on p. 2).

[24] L. A. Bappa and I. A. Yakasai, "Colposcopy: The scientific basis.," *Annals of African medicine*, vol. 12, no. 2, pp. 86–9, 2013 (cit. on p. 2).

[25] C. K. Bahler, G. T. Smedley, J. Zhou, and D. H. Johnson, "Trabecular bypass stents decrease intraocular pressure in cultured human anterior segments.," *American journal of ophthalmology*, vol. 138, no. 6, pp. 988–94, Dec. 2004 (cit. on p. 2).

[26] J. Ren, H. K. Gille, J. Wu, and C. Yang, "Ex vivo optical coherence tomography imaging of collector channels with a scanning endoscopic probe.," *Investigative ophthalmology & visual science*, vol. 52, no. 7, pp. 3921–5, Jun. 2011 (cit. on p. 2).

[27] J. Schmitt, S. Lee, and K. Yung, "An optical coherence microscope with enhanced resolving power in thick tissue," *Optics Communications*, vol. 142, no. 4-6, pp. 203–207, Oct. 1997 (cit. on p. 2).

[28] B. Povazay, K. Bizheva, A. Unterhuber, B. Hermann, H. Sattmann, A. F. Fercher, W. Drexler, A. Apolonski, W. J. Wadsworth, J. C. Knight, P. S. J. Russell, M. Vetterlein, and E. Scherzer, "Submicrometer axial resolution optical coherence tomography," EN, *Optics Letters*, vol. 27, no. 20, p. 1800, Oct. 2002 (cit. on p. 2).

[29] American National Standards Institute, *Safe Use of Lasers*, Orlando, Florida., 2000 (cit. on p. 3).

[30] E. A. Swanson, J. A. Izatt, M. R. Hee, D. Huang, C. P. Lin, J. S. Schuman, C. A. Puliafito, and J. G. Fujimoto, "In vivo retinal imaging by optical coherence tomography," EN, *Optics Letters*, vol. 18, no. 21, p. 1864, Nov. 1993 (cit. on p. 3).

[31] J. A. Izatt, M. R. Hee, and D. Huang, "High-speed In-Vivo retinal imaging with optical coherence tomography," *Investigative ophthalmology & visual science*, vol. 35, no. 4, pp. 1729–1729, 1994 (cit. on p. 3).

[32] M. R. Hee, J. A. Izatt, and E. A. Swanson, "Optical coherence tomography of the human retina," *Archives of Ophthalmology*, vol. 113, no. 3, pp. 325–332, 1995 (cit. on p. 3).

[33] A. G. Podoleanu, G. M. Dobre, D. J. Webb, and D. A. Jackson, "Simultaneous en-face imaging of two layers in the human retina by low-coherence reflectometry," EN, *Optics Letters*, vol. 22, no. 13, p. 1039, Jul. 1997 (cit. on p. 3).

[34] J. F. de Boer, T. E. Milner, M. J. C. van Gemert, and J. S. Nelson, "Two-dimensional birefringence imaging in biological tissue by polarization-sensitive optical coherence tomography," EN, *Optics Letters*, vol. 22, no. 12, p. 934, Jun. 1997 (cit. on p. 3).

[35] M. J. Everett, K. Schoenenberger, J. Colston, and L. B. Da Silva, "Birefringence characterization of biological tissue by use of optical coherence tomography," EN, *Optics Letters*, vol. 23, no. 3, p. 228, Feb. 1998 (cit. on p. 3).

[36] J. A. Izatt, M. D. Kulkarni, S. Yazdanfar, J. K. Barton, and A. J. Welch, "In vivo bidirectional color Doppler flow imaging of picoliter blood volumes using optical coherence tomography," *Optics Letters*, vol. 22, no. 18, p. 1439, Sep. 1997 (cit. on p. 3).

[37] S. Yazdanfar, A. M. Rollins, and J. A. Izatt, "Imaging and velocimetry of the human retinal circulation with color Doppler optical coherence tomography," *Optics Letters*, vol. 25, no. 19, p. 1448, Oct. 2000 (cit. on p. 3).

[38] K. D. Rao, M. A. Choma, S. Yazdanfar, A. M. Rollins, and J. A. Izatt, "Molecular contrast in optical coherence tomography by use of a pump probe technique," EN, *Optics Letters*, vol. 28, no. 5, p. 340, Mar. 2003 (cit. on p. 3).

[39] C. Yang, "Molecular Contrast Optical Coherence Tomography: A Review," *Photochemistry and Photobiology*, vol. 81, no. 2, p. 215, 2005 (cit. on p. 3).

[40] U. Morgner, W. Drexler, F. X. Kärtner, X. D. Li, C. Pitris, E. P. Ippen, and J. G. Fujimoto, "Spectroscopic optical coherence tomography," *Optics Letters*, vol. 25, no. 2, p. 111, Jan. 2000 (cit. on p. 3).

[41] R. Leitgeb, M. Wojtkowski, A. Kowalczyk, C. K. Hitzenberger, M. Sticker, and A. F. Fercher, "Spectral measurement of absorption by spectroscopic frequency-domain optical coherence tomography," *Optics Letters*, vol. 25, no. 11, p. 820, Jun. 2000 (cit. on p. 3).

[42] D. Huang, E. Swanson, C. Lin, J. Schuman, W. Stinson, W. Chang, M. Hee, T. Flotte, K. Gregory, C. Puliafito, and A. Et, "Optical coherence tomography," *Science*, vol. 254, no. 5035, pp. 1178–1181, Nov. 1991 (cit. on p. 3).

[43] A. F. Fercher, C. K. Hitzenberger, W. Drexler, G. Kamp, and H. Sattmann, "In vivo optical coherence tomography.," *American journal of ophthalmology*, vol. 116, no. 1, pp. 113–4, Jul. 1993 (cit. on p. 3).

[44] J. M. Schmitt, A. Knüttel, M. Yadlowsky, and M. A. Eckhaus, "Optical-coherence tomography of a dense tissue: statistics of attenuation and backscattering.," *Physics in medicine and biology*, vol. 39, no. 10, pp. 1705–20, Oct. 1994 (cit. on p. 3).

[45] J. G. Fujimoto, M. E. Brezinski, G. J. Tearney, S. A. Boppart, B. Bouma, M. R. Hee, J. F. Southern, and E. A. Swanson, "Optical biopsy and imaging using optical coherence tomography.," *Nature medicine*, vol. 1, no. 9, pp. 970–2, Sep. 1995 (cit. on p. 3).

[46] J. Gallwas, R. Gaschler, H. Stepp, K. Friese, and C. Dannecker, "3D optical coherence tomography of cervical intraepithelial neoplasia–early experience and some pitfalls.," *European journal of gynaecological oncology*, vol. 33, no. 1, pp. 37–41, Jan. 2012 (cit. on p. 3).

[47] R. Hou, T. Le, S. D. Murgu, Z. Chen, and M. Brenner, "Recent advances in optical coherence tomography for the diagnoses of lung disorders.," *Expert review of respiratory medicine*, vol. 5, no. 5, pp. 711–24, Oct. 2011 (cit. on p. 3).

[48] E. Osiac, A. Săftoiu, D. I. Gheonea, I. Mandrila, and R. Angelescu, "Optical coherence tomography and Doppler optical coherence tomography in the gastrointestinal tract.," *World journal of gastroenterology : WJG*, vol. 17, no. 1, pp. 15–20, Jan. 2011 (cit. on p. 3).

[49] H. Wang, W. Kang, H. Zhu, G. MacLennan, and A. M. Rollins, "Three-dimensional imaging of ureter with endoscopic optical coherence tomography.," *Urology*, vol. 77, no. 5, pp. 1254–8, May 2011 (cit. on p. 3).

[50] G. J. Tearney, K. Jang, and B. E. Bouma, "Optical coherence tomography for imaging the vulnerable plaque.," *Journal of biomedical optics*, vol. 11, no. 2, p. 021 002, 2006 (cit. on p. 3).

[51] G. J. Tearney, M. E. Brezinski, B. E. Bouma, S. A. Boppart, C. Pitris, J. F. Southern, and J. G. Fujimoto, "In vivo endoscopic optical biopsy with optical coherence tomography.," *Science (New York, N.Y.)*, vol. 276, no. 5321, pp. 2037–9, Jun. 1997 (cit. on p. 3).

[52] L. Liu, J. A. Gardecki, S. K. Nadkarni, J. D. Toussaint, Y. Yagi, B. E. Bouma, and G. J. Tearney, "Imaging the subcellular structure of human coronary atherosclerosis using micro-optical coherence tomography.," *Nature medicine*, vol. 17, no. 8, pp. 1010–4, Aug. 2011 (cit. on p. 4).

[53] H. Liang, M. Sax, D. Saunders, and M. Tite, "Optical Coherence Tomography for the non-invasive investigation of the microstructure of ancient Egyptian faience," *Journal of Archaeological Science*, vol. 39, no. 12, pp. 3683–3690, Dec. 2012 (cit. on p. 4).

[54] J. Schmitt, "Optical coherence tomography (OCT): a review," *IEEE Journal of Selected Topics in Quantum Electronics*, vol. 5, no. 4, pp. 1205–1215, 1999 (cit. on p. 5).

[55] M. Wojtkowski, R. Leitgeb, A. Kowalczyk, T. Bajraszewski, and A. F. Fercher, "In vivo human retinal imaging by Fourier domain optical coherence tomography.," *Journal of biomedical optics*, vol. 7, no. 3, pp. 457–63, Jul. 2002 (cit. on p. 6).

[56] M. Wojtkowski, V. J. Srinivasan, T. H. Ko, J. G. Fujimoto, A. Kowalczyk, and J. S. Duker, "Ultrahigh-resolution, high-speed, Fourier domain optical coherence tomography and methods for dispersion compensation," *Optics Express*, vol. 12, no. 11, p. 2404, May 2004 (cit. on p. 6).

[57] G. Ha Usler and M. W. Lindner, ""Coherence radar" and "spectral radar"-new tools for dermatological diagnosis.," *Journal of biomedical optics*, vol. 3, no. 1, pp. 21–31, Jan. 1998 (cit. on p. 6).

[58] A. F. Fercher, C. K. Hitzenberger, G. Kamp, and S. Y. El-Zaiat, "Measurement of intraocular distances by backscattering spectral interferometry," *Optics Communications*, vol. 117, no. 1–2, pp. 43–48, May 1995 (cit. on p. 6).

[59] M. Choma, M. Sarunic, C. Yang, and J. Izatt, "Sensitivity advantage of swept source and Fourier domain optical coherence tomography," EN, *Optics Express*, vol. 11, no. 18, p. 2183, Sep. 2003 (cit. on pp. 6, 7).

[60] J. F. de Boer, B. Cense, B. H. Park, M. C. Pierce, G. J. Tearney, and B. E. Bouma, "Improved signal-to-noise ratio in spectral-domain compared with time-domain optical coherence tomography," EN, *Optics Letters*, vol. 28, no. 21, p. 2067, Nov. 2003 (cit. on pp. 6, 7).

[61] R. Leitgeb, C. Hitzenberger, and A. Fercher, "Performance of fourier domain vs time domain optical coherence tomography," EN, *Optics Express*, vol. 11, no. 8, p. 889, Apr. 2003 (cit. on pp. 6, 7).

[62] M. Wojtkowski, T. Bajraszewski, P. Targowski, and A. Kowalczyk, "Real-time in vivo imaging by high-speed spectral optical coherence tomography," EN, *Optics Letters*, vol. 28, no. 19, p. 1745, Oct. 2003 (cit. on p. 6).

[63] S. Yun, G. Tearney, B. Bouma, B. Park, and J. de Boer, "High-speed spectral-domain optical coherence tomography at 13 μm wavelength," EN, *Optics Express*, vol. 11, no. 26, p. 3598, Dec. 2003 (cit. on p. 6).

[64] S. Yun, G. Tearney, J. de Boer, N. Iftimia, and B. Bouma, "High-speed optical frequency-domain imaging," EN, *Optics Express*, vol. 11, no. 22, p. 2953, Nov. 2003 (cit. on pp. 6, 7).

[65] S. H. Yun, G. J. Tearney, B. J. Vakoc, M. Shishkov, W. Y. Oh, A. E. Desjardins, M. J. Suter, R. C. Chan, J. A. Evans, K. Jang, N. S. Nishioka, J. F. de Boer, and B. E. Bouma, "Comprehensive volumetric optical microscopy in vivo.," *Nature medicine*, vol. 12, no. 12, pp. 1429–33, Dec. 2006 (cit. on p. 6).

[66] F. Lexer, C. K. Hitzenberger, A. F. Fercher, and M. Kulhavy, "Wavelength-tuning interferometry of intraocular distances," *Applied Optics*, vol. 36, no. 25, p. 6548, Sep. 1997 (cit. on p. 7).

[67] B. Golubovic, B. E. Bouma, G. J. Tearney, and J. G. Fujimoto, "Optical frequency-domain reflectometry using rapid wavelength tuning of a Cr^4+:forsterite laser," *Optics Letters*, vol. 22, no. 22, p. 1704, Nov. 1997 (cit. on p. 7).

[68] Kelling and G, "Endoscopy of the oesophagus and stomach," *Lancet*, vol. 1, pp. 1189–1198, 1900 (cit. on p. 8).

[69] Killian and G, "On direct endoscopy of the upper air passages and oesophagus : Its diagnostic and therapeutic value in the search for and removal of foreign bodies," *British Medical Journal*, vol. 1902, pp. 569–571, 1902 (cit. on p. 8).

[70] WALLACE and FJ, "FIBER OPTIC ENDOSCOPY," *Journal of Urology*, vol. 90, no. 3, 1963 (cit. on p. 8).

[71] S. Lam, C. MacAulay, J. C. LeRiche, and B. Palcic, "Detection and localization of early lung cancer by fluorescence bronchoscopy.," *Cancer*, vol. 89, no. 11 Suppl, pp. 2468–73, Dec. 2000 (cit. on p. 8).

[72] Schindler and R, "Gastroscopy," *Lancet*, vol. 1, pp. 1361–1361, 1938 (cit. on p. 8).

[73] D. C. Cumberland, "Fibre-optic endoscopy and radiology in the investigation of the ipper gastrointestinatract.," *Clinical radiology*, vol. 26, no. 2, pp. 223–36, Apr. 1975 (cit. on p. 8).

[74] H. Zeng, A. Weiss, R. Cline, and C. E. MacAulay, "Real-time endoscopic fluorescence imaging for early cancer detection in the gastrointestinal tract," *Bioimaging*, vol. 6, no. 4, pp. 151–165, Dec. 1998 (cit. on p. 8).

[75] J. D. Rogge, M. F. Elmore, S. J. Mahoney, E. D. Brown, F. P. Troiano, D. R. Wagner, D. J. Black, and D. C. Pound, "Low-cost, office-based, screening colonoscopy.," *The American journal of gastroenterology*, vol. 89, no. 10, pp. 1775–80, Oct. 1994 (cit. on p. 8).

[76] A. D. Müller and A. Sonnenberg, "Protection by endoscopy against death from colorectal cancer. A case-control study among veterans.," *Archives of internal medicine*, vol. 155, no. 16, pp. 1741–8, Sep. 1995 (cit. on p. 8).

[77] D. K. Rex, "Colonoscopy: a review of its yield for cancers and adenomas by indication.," *The American journal of gastroenterology*, vol. 90, no. 3, pp. 353–65, Mar. 1995 (cit. on p. 8).

[78] F. C. Menken, "[Micro-endoscopy of the uterine cervix (author's transl)].," *Geburtshilfe und Frauenheilkunde*, vol. 41, no. 3, pp. 192–3, Mar. 1981 (cit. on p. 8).

[79] A. L. Magos, N. Bournas, R. Sinha, L. Lo, and R. E. Richardson, "Transvaginal endoscopic oophorectomy.," *American journal of obstetrics and gynecology*, vol. 172, no. 1 Pt 1, pp. 123–4, Jan. 1995 (cit. on p. 8).

[80] J. Donnez and M. Nisolle, "Endoscopic laser treatment of uterine malformations.," *Human reproduction (Oxford, England)*, vol. 12, no. 7, pp. 1381–7, Jul. 1997 (cit. on p. 8).

[81] R. I. Schnall, H. M. Baer, and E. J. Seidmon, "Endoscopy for removal of unusual foreign bodies in urethra and bladder.," *Urology*, vol. 34, no. 1, pp. 33–5, Jul. 1989 (cit. on p. 8).

[82] M. Grasso, M. Fraiman, and M. Levine, "Ureteropyeloscopic diagnosis and treatment of upper urinary tract urothelial malignancies.," *Urology*, vol. 54, no. 2, pp. 240–6, Aug. 1999 (cit. on p. 8).

[83] L. S. Marks, "Serial endoscopy following visual laser ablation of prostate (VLAP)," *Urology*, vol. 42, no. 1, pp. 66–71, Jul. 1993 (cit. on p. 8).

[84] E. M. Moore, T. J. Magrino, and P. A. Johnstone, "Rectal bleeding after radiation therapy for prostate cancer: endoscopic evaluation.," *Radiology*, vol. 217, no. 1, pp. 215–8, Oct. 2000 (cit. on p. 8).

[85] G. J. Tearney, M. Shishkov, and B. E. Bouma, "Spectrally encoded miniature endoscopy.," *Optics letters*, vol. 27, no. 6, pp. 412–4, Mar. 2002 (cit. on p. 8).

[86] J. F. Botet, C. J. Lightdale, A. G. Zauber, H. Gerdes, C. Urmacher, and M. F. Brennan, "Preoperative staging of esophageal cancer: comparison of endoscopic US and dynamic CT.," *Radiology*, vol. 181, no. 2, pp. 419–25, Nov. 1991 (cit. on p. 9).

[87] E. P. Dimagno, P. T. Regan, J. E. Clain, E. M. James, and J. L. Buxton, "Human endoscopic ultrasonography.," *Gastroenterology*, vol. 83, no. 4, pp. 824–9, Oct. 1982 (cit. on p. 9).

[88] I. Yamada, N. Saito, K. Takeshita, N. Yoshino, A. Tetsumura, J. Kumagai, and H. Shibuya, "Early gastric carcinoma: evaluation with high-spatial-resolution MR imaging in vitro.," *Radiology*, vol. 220, no. 1, pp. 115–21, Jul. 2001 (cit. on p. 9).

[89] J. G. Fujimoto, S. A. Boppart, G. J. Tearney, B. E. Bouma, C. Pitris, and M. E. Brezinski, "High resolution in vivo intra-arterial imaging with optical coherence tomography.," *Heart (British Cardiac Society)*, vol. 82, no. 2, pp. 128–33, Aug. 1999 (cit. on pp. 10–12).

[90] M. Brezinski, K. Saunders, C. Jesser, X. Li, and J. Fujimoto, "Index matching to improve optical coherence tomography imaging through blood.," *Circulation*, vol. 103, no. 15, pp. 1999–2003, Apr. 2001 (cit. on pp. 10, 12).

[91] A. M. Zysk, F. T. Nguyen, A. L. Oldenburg, D. L. Marks, and S. A. Boppart, "Optical coherence tomography: a review of clinical development from bench to bedside.," *Journal of biomedical optics*, vol. 12, no. 5, p. 051 403, 2007 (cit. on p. 11).

[92] O. C. Raffel, T. Akasaka, and I.-K. Jang, "Cardiac optical coherence tomography.," *Heart (British Cardiac Society)*, vol. 94, no. 9, pp. 1200–10, Sep. 2008 (cit. on p. 11).

[93] K. Jang, B. E. Bouma, D.-H. Kang, S.-J. Park, S.-W. Park, B. Seung, K.-B. Choi, M. Shishkov, K. Schlendorf, E. Pomerantsev, S. L. Houser, H. T. Aretz, and G. J. Tearney, "Visualization of coronary atherosclerotic plaques in patients using optical coherence tomography: comparison with intravascular ultrasound.," *Journal of the American College of Cardiology*, vol. 39, no. 4, pp. 604–9, Feb. 2002 (cit. on p. 11).

[94] B. E. Bouma, G. J. Tearney, H. Yabushita, M. Shishkov, C. R. Kauffman, D. DeJoseph Gauthier, B. D. MacNeill, S. L. Houser, H. T. Aretz, E. F. Halpern, and I.-K. Jang, "Evaluation of intracoronary stenting by intravascular optical coherence tomography.," *Heart (British Cardiac Society)*, vol. 89, no. 3, pp. 317–20, Mar. 2003 (cit. on p. 11).

[95] A. H. Chau, R. C. Chan, M. Shishkov, B. MacNeill, N. Iftimia, G. J. Tearney, R. D. Kamm, B. E. Bouma, and M. R. Kaazempur-Mofrad, "Mechanical analysis of atherosclerotic plaques based on optical coherence tomography.," *Annals of biomedical engineering*, vol. 32, no. 11, pp. 1494–503, Nov. 2004 (cit. on p. 11).

[96] R. Karimi, T. Zhu, B. E. Bouma, and M. R. K. Mofrad, "Estimation of nonlinear mechanical properties of vascular tissues via elastography.," *Cardiovascular engineering (Dordrecht, Netherlands)*, vol. 8, no. 4, pp. 191–202, Dec. 2008 (cit. on p. 12).

Chapter 2

Optical Coherence Tomography Probe I - Manual Scanning

Optical Coherence Tomography's (OCT) non-invasive nature and high resolution has made it an important modality in the field of biomedical imaging since 90's [1]. Aside from ophthalmology applications [2, 3], OCT has been implemented in various probes and endoscopic formats for various applications [4, 5]. Various methods for sweeping the OCT probe beam to accomplish scans have been developed over the years and almost all of them involve some form of mechanical actuations. While these systems allow for good scan controls and result in excellently rendered OCT images, they do come with the associated cost of additional hardware that need to be integrated well onto the probes. A hand-held OCT probe that can be manually swept over the region of interest by the user and that provides an OCT scan of the biological structures along the device's motion trajectory, can potentially simplify the whole procedure of image acquisition.

In this chapter, we report a new OCT probe design based on position tracking to achieve the above manual-scanning capability. We developed an optical monitoring system can continuously track the position and orientation (henceforth referred to as the pose) of a simple OCT probe while the probe is manually scanned over a region of interest. Both planar 2D images and volumetric 3D images could be reconstructed by orienting each OCT depth scan (A-scan) according to their individual spatial location and direction as resolved from the poses of the hand-held device. Unlike mechanically actuated OCT probes that reconstruct images based on pre-determined scan patterns [6–13], this method can objectively track and measure the real scan pattern regardless of the scanning mechanism or pattern.

2.1 Hand-Held manual scanning probe by position tracking

One possible way to acquire images is to build a non-scanning probe acquiring A lines in forward direction and surgeons can wave this probe cross the region of interest. If we can track the position

information of the probe, that can be combined with A line data to create OCT images. This idea is illustrated in the following figure:

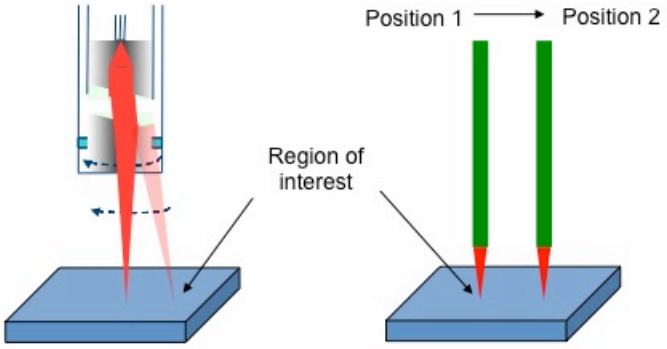

Figure 2.1: Illustration of mechanical and manual scanning

However, challenges are still left. As shown in Figure 2.2, non-uniformity and uncertainty of hand motion will significantly distort the acquired images since the spatial sampling of OCT axial scans can not maintain uniform. Therefore if there is not external mechanism to restore the hand motion information, one cannot recover the structure under test.

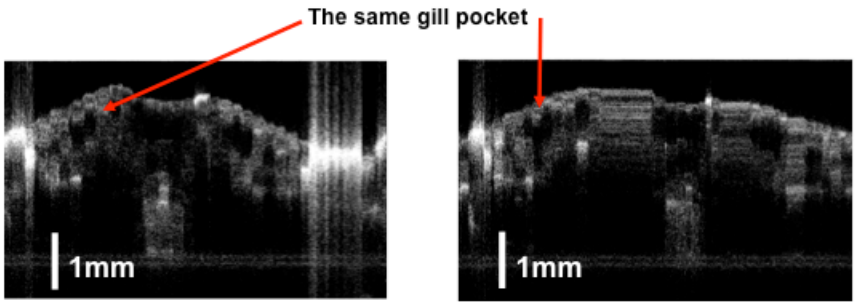

Figure 2.2: Image artifact induced by non-uniformity of hand motion.

The new design concept has three major advantages. First, the construction of such an OCT probe can be fairly simple since the user will provide the actuation force; the low associated fabrication cost is advantageous for applications that call for disposable probes. Second, the absence of a mechanical actuation system allows for very lightweight OCT probe designs; the user can thereby achieve greater control finesse during probe usage. Third, this design has significant flexibility as it allows the user to manually scan the region of his/her interest along almost any arbitrary pattern he/she desires, as long as the trajectory of the device is within the tracking frame of the monitoring system.

2.2 Implementation and verification

The implemented tracking system is schematically illustrated in Figure 2.3. Four infrared LEDs centered at 950 nm were mounted on a tetrahedron frame to serve as feature points. Taking one of the LEDs as the origin of the reference frame, the coordinates for these feature points were (0, 0, 0), (43mm, 0, 0), (0, 43mm, 0), (0, 0, 43mm) respectively. An OCT needle probe was attached to this frame along the direction of (-1, -1, -1). A monochrome CMOS camera with a focal length of 25.4mm was placed about 51cm away from the hand-held probe. Its frame rate was configured at 30fps with a pixel array of 1280 by 1024. The sensor pixel size is 5.2 microns. With this optical arrangement, a plane 51 cm from the camera was recorded with a magnification factor of 0.05 and the achieved field-of-view was 13.3cm by 10.6cm. The camera captured 2D images of the feature points. The positions of these four feature points in the recorded images provide sufficient information for the determination of the probe's pose in 3D.

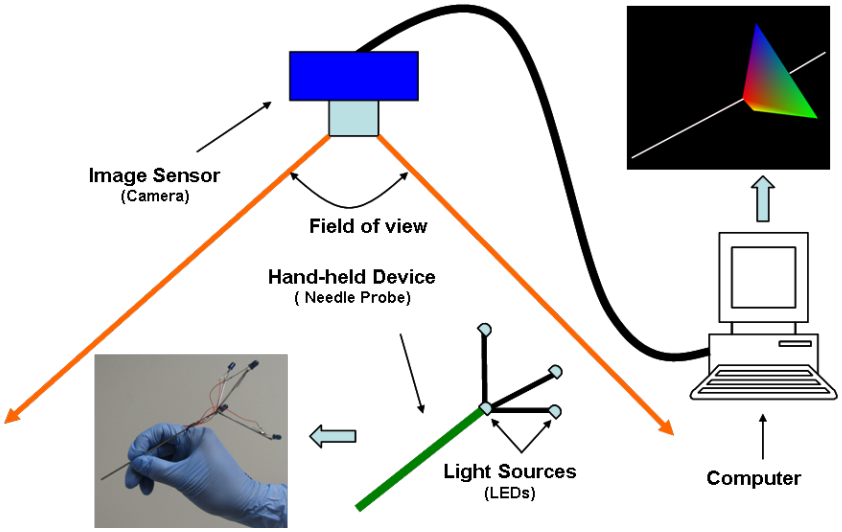

Figure 2.3: Schematic of the tracking system. The left bottom inset is a photo of our prototype hand-held probe. The right top inset is a 3D rendering of the probe by the tracking system.

In the first stage of pose determination, we employ a pair of blob detector and tracker programs to locate the feature points in each image and track their correspondence among a sequence of images. We then determine each feature point's location with sub-pixel resolution (0.03 pixels) by applying a centroid-based estimation algorithm in a surrounding square region after the center of the feature point has been approximately identified by the programs. The choice of the selected region size will ultimately impact on the achieved accuracy of the pose computation. Our evaluation experiments (described later in this paper) led us to choose a 21 x 21 pixel grid for optimal operation.

Next, we employed a pose estimation algorithm known as Pose from Orthography and Scaling with ITerations (POSIT)[14] to compute the pose. The POSIT algorithm was chosen for its fast con-

vergence. The algorithm basically applies the scaled orthographic projection (SOP) to approximate the prospective projection occurring in the camera; it simplifies the task of solving a set of nonlinear equations into iteratively solving a few sets of linear equations. The tracking system allowed us to track the probe's pose at intervals limited only by the camera's frame rate of 30 fps. The workflow of the system is shown below:

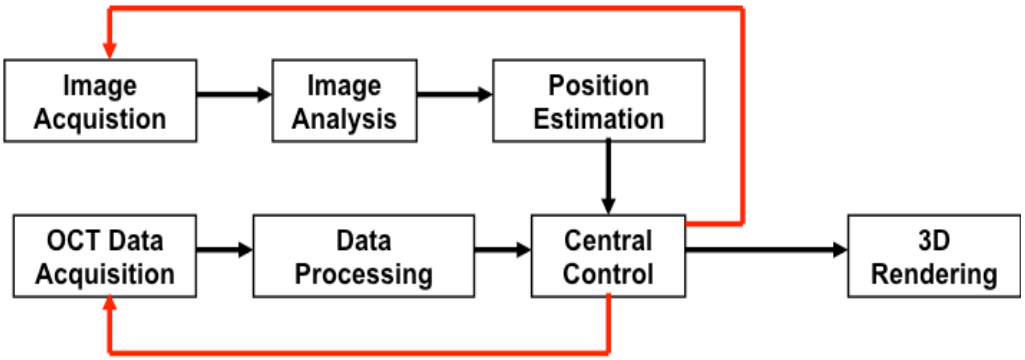

Figure 2.4: Workflow of the OCT tracking system

Our OCT probe consisted of a needle probe with a diameter of 1.2 mm and length of 63.5 mm. A 3 mm long 0.29 pitch GRIN lens connected to a single mode fiber via a glass ferrule was housed within this needle probe. This probe focused light at a working distance of 3.9 mm (in air) ahead of its tip with a spot size of 19 microns. The schematics of the probe is illustrated in Figure 2.5. A swept laser centered at 1310nm with a scan range of about 100nm and an average power of 8.5mW served as the OCT light source. The depth scan acquisition rate (A line rate) was 333 Hz. The sensitivity of this OCT probe was measured as 95dB. Concurrent with the pose tracking, our OCT probe continuously acquired A-scans and transferred the data into the computer.

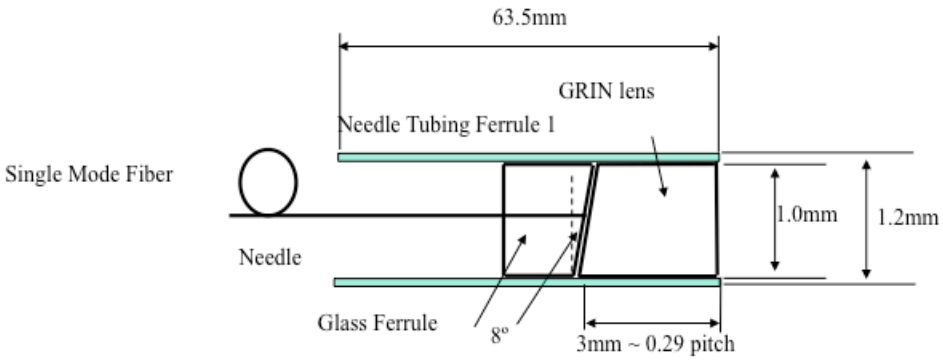

Figure 2.5: Schematics of the hand-held probe

The accuracy of our pose tracking system was examined through the following evaluation experiment. We mounted the probe onto a mechanical stage that was translated over a length of 1mm

along the scan direction (orthogonal to the OCT probe's main axis) in increments of 10 microns. At each location, a group of 100 images were captured as a sufficient statistical ensemble and analyzed for pose estimation. For each sample image, we varied the size of the selected square regions around each identified feature point from 3 x 3 to 201 x 201 pixels during feature point centroid computations.

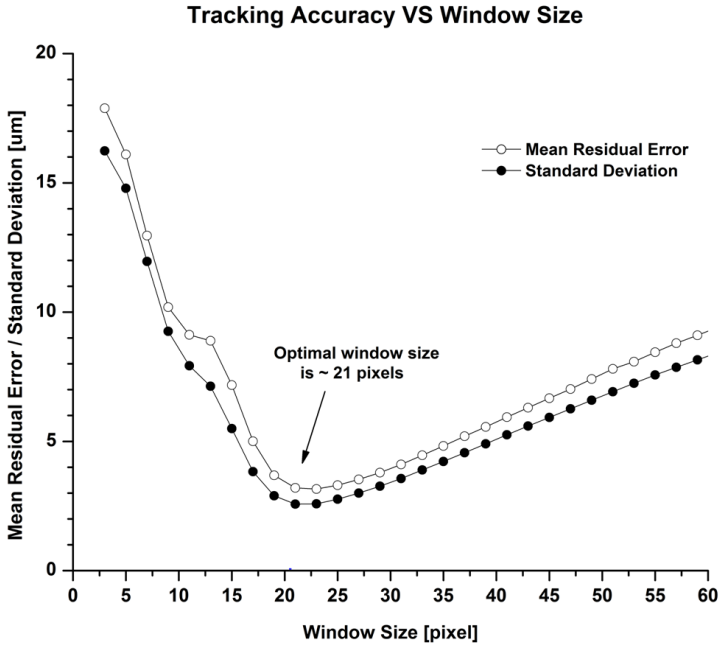

Figure 2.6: Tracking accuracy characterization

For each window size, we then computed the mean residual error and the standard deviation of the estimated displacements based on the collected data. These quantities deserve some elaborations. As the probe was translated in this experiment via a mechanical stage, its position was known at all times. We refer to the difference between this known position and the position computed by the tracking system as the residual error. The average of this error over the set of 100 images at each location is defined as the mean residual error. In effect, this quantity is a measure of the systematic positional error. The computed position varied from image frame to image frame as well, even when the probe was fixed in position. We refer to this variation as the standard deviation. In effect, this quantity is a measure of the random error associated with the measurement process. Figure 2.6 shows the behavior of these two errors (averaged over all the locations) as a function of the selected window size. We can see that both curves achieved minima at a window size of 21 pixels. This directed our window size choice for our pose estimation process. Here we define the tracking accuracy as the sum of the above two types of errors. As indicated in Figure 2.6, we were

able to determine the position of the probe with an accuracy of 5.8 microns at the optimal window size.

The existence of a sweet spot for positional accuracy is not surprising. If we choose a window size that is overly small, we will reject some of the light contribution from the feature point from the position calculation and therefore expect to introduce errors. On the other hand, an overly large window size ensures that we fully consider all light contributions associated with the feature point; however, such a choice will also assign undue weighting on spurious background signals.

We further evaluated the probe's tracking ability perpendicular to the scan direction (in other words, along the OCT probe's main axis) via a similar experiment and determined that the tracking accuracy along that axis was 18.8 μm.

2.3 Proof-of-Principle experiments

To demonstrate that this tracking approach can indeed be employed to generate reasonable OCT images, we performed a number of scans with the probe on a phantom sample. The phantom sample consisted of an agarose gel block embedded with 0.2 micron latex microspheres at 0.66% volume concentration. Two grooves were intentionally carved on its surface. They were roughly 2.5mm wide and spaced 2.2mm apart. The first groove was 1.3 mm deep and the second was 0.3 mm deep. We first translated the probe across the surface of this sample via a motorized translation stage. The collected OCT image from this scan is shown in Figure 2.7(a) and serves as the control. Next, we held the probe by hand and manually scanned the probe across the sample. This manual scan took 6 second and occurred over a length of 7.5 mm. If we simply stack the collected A-scans based on time-order, the resulting OCT image (shown in Figure 2.7(b)) corresponds poorly to our control image (Figure 2.7(a)). This is attributable to the fact that our manual scan motion exhibited significant velocity variations during the scan. In comparison, the construction of the OCT image based on accurate tracking of the probe's position did a significantly better job at rendering an accurate OCT image (Figure 2.7(c)).

It is worth to mention that the frame rate of the camera was relatively slow compared to the A line acquisition rate thus there were about 10 A lines acquired between probe pose determination. We estimated the probe position for each A line by linear interpolation from the known probe pose-time points. This interpolation might introduce some pose errors. The rendered image in Figure 7(c) contains possible maximal interpolation-induced errors of 40 microns, which can be reduced with a camera of higher frame rate.

We next applied this method to image the gill pocket structures of a 54 stage *Xenopus Laevis* tadpole, as shown in Figure 8(a). Figure 8(b) shows an uncorrected manual scan OCT image and Figure 8(c) shows a corrected version. One can see the two gill pockets at left side have apparently

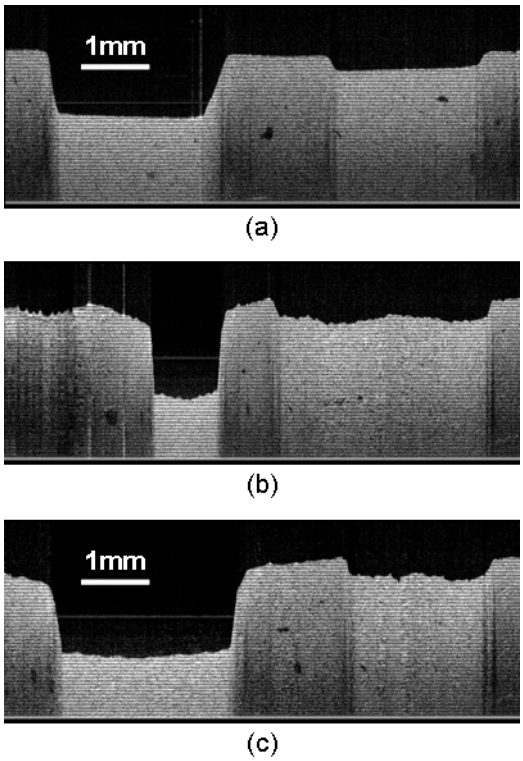

Figure 2.7: (a) Target phantom image by a motorized stage scanning (control group); (b) Target phantom image by manual scanning and reconstructed based on time order; (c) Target phantom image by manual scanning and reconstructed based on estimated displacement.

different shapes in the two images.

These experiments demonstrated that continuous pose tracking of an OCT probe is indeed useful as a means for accomplishing OCT image renderings. The position determination accuracy of 6 microns along two dimension and 19 microns along the third dimension in our prototype is a sufficiently good match with the associated resolution of the OCT system. Our proposed system can be improved by incorporating a faster frame-rate pose tracker to allow for more accurate pose tracking. Pose accuracy can also be potentially improved by employing multiple cameras at different angles to monitor the probe's movement. This tracking system approach is potentially a good match with the confined work environment of the surgical suite, as the involved tracking camera can potentially be mounted on the suite's ceiling.

Furthermore, we also tested the 3D tracking capability of the system. In the preliminary study, we did not image any sample; instead we acquired dummy axial scans and tracked the probe position while a user moving the probe in 3D. Then we placed the dummy axial scans into their corresponding positions. This way we can visualize the trajectory of the hand motion in 3D. Some of those tracked trajectories are shown below:

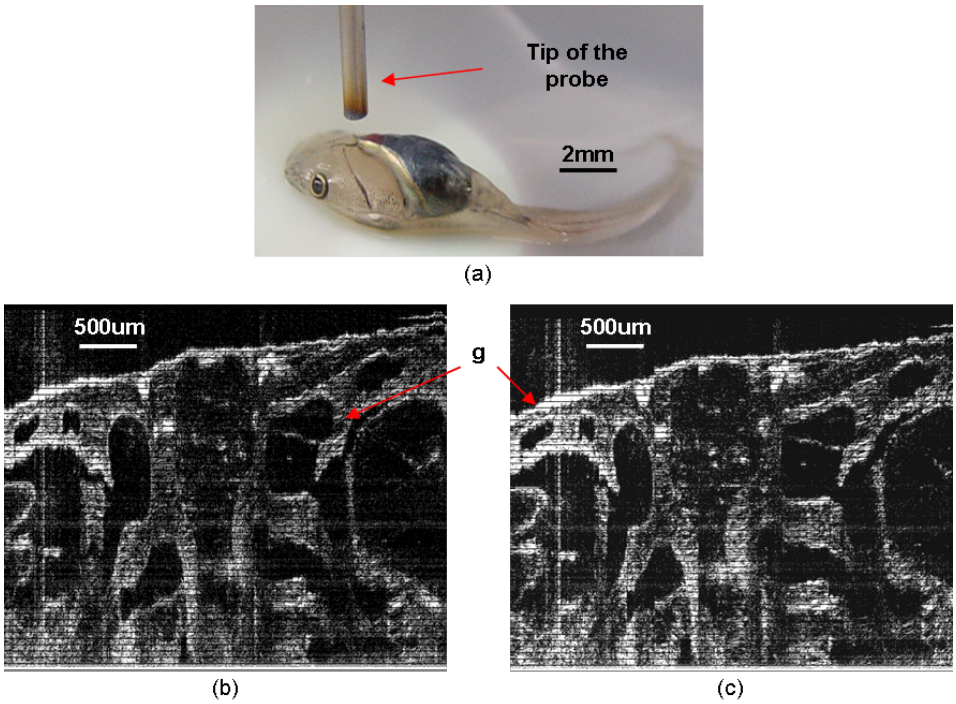

Figure 2.8: ((a) Photo of a 54 stage *Xenopus Laevis* tadpole specimen and the scanning probe's tip; (b) OCT image acquired by manually scanning without tracking correction; (c) OCT image acquired by manually scanning with tracking correction; g, gill pockets.

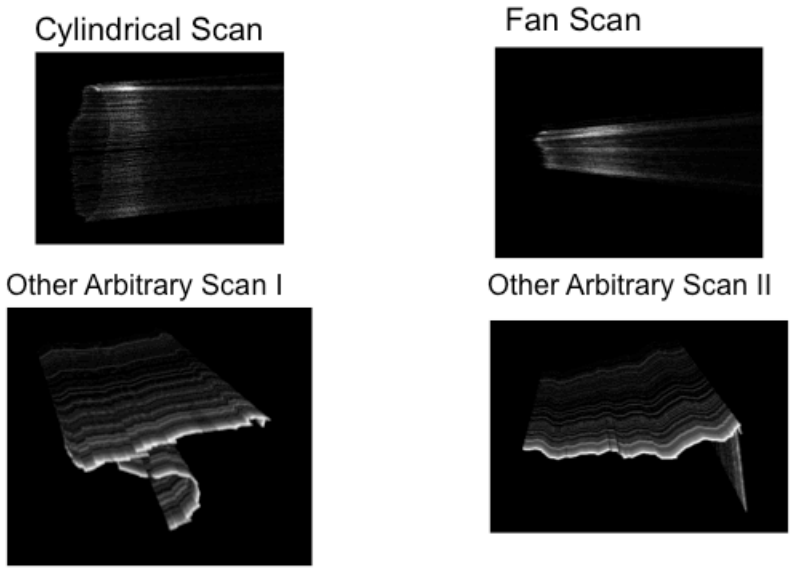

Figure 2.9: 3D scan patterns

References

[1] D. Huang, E. Swanson, C. Lin, J. Schuman, W. Stinson, W. Chang, M. Hee, T. Flotte, K. Gregory, C. Puliafito, and A. Et, "Optical coherence tomography," *Science*, vol. 254, no. 5035, pp. 1178–1181, Nov. 1991 (cit. on p. 22).

[2] B. Povazay, K. Bizheva, B. Hermann, A. Unterhuber, H. Sattmann, A. Fercher, W. Drexler, C. Schubert, P. Ahnelt, M. Mei, R. Holzwarth, W. Wadsworth, J. Knight, and P. S. J. Russell, "Enhanced visualization of choroidal vessels using ultrahigh resolution ophthalmic OCT at 1050 nm," EN, *Optics Express*, vol. 11, no. 17, p. 1980, Aug. 2003 (cit. on p. 22).

[3] S. Han, M. V. Sarunic, J. Wu, M. Humayun, and C. Yang, "Handheld forward-imaging needle endoscope for ophthalmic optical coherence tomography inspection.," *Journal of biomedical optics*, vol. 13, no. 2, p. 020 505, Jan. 2008 (cit. on p. 22).

[4] M. V. Sivak, K. Kobayashi, J. A. Izatt, A. M. Rollins, R. Ung-Runyawee, A. Chak, R. C. Wong, G. A. Isenberg, and J. Willis, "High-resolution endoscopic imaging of the GI tract using optical coherence tomography.," *Gastrointestinal endoscopy*, vol. 51, no. 4 Pt 1, pp. 474–9, Apr. 2000 (cit. on p. 22).

[5] B. E. Bouma, G. J. Tearney, H. Yabushita, M. Shishkov, C. R. Kauffman, D. DeJoseph Gauthier, B. D. MacNeill, S. L. Houser, H. T. Aretz, E. F. Halpern, and I.-K. Jang, "Evaluation of intracoronary stenting by intravascular optical coherence tomography.," *Heart (British Cardiac Society)*, vol. 89, no. 3, pp. 317–20, Mar. 2003 (cit. on p. 22).

[6] G. J. Tearney, S. A. Boppart, B. E. Bouma, M. E. Brezinski, N. J. Weissman, J. F. Southern, and J. G. Fujimoto, "Scanning single-mode fiber optic catheter-endoscope for optical coherence tomography," *Optics Letters*, vol. 21, no. 7, p. 543, Apr. 1996 (cit. on p. 22).

[7] X. Li, C. Chudoba, T. Ko, C. Pitris, and J. G. Fujimoto, "Imaging needle for optical coherence tomography," *Optics Letters*, vol. 25, no. 20, p. 1520, Oct. 2000 (cit. on p. 22).

[8] P. R. Herz, Y. Chen, A. D. Aguirre, K. Schneider, P. Hsiung, J. G. Fujimoto, K. Madden, J. Schmitt, J. Goodnow, and C. Petersen, "Micromotor endoscope catheter for in vivo, ultrahigh-resolution optical coherence tomography," *Optics Letters*, vol. 29, no. 19, p. 2261, Oct. 2004 (cit. on p. 22).

[9] J. Su, J. Zhang, L. Yu, and Z. Chen, "In vivo three-dimensional microelectromechanical endoscopic swept source optical coherence tomography," *Optics Express*, vol. 15, no. 16, p. 10 390, Aug. 2007 (cit. on p. 22).

[10] T. Xie, H. Xie, G. K. Fedder, and Y. Pan, "Endoscopic Optical Coherence Tomography with a Modified Microelectromechanical Systems Mirror for Detection of Bladder Cancers," *Applied Optics*, vol. 42, no. 31, p. 6422, Nov. 2003 (cit. on p. 22).

[11] X. Liu, M. J. Cobb, Y. Chen, M. B. Kimmey, and X. Li, "Rapid-scanning forward-imaging miniature endoscope for real-time optical coherence tomography," *Optics Letters*, vol. 29, no. 15, p. 1763, Aug. 2004 (cit. on p. 22).

[12] T. Xie, S. Guo, Z. Chen, D. Mukai, and M. Brenner, "GRIN lens rod based probe for endoscopic spectral domain optical coherence tomography with fast dynamic focus tracking," *Optics Express*, vol. 14, no. 8, p. 3238, Apr. 2006 (cit. on p. 22).

[13] J. Wu, M. Conry, C. Gu, F. Wang, Z. Yaqoob, and C. Yang, "Paired-angle-rotation scanning optical coherence tomography forward-imaging probe," *Optics Letters*, vol. 31, no. 9, p. 1265, May 2006 (cit. on p. 22).

[14] D. F. Dementhon and L. S. Davis, "Model-based object pose in 25 lines of code," *International Journal of Computer Vision*, vol. 15, no. 1-2, pp. 123–141, Jun. 1995 (cit. on p. 24).

Chapter 3

Optical Coherence Tomography Probe II - Mechanical Scanning

This chapter is to present some continuing improvement on Paired-Angle-Rotation Scanning (PARS) forward-imaging probe [1–3]. These include a more precise theoretical modeling of the scanning and a new design of 21/23 gauge hand-held probe. We will start with a short review on the PARS technology.

3.1 Paired-Angle-Rotation Scanning (PARS) Forward-Imaging Probe

Forward-imaging OCT endoscopic systems can be very useful in providing tissue structural information forward of the probe tip for the purpose of surgery guidance. Unlike side-imaging OCT systems, the implementation of such a system within a narrow probe poses very significant technological challenges. Boppart et al. [4] and Liu et al. [5] reported on two implementation approaches. The more recent report by Liu described a probe consists of an imaging fiber tip that is physically actuated by a piezoelectric cantilever. This probe is 2.4mm wide and renders relatively high quality two-dimensional scans (or B-scans). Another forward-imaging OCT probe uses 2-D microelectromechanical systems (MEMS) to scan the sample beam and hence renders 3-D OCT images [6]. However, the size of the MEMS based OCT probe has 4.3 mm diameter, which is simply too big to fit within a surgical needle. Hence, the development of a much narrower (1 mm diameter) forward-imaging needle probe with high-speed three-dimensional (3-D) imaging capability is highly desirable for IGI applications.

PARS probe is designed as a forward-imaging endoscopic probe. It features with small diameter capabilities, which is essentially only limited by the diameter of the GRIN lens available. This attributes to the design that the actuation system is located far away from the tip of the probe. At the same time, by programming the actuation mode, one can achieve different scan patterns, which

are able to provide volumetric scanning capability.

The following drawing shows the principle of a typical PARS probe.

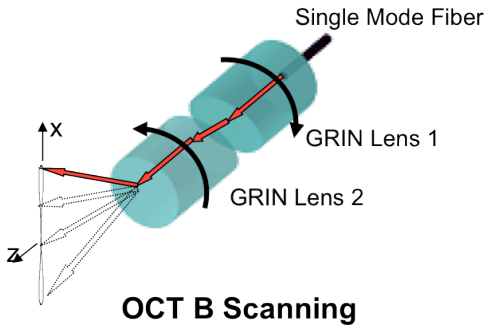

Figure 3.1: The principle of PARS scanning

As shown above, the device contains two segment of GRIN lenses. The GRIN lens 1 is connected to the delivery single mode fiber and collimates the probing beam. Its output end is angle-cut so that the exiting beam will be deflected first due to the air and glass interface. The deflected beam will then propagate a short distance (50-100 microns) before reaching the GRIN lens 2, where the second refraction occurs and the beam is future deflected. The GRIN lens 2 also works as a focusing lens so that the collimated beam will be converged to a working distance ahead of the output end of the lens. While counter-rotating both lenses, the beam can have a fan-shape scan pattern, while it is focused to the desired working distance as well.

To realize this idea, we also need to provide actuation system to provide driving torque and tubing assembly to mount the lenses. Below is a typical implementation of a PARS probe.

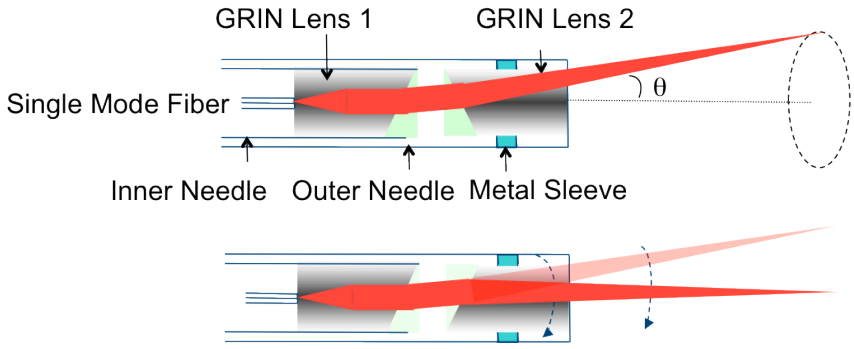

Figure 3.2: Implementation of PARS probe

As shown above, the probe consists of two needles: inner needle, which encases the first GRIN lens; outer needle, which contains the second lens. We also notice that when the two angle cut surfaces are aligned parallel, the beam will not be deflected; when they have the largest angle between them, the beam will be deflected most.

In deed, rotating two wedge prisms to steer beam in 2D have been studied. Some early works on dual wedge scanner can be traced back to 1980s [7]. Recently researchers have applied this scanner to Confocal Reflectance Microscopy [1] in the Optical Science Laboratory of Chuck DiMarzio at Northeastern University.

While the idea is similar, the key difference here is that PARS uses wedge GRIN lens instead of wedge prism, which eliminates the need for an extra lens in front of prisms to focus the beam to a desired working distance. By combining beam steering and focusing in a single miniaturized optical element, our method can potentially result in a smaller probe diameter as there is no bulky lenses necessary. The diameter is only limited by that of GRIN lens. GRIN lenses with 250 micron diameter have been commercially available.

3.2 Theoretical Modeling of PARS Scanning

Our previous study has shown that the relationship between the deflection angle and the rotation angle of the two GRIN lens are not linear. However, the old model has taken some significant simplification, such as small deflection angle approximation. The study in this section is triggered by two questions: what is the actual scan pattern of the PARS probes? And will the counter-rotating PARS scanning indeed have a line scan pattern?

To answer the above two questions, we take no approximation and strictly solve refraction within the actual geometry configurations. The following figure shows the schematics of our model calculation.

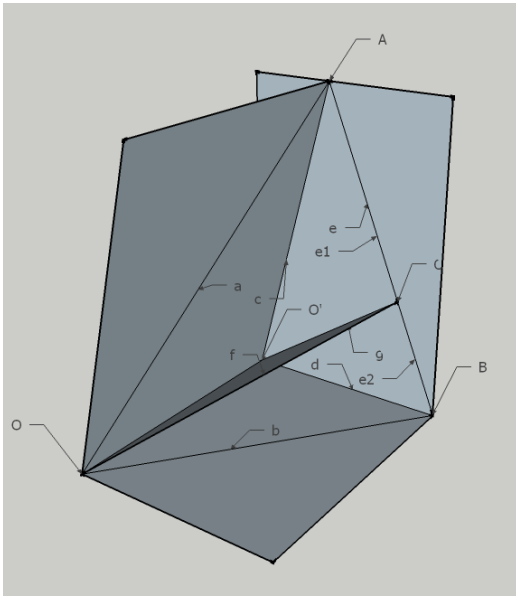

Figure 3.3: PARS scan geometric configuration

[1] http://www.ece.neu.edu/groups/osl/research-new/dwcr.html

Since the majority of light deflection occurs at the interface of the two angle-cut surfaces, we will focus our calculation onto this part only, although there exist some minor deflections at the final exit surface of the second GRIN lens. In the above figure, OO' represents the direction of optical axis, OA represents the beam direction after exiting the first GRIN lens and OB represents the surface normal of the angle cut surface of the second GRIN lens. OC then is the direction of refracted light beam after entering into the second lens. By solving all the angle and length listed in the graph, one can eventually get the angle between OC and OO'.

The derivation starts from solving the triangle O'AB, where we can compute the length of e as following:

$$e = \sqrt{\tan^2\psi - \tan^2\beta + 2\tan\psi\tan\beta\cos(\Delta\xi)} \tag{3.1}$$

We can then express the incident angle for the refraction on the angel-cut surface of the second lens as the following:

$$IncidentAngle = \cos^{-1}\left(\frac{\sec^2\psi + \sec^2\beta - \tan^2\psi - \tan^2\beta + 2\tan\psi\tan\beta\cos(\Delta\xi)}{2\sec\psi\sec\beta}\right) \tag{3.2}$$

And based on the Snell's law, the exit angel can be computed as below:

$$ExitAngle = \sin^{-1}\left(\frac{\sin(IncidentAngle)}{N}\right) \tag{3.3}$$

These angle values are planar angle inside the plane OAB. We then need to calculate the actual angle between the refracted beam direction OC and the optical axis OO'. To do this, we need to get the length of f and solve triangle OO'C. Two important angles involved are the angles between a and e, e and f. The results are shown below:

$$Angle\_ae = \sin^{-1}\left(\frac{\sin(IncidentAngle)}{e\sec\beta}\right) \tag{3.4}$$

$$Angle\_ef = \pi - (Angle\_ae + ExitAngle) \tag{3.5}$$

Now we have all the information to compute the length f, as shown below:

$$f = \frac{\sin(Angle\_ae)\sec\psi}{\sin Angle\_ef} \tag{3.6}$$

Then the angle θ between OC and OO' is presented as: $\theta = \cos^{-1}(1/f)$

Now we can continue to compute the off-plane angle ? by solving the triangle O'CB. We first need to know the lengths of g, e1, and e2.

$$g = \sqrt{f^2 - 1} \tag{3.7}$$

$$e_1 = \frac{\sin(ExitAngle)\sec\psi}{\sin(Angle\_ef)} \tag{3.8}$$

$$e_2 = e - e_1 \tag{3.9}$$

Then we are now able to calculate the angle between g and d:

$$Angle\_gd = \cos^{-1}\left(\frac{g^2 + \tan^2\beta - e_2^2}{2g\tan\beta}\right) \tag{3.10}$$

This angle is directly related to the off-plane angle ϕ, as following:

$$\phi = \xi + Angle\_gd \tag{3.11}$$

By now we have both the deflection angle θ and off-plane angle ϕ. We wrote a MATLAB code to solve this automatically so that we can sweep the rotation angle (the angle between plane OO'A and OO'B) to get a full characterization for the evolution of angle OC and OO'.

Based on this strict model, the dependence of the deflection angle and the off-plane angle on the rotation angle is plotted in the following figure with comparison to the old model.

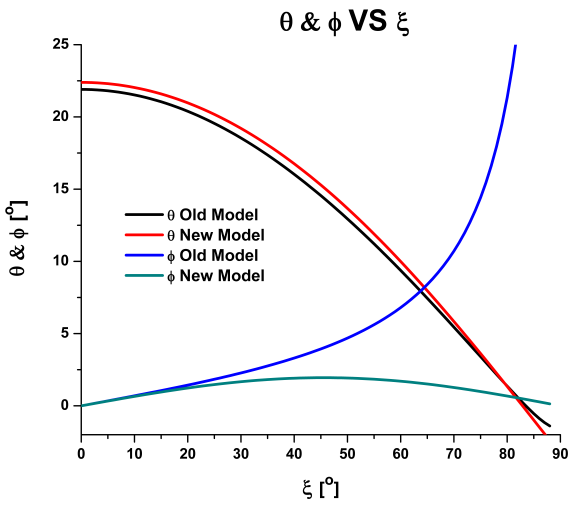

Figure 3.4: Comparison between the new and the old model

From the above plot, we can see that both model agree well with the deflection angle's dependency. However, they differ a lot on the off-plane angle's dependence. While the new model discloses that the beam deviates from the scanning plane mildly along the entire scanning range, the old model indicates that the deviation gets significantly large (over 20 degree) when the deflection

angle is small. But during all of our experiments, we have never observed large angle deviation, which suggest that the prediction of old model has considerable error. On the other hand, that of new model appears to agree with the experimental observations.

To confirm our model, we next simulated the scan pattern of counter rotating GRIN lens with ZEMAX. The simulation results of deflection angle dependency are presented in the plot below:

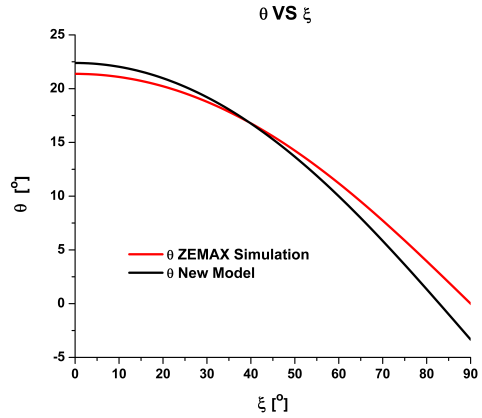

Figure 3.5: Comparison between ZEMAX simulation and the new model for deflection angle

From the above figure, we can see that the new model agrees well with the simulation in the deflection dependency. We also simulated the off-plane angle in ZEMAX, the result is shown in below.

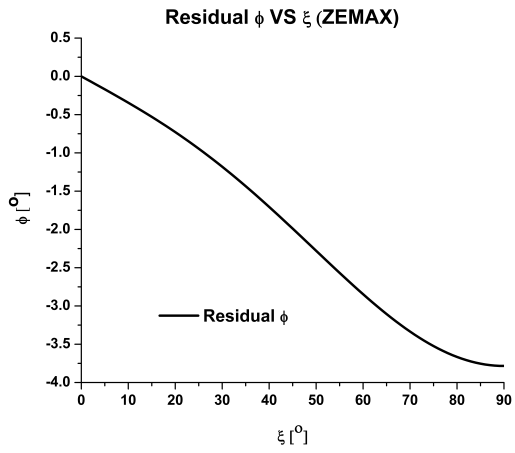

Figure 3.6: Simulated off-plane angle

Although it differs from the theoretical model, we noticed that difference is well below 5 degree, as both the model and the simulation indicate a relatively small off-plane deviation.

Finally, we compared the scan pattern on a plane perpendicular to the optical axis of the lenses.

These are shown in the following figure.

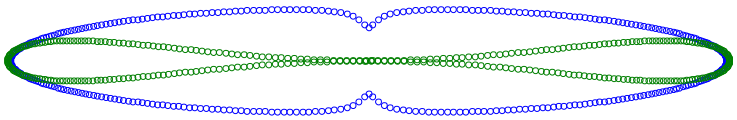

Figure 3.7: Scan pattern comparison. Blue trace is based on the old model. Green trace is based on the new model. (This figure amplified 10 times vertically to enhance the visualization of the difference)

This figure discloses that the PRAS scanning is indeed not within a single plane. And the more accurate model indicates less deviation when the deflection angle is small.

Furthermore, we proposed a simple method to experimentally measure the deflection angle dependency. This approach utilizes the inherent depth resolving capability of OCT and is now explained below:

We first place a mirror perpendicular to the probe axis and acquire an OCT image of the mirror. One of such images is shown in the following figure.

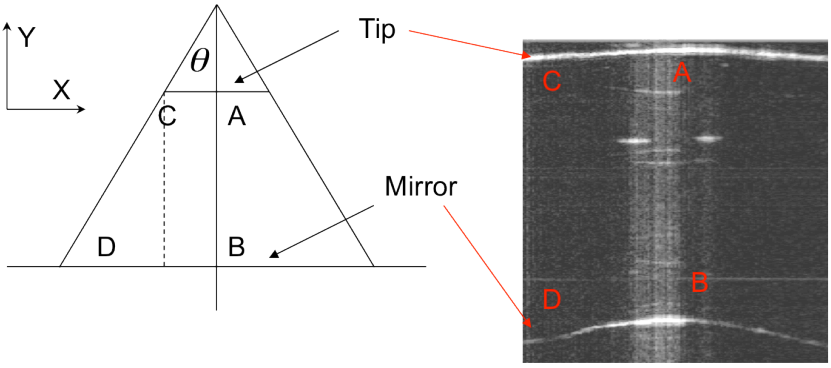

Figure 3.8: Experimental measurement of deflection angle dependency

The top bright line (AC) is caused by the tip of the probe and the bottom bright line (BD) is caused by the mirror. Although both the tip and the mirror are flat plane, they appear to be curved in the OCT image. This is due to the non-parallel scanning of the probe. This phenomenon imposes distortion on the OCT images, but on the other hand, we can make use of it since it carries the information of deflection angle.

Here we draw the geometry configuration next to the OCT image. Clearly, the axial distance between AB is shorter then CD, and the ratio of these two defines the deflection angle θ as the following equation:

$$\theta = \cos^{-1}\left(\frac{A_y - B_y}{C_y - D_y}\right) \tag{3.12}$$

Where A_y, B_y, C_y, and D_y represents the axial location of these points. And these this infor-

mation has already been carried in the OCT image. One can easily measure them from the OCT image next to it.

We have successfully implemented an algorithm to automatically detect the bright lines and measure the distance between them from OCT images. Since the lenses were rotated at a constant speed, we can plot the calculated deflection angle versus the rotation angle after a one-time calibration. Such a measurement will be presented in the next chapter.

3.3 Design and Fabrication of 21/23 Gauge Hand-held Probe

The hand-held probe consists of two major parts: the actuation system and tubing assemblies. The actuation system is responsible for driving two GRIN lens counter-rotating. The tubing assemblies are to encase the lens so that they can be mounted into the actuation system. The following figure illustrates the overall shape of the device.

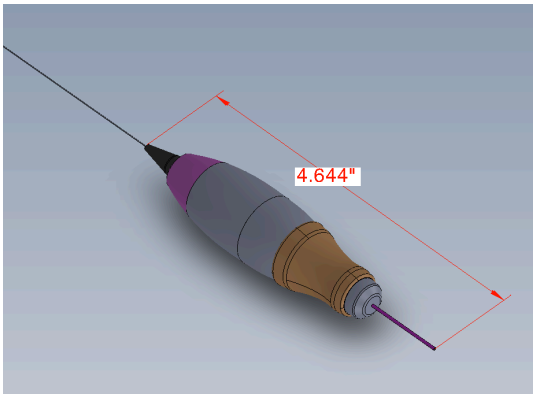

Figure 3.9: 21/23 gauge hand-held probe

3.3.1 The actuation system

The system includes a miniaturized motor, which provides the driving torque, and a set of gear to distribute the torque to the inner and outer needles. The motor we used is a 6mm diameter Micro Planetary Gear Motor. It operates at 3V DC and 40mA providing a maximum torque of 25gcm. The No-load speed is 1000rpm. While providing these performances, it weights only 2.1g and has a length of 21.4mm. These make it a very good fit for a hand-held device.

As, shown in the following figure, we employed four gears to distribute the driving torque. First, the gear on the motor shaft is connected to two other gears, among which one is bounded to the inner needle to drive the lens; the other is a compound gear that has two gears attached to a common shaft. One of the compound gears is driven by the gear on the motor shaft; the other is connected the gear on the outer needle. Because of the bridging of this compound gear, the rotation directions

for inner and outer needle are reversed.

3.3.2 The tubing assemblies

The following figure shows the overall configuration of the tube assemblies.

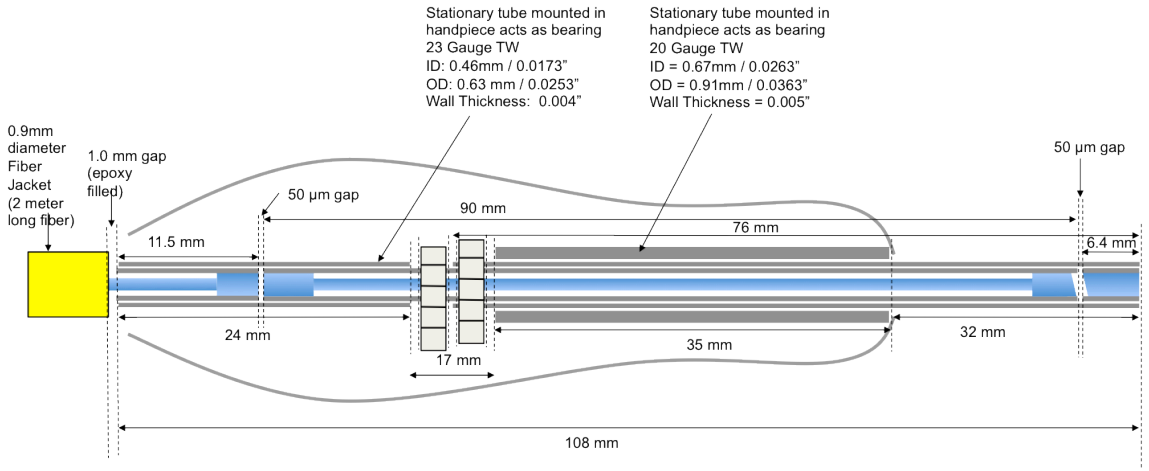

Figure 3.10: Tubing Assembly for 21/23 gauge hand-held probe

The tube assemblies include three major parts: the inner needle, the outer needle, and the rotatory jointer.

The outer needle

The structure of the outer needle is displayed below:

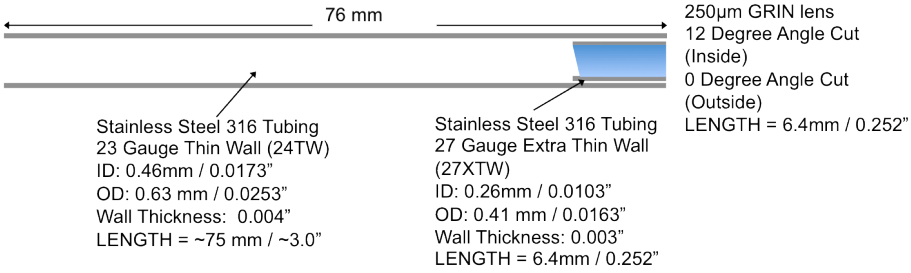

Figure 3.11: Schematics of the outer needle

The outer needle includes two stainless tubes and a GRIN lens. The short tube, as shown in the above figure as the 27 gauge extra thin wall, has a length of 6.4mm to encase the GRIN lens that has the same length. The outer end of lens is flat, the inner end has a 12 degree angle cut to achieve the desired deflection. After the lens is encased into the short tubing sleeve, they will be glued together to form a compound piece. The long tube is a 23 gauge thin wall tubing with

a length of 76mm. The compound piece is then inserted into the long tube and glued together to finish the construction of the outer needle.

The inner needle

The structure of the inner needle is shown below:

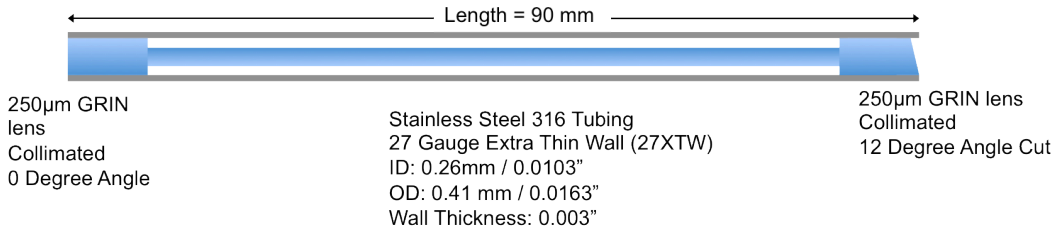

Figure 3.12: Schematics of the inner needle

The inner needle has two parts: a customized fiber/GRIN lens assembly and a stainless tube. The fiber/GRIN lens assembly has two GRIN lenses at the two ends. At the output end, there is a GRIN lens that can collimate the output beam from the delivery fiber and it has a 12 degree angle cut to initiate the deflection. At the input end, there is a second GRIN lens that focuses the collimated light from the rotary jointer into the fiber connecting the two lenses. The entire assembly is encased and glued into a 27 gauge extra thin wall tube. The total length of the fiber/GRIN lens assembly is about 90mm. Since the fabrication of this assembly involving splicing two segments of fiber pieces, the variance of the overall length is larger than a normal fiber assembly. Therefore, we measure their length first and cut each tube accordingly to fit each fiber assembly respectively.

The rotary jointer

The schematics of the rotary jointer is displayed below:

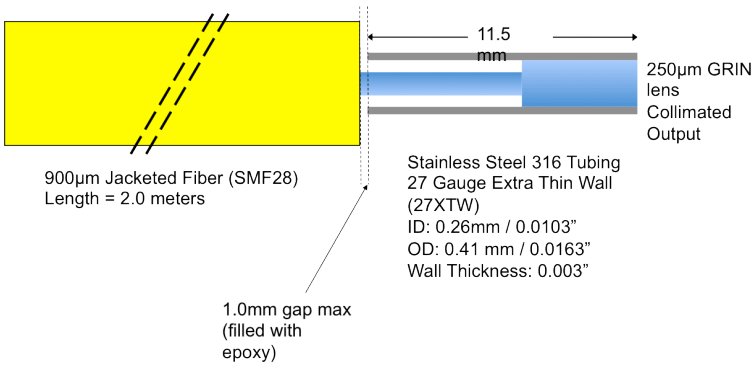

Figure 3.13: Schematics of the rotary jointer

The rotary jointer is responsible for providing a rotary connection between inner needle and the external deliver fiber so that when the needles are rotating the external fiber would get twisted and entangled. To achieve this, as described above, we redesigned the inner needle to make it has two ends. The input end can now take a collimated beam. We added another GRIN lens on the rotary jointer part so that it can collimate the beam from the delivery fiber and send to the inner needle. As shown above, the GRIN lens and part of the fiber pigtail is encased into a 27 gauge extra thin wall tube with a length of 11.5 mm to help protect it.

Here we also show how the electrical and optical parts are interconnected to each other to make the entire system operate.

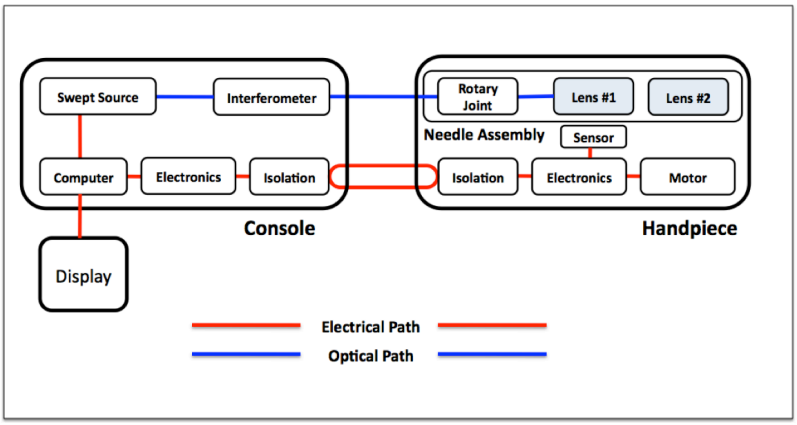

Figure 3.14: System function diagram

Also, we compare the physical specifications of our prototype with commercial available vitrectors to show its compatibility and feasibility in vitrectomy surgeries.

Table 3.1: Form factor comparison

	InnoVit®	UltraVit®	Prototype
Weight	8.5 Grams	9 Grams	14 Grams
Length	~100 mm	~100 mm	104 mm
Max Width	18 mm	18 mm	22 mm
RPM	1200 cuts/ min	5000 cuts/ min	150-500 RPM

Finally, a photo of our prototype is displayed below:

Figure 3.15: Photography of prototype hand-held PARS probe

References

[1] J. Wu, M. Conry, C. Gu, F. Wang, Z. Yaqoob, and C. Yang, "Paired-angle-rotation scanning optical coherence tomography forward-imaging probe," *Optics Letters*, vol. 31, no. 9, p. 1265, May 2006 (cit. on p. 32).

[2] S. Han, M. V. Sarunic, J. Wu, M. Humayun, and C. Yang, "Handheld forward-imaging needle endoscope for ophthalmic optical coherence tomography inspection.," *Journal of biomedical optics*, vol. 13, no. 2, p. 020 505, Jan. 2008 (cit. on p. 32).

[3] J. Ren, H. K. Gille, J. Wu, and C. Yang, "Ex vivo optical coherence tomography imaging of collector channels with a scanning endoscopic probe.," *Investigative ophthalmology & visual science*, vol. 52, no. 7, pp. 3921–5, Jun. 2011 (cit. on p. 32).

[4] S. A. Boppart, B. E. Bouma, C. Pitris, G. J. Tearney, J. G. Fujimoto, and M. E. Brezinski, "Forward-imaging instruments for optical coherence tomography," *Optics Letters*, vol. 22, no. 21, p. 1618, Nov. 1997 (cit. on p. 32).

[5] X. Liu, M. J. Cobb, Y. Chen, M. B. Kimmey, and X. Li, "Rapid-scanning forward-imaging miniature endoscope for real-time optical coherence tomography," *Optics Letters*, vol. 29, no. 15, p. 1763, Aug. 2004 (cit. on p. 32).

[6] T. Xie, H. Xie, G. K. Fedder, and Y. Pan, "Endoscopic Optical Coherence Tomography with a Modified Microelectromechanical Systems Mirror for Detection of Bladder Cancers," *Applied Optics*, vol. 42, no. 31, p. 6422, Nov. 2003 (cit. on p. 32).

[7] C. T. Amirault and C. A. DiMarzio, "Precision pointing using a dual-wedge scanner," *Applied Optics*, vol. 24, no. 9, p. 1302, May 1985 (cit. on p. 34).

Chapter 4

Clinical Applications of PARS Probe

In this chapter, we will present two potential clinical applications of PARS probe: collector channel localization for glaucoma stent implantation and vitreous remnant detection for live animal vitrectomy.

4.1 Collector Channel Imaging for Glaucoma Treatment

The majority of open angle glaucomas result from the retention of aqueous humor. This is mainly caused by abnormalities in the trabecular meshwork (TM) that increase the resistance of aqueous humor outflow into Schlemm's canal (SC), thereby reducing physiological outflow through the collector channels (CCs) and the episcleral veins[1]. Recently stents have been developed to bypass the fluid resisting TM. For example, as shown in Figure 1(a), the Glaukos iStent® is a micro-bypass stent that is surgically implanted into the TM, effectively bypassing the obstructed meshwork, thereby reestablishing physiological outflow of aqueous humor into SC[2, 3].

The implantation process involves introducing the stent into the anterior chamber through a corneal incision. It is advanced across the iris until it can be implanted in the TM. Recent research has shown that SC cross-sectional area is wider in the nasal inferior quadrant of the anterior chamber, suggesting a greater prevalence of CCs draining that segment of SC [4]. It is hypothesized that implanting a stent in closer proximity to these active CCs, may increase fluid outflow. To test this hypothesis, it is first necessary to determine the location of the CCs.

Both high resolution and depth-resolving capability have made Optical Coherence Tomography (OCT) an important ophthalmic diagnostic tool[5, 6]. As scleral tissue and the TM are not transparent to visible light, OCT may be useful to visualize and locate the CCs. Commercial spectral domain (SD) - OCT systems with a light source centered at 870 nm have been used to image through the sclera from the exterior surface of the eye[4]. However, there are two major problems with this

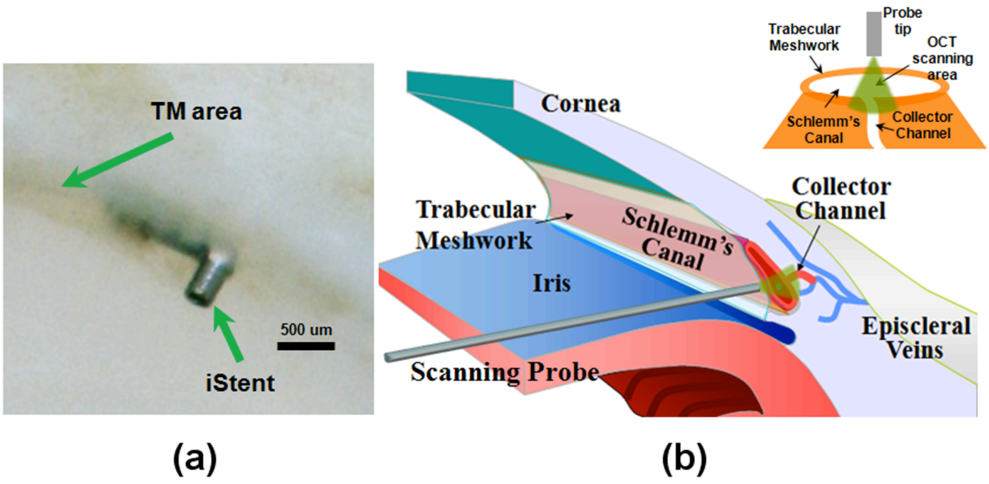

Figure 4.1: Glaucoma bypass stent implantation and its imaging guidance by an endoscopic OCT probe. (a) The Glaukos iStent® bypassing the TM. (b) Surgical configuration of the OCT imaging procedure using an endoscopic probe. The inset illustrates the relative positions of physiological structures and the probe.

method. First, the CCs were not clearly imaged. Both SC and its junctions with CCs (SC/CC) are not easily identified and located from those images. This can be attributed to the fact that the OCT beam coming from outside has been largely scattered by the scleral tissue, especially the blood in superficial vessels, before reaching SC. As a result, the image contrast of the structures inside scleral tissue, such as the SC/CC junctions, has been severely impaired. The shadowing effect by superficial blood vessels obscuring many regions of interest is one example [4]. Images of low contrast preclude the ability of surgeons to select the optimal implantation location of the stents during the operation. Also, a number of axial scans (A scans) were averaged to improve the contrast[4]. This resulted in a scan time of 4.5 seconds, which makes real-time imaging impossible.

Second, for current commercial OCT systems, immobilization of the patient's head is required to provide stable images. For instance, in the previous studies[4], a bite bar was used to reduce eye movement during the 4.5-second scan time and a visual inspection for eye movements between images was performed to subjectively select valid images. This limits the OCT examination to being carried out either before an operation or after. Because of the complex episcleral vein structures in the sclera, it is not easy to trace them back to SC during an operation even if they could have been located in a pre-acquired OCT image slice. Therefore, it would be much more desirable to have a real-time imaging method that can view the surgical field from the inside of the anterior chamber during these surgeries.

OCT endoscopes offer a potential solution to the above problems. They can be placed deep into tissues and collect reflected optical signals from the desired depth, providing images of much higher quality by overcoming signal attenuation from intervening tissue such as the sclera or TM.

Furthermore, due to their small size, hand-held endoscopic probes can be used intra-operatively and are capable of providing real-time visualization and guidance for the specific structures of interest[7]. Therefore, we propose an OCT endoscopic probe to determine the locations of CCs for the bypass stent implantation, as illustrated in Figure 1(b). The proposed probe passes through the corneal incision for implantation and is advanced across the iris until it is in apposition to the TM, approximately 0.5 to 1 mm away. Then the probe starts scanning the forward cone in front of its tip in a fan shape fashion. The OCT beam penetrates TM, imaging the cross-section of the SC and disclosing the structures inside, such as CCs. The relative geometry between tissue structures and this probe is shown in the inset. The goal of this research is to develop such an endoscopic OCT probe and determine if it is capable of locating the CCs exiting from SC and its suitability for intra-operative ophthalmic applications.

4.1.1 Methods

The Scanning Endoscopic Probe

The prototype endoscopic probe developed in this study is based on a similar design as described in our previous publications[8, 9]. It contains two stainless steel needles, the inner needle and the outer needle. Each of them houses one segment of GRIN lens. The OCT laser beam is guided through a single mode fiber into the inner needle. A glass ferrule is used to fix and center the fiber end inside the inner needle and it is followed by the first GRIN lens. Both the front surface of the glass ferrule and the back surface of the lens have been angle-cut to 80 to reduce reflection. The lens is 2.5 mm long and collimates the incoming laser beam from the delivery fiber end. Its front end has been polished at a 22.50 angle to initiate the first beam deflection.

The second GRIN lens mounted in the outer needle has a length of 5.6 mm. It further deflects the beam and focuses it to a working distance ahead of the probe tip. The back end was also polished at a 22.50 angle and the front end was a blunt end and was sealed with epoxy to avoid fluid leakage.

The outer diameter of both lenses and the ferrule is 1.0 mm. The inner/outer diameter (ID/OD) of the inner needle is 1.0/1.2 mm, while that of the outer needle is 1.3/1.6 mm. There was a metal sleeve used to adapt the second lens into the outer needle, which has an ID/OD of 1.0/1.3 mm. The overall length of the probe is 63.5 mm. Optical grade epoxy was used to glue and fit the optical components inside the needles. The lenses were fabricated by GRINTECH GmbH [Jena, Germany] and the needle tubes were machined by Trinity Biomedical Inc [Wisconsin, US]. The schematic of the probe is illustrated in Figure 2.

By rotating the inner and outer needles (thus the lenses) at the same angular speed but in opposite directions, the probe can steer the laser beam in a fan shape pattern. Combined with the OCT axial scan, the probe can provide two dimensional images representing physiological structures in the

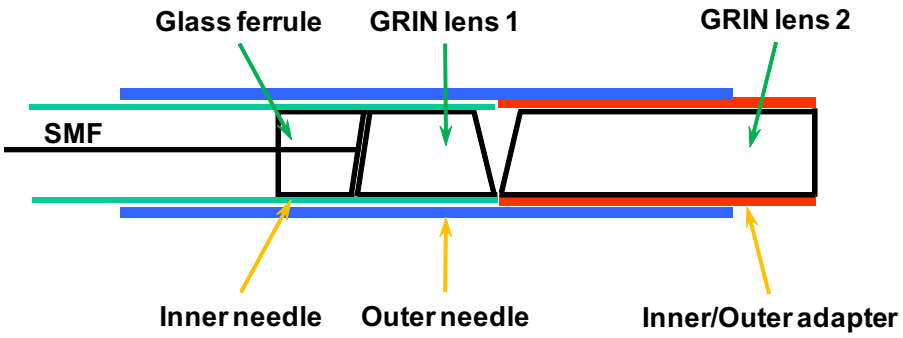

Figure 4.2: Schematic of the prototype endoscopic probe. SMF, single-mode fiber.

forward cone of the probe tip. An actuation system was built to drive the needles, as partly pictured in Figure 3. The system utilizes a single motor and a set of bevel gears to mechanically ensure the rotation synchronization of the lenses. A feed-back electronic system was also implemented to maintain a constant rotation speed. The speed deviation was kept within 2.5% of the desired value. In the following imaging experiments, the system was configured to operate at 0.5 scans per second.

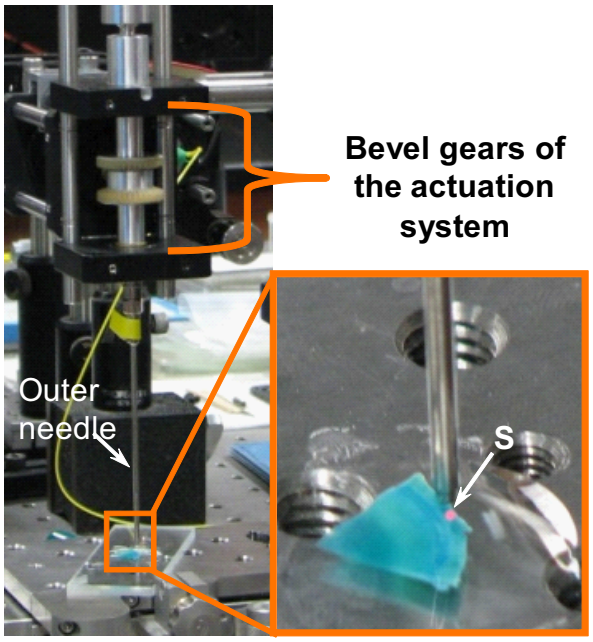

Figure 4.3: A side view of the endoscopic OCT probe and actuation system used in the CC imaging experiments. A close view of the probe tip and the human cadaver eye tissue underneath is enclosed. The sample has been dyed with methylene blue. The bevel gears of the actuation systems synchronize the lens rotation mechanically. The outer needle is 63.5mm long. S, the red aiming beam spot onto the sample.

The Swept Source OCT System

As shown in Figure 4, we built an OCT system based on a swept source laser (Micron Optics S3, Atlanta, Georgia) for this study. The laser is centered at 1310 nm with a wavelength tuning range of about 100 nm. Two optical circulators were used to assemble the interferometer for the OCT setup. The output power of the laser is 9.8 mW and the power delivered onto the sample is below 1 mW due to the passive losses in the system. A 660 nm laser aiming beam with an average power about 10 uW or less was combined with the OCT beam by a WDM (Wavelength-division multiplexing) coupler. It provides a visible indication of the scanning beam's position on the tissue. The A scan rate was configured at 333 Hz.

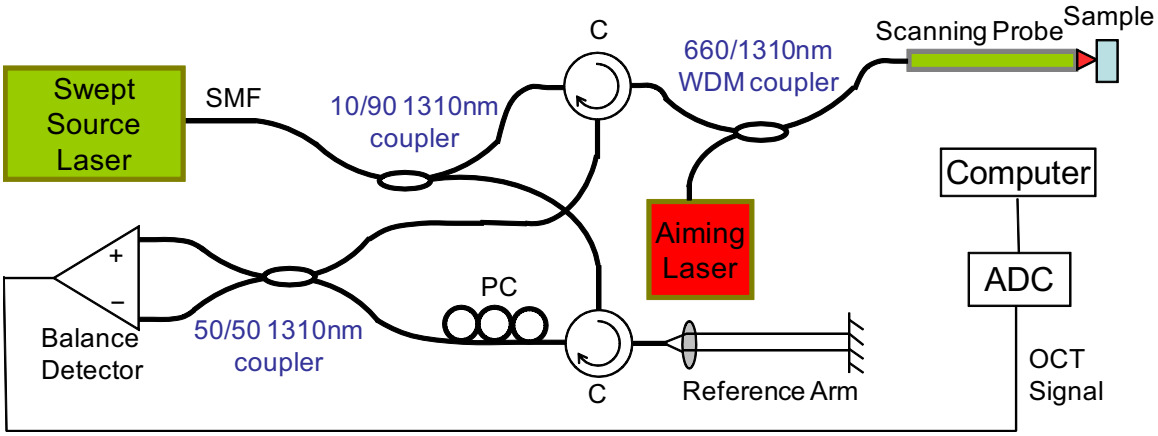

Figure 4.4: The swept source OCT setup. SMF, single-mode fiber; PC, polarization controller; ADC, analog-to-digital converter; C, optical circulator.

Imaging the Collector Channel

Human cadaver eye tissue was prepared for OCT imaging. The cornea and surrounding tissue were dissected from a whole globe, removing the iris, lens and supporting tissue. The resulting shell was quartered and the segments were dyed with methylene blue for a better visual contrast between the SC and the sclera. We removed TM from some tissue segments while maintaining TM for other segments. This formed two groups of samples. Each segment under test was placed in a microscope slide well with a few drops of basic saline solution to prevent desiccation. The microscope slide was secured on a mechanical stage. The OCT probe was positioned over the tissue and adjusted to have a distance of about 1.5 mm from the tip to the sample, as shown in Figure 3. The stage could be translated to move the sample across the surface perpendicular to the probe's axis. OCT images were displayed on the system monitor.

First, we examined the tissue penetration of the 1310 nm OCT light on the samples with TM intact. To test the penetration over the entire sample, instead of rotating the two needles to gen-

erate a fan shape scan, the stage was linearly translated so that the probe was traveling relatively perpendicular to SC by a longer range to cover the tissue sample while the laser beam was kept undeflected. Thus the resulting OCT images in this step have a regular rectangular shape.

Upon the verification of the tissue penetration of 1310 nm light, we next proceeded to search and image CCs using the probe, where the needles were actuated to rotate. The stage was translated so that the probe was moving relatively along the SC to search CCs, while the beam was scanning the cross section of the SC in a fan shape pattern, as shown in Figure 1(b). To provide corroboration of any CCs found by the probe, the experiments in this step were conducted on tissues with their TM removed so that image confirmation by scanning electron microscopy (SEM) could be performed later. If the TM were not removed, it would be very difficult to accurately map out the CCs found underneath over the entire sample and image the appropriate parts of it by SEM. This would have resulted in a remote chance of correct correlation between OCT and SEM images. Also, during SEM sample preparation, desiccation of the samples would have caused the TM tissue to obscure the openings of any CCs found during OCT examination.

Once we located the CCs from the OCT images, we recorded their location and mapped them across the sample using the scanning visualization provided by the aiming beam. We then sent the sample for study by using SEM to image those spots where CC openings were located.

4.1.2 Results

A typical OCT image acquired by translating the stage in the penetration verification experiments is shown in Figure 5(a). It clearly depicts the shape of the cross section of the SC. The tissues under TM and on the other side of SC wall have almost as good clarity as TM itself. There is no observable shadow effect from TM. These images verify that the probe operating at 1310 nm can indeed clearly visualize tissues behind the TM for a considerable distance. Some of these images even reveal structures that could be CCs branching far away from their openings inside SC.

A typical OCT image acquired by rotating the needles of the endoscopic probe in the experiments searching CCs is shown in Figure 5(b). From the OCT image, one can clearly see not only the CC's opening exiting for the SC wall but also the shape of the channel winding into the sclera. Based on these images, we were able to quantitatively measure the dimensions of these physiological structures. The SEM image of the CC is shown in Figure 5(c) for comparison. The two methods agree with each other indicating the CC's opening was approximately 120 μm wide.

The probe focuses the probing beam to a working distance of about 1.4 mm (in air) ahead of the tip. The focal spot was measured to range from 12 to 14 microns in diameter. Both the working distance and the spot size have a weak dependence on the deflection angle. The maximum variation of the spot size was 16% and the variation in the working distance was 13%.

A maximum scan range of about 40 degrees (20 degrees for half angle) was achieved. The axial

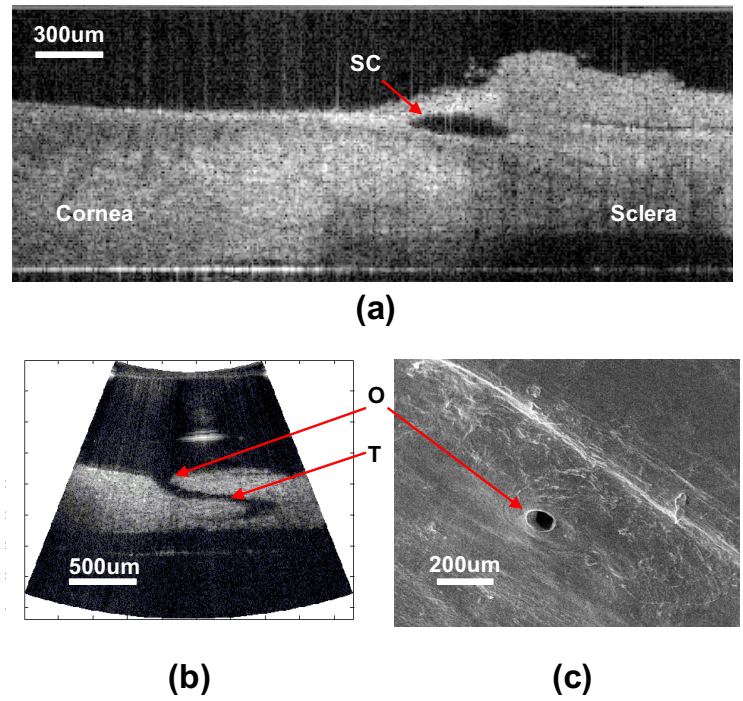

Figure 4.5: OCT and SEM images of human cadaver eye tissue segments. (a) OCT image of a tissue segment with TM intact, acquired by translating the stage. (b) OCT image of a tissue with TM removed, acquired by rotating the needles of the endoscopic probe. (c) SEM image of the same CC in (b). O, CC's opening; T, CC's path through sclera.

scan range was 3 mm, which was determined by the sampling period in the wavenumber space. The signal-to-noise ratio of the entire system was measured to be over 95dB.

4.1.3 Discussion

As opposed to 800 nm, the typical wavelength range for ophthalmic OCT imaging used by previous studies4, 7, a central wavelength of 1310 nm was selected for this study. Indeed, axial resolution is lower for longer central wavelength assuming the same wavelength scan range. The theoretical axial resolution of our system is 7.5 microns while that of the previous studies[4] was 1.3 microns. However, as shown in Figure 5, one can easily identify and locate CCs from the images acquired by the probe. It indicates that the 7.5-microns axial resolution is sufficient as the dimensions of the structures are usually on the order of several 10s microns. The fact that the previous systems [4] with higher axial resolution could not provide images of the same quality could be mainly due to light scattering and absorption by intervening tissues. Although there was no blood involved in this ex vivo study, one can expect an improved performance over shorter wavelengths for in vivo studies since shorter wavelengths suffer more from optical scattering6. Higher water absorption at 1310 nm should not impair the image contrast as much as expected in external OCT systems. It is because that the distance from the probe tip to the tissue of interest is usually kept from 0.5 to 1 mm during

the intended endoscopic imaging procedures.

This wavelength selection of 1310 nm has been verified in the initial penetration verification experiments. Although we did not happen to catch a CC during those experiments, (which were not designed to search CCs after all), based on the images we obtained with TM intact, if a CC had been captured in those experiments, the clarity should be comparable. Besides the advantages of 1310 nm light, this is mainly because that the beam has bypassed the majority of intervening tissues and the only tissue left is a thin and flimsy layer of TM with its thickness usually around several 10s microns, which can be easily penetrated as shown in Figure 5(a).

Although the rotation speed of the motor was well maintained as constant, the angular speed of the deflection was not constant. This is because the deflection angle is not linearly related to the rotation angle9. An accurate relationship of the two angles is critical for accurate image reconstruction. In this study, based on a simplified model9, we further developed a more accurate theoretical model to estimate the deflection angle. A ZEMAX [ZEMAX Development Corporation, Washington, USA] numerical simulation was also used to verify this calculation. Finally, we experimentally measured the relationship. These results are shown in Figure 6. We applied this result to the final image reconstruction to obtain the correct geometry of the structures.

In this endoscopic probe design, the actuation system is located far away from the probe tip, which enables easy miniaturization. The diameter of the probe is mainly limited by that of the GRIN lenses. Previously we have already achieved a narrower probe10, which was encased in two needles of 23/21 gauge for the inner/outer needles. Nowadays GRIN lenses with diameter less than 400 microns are commercially available. This can further reduce the probe size and make it small enough to be introduced through a clear corneal incision for OCT visualization of CC location prior to or while implanting a bypass shunt.

As mentioned in our previous publication[8], inherent in this technology is the capability to do volumetric scanning by employing different rotating modes. By driving the lenses at different angular speeds and switching their rotation direction, we can engineer many volumetric scanning patterns besides the current planar fan shape scan pattern. Those patterns might permit visualization of larger areas leading to more rapid identification of tissue structures.

It is worth mentioning that the frame rate of the OCT system (0.5 fps) was limited by the scan rate of the swept laser. To accumulate enough A scans (666 depth scans in our case) for each OCT image frame, the rotation speed of our probe had to be kept at a constant value of 15 rpm, which is much lower than what it can support. OCT engines with A scan rate over 100 kHz have been demonstrated[10] and OCT systems over 20 kHz are now commercially available as well. These could significantly increase the frame rate of our endoscopic system.

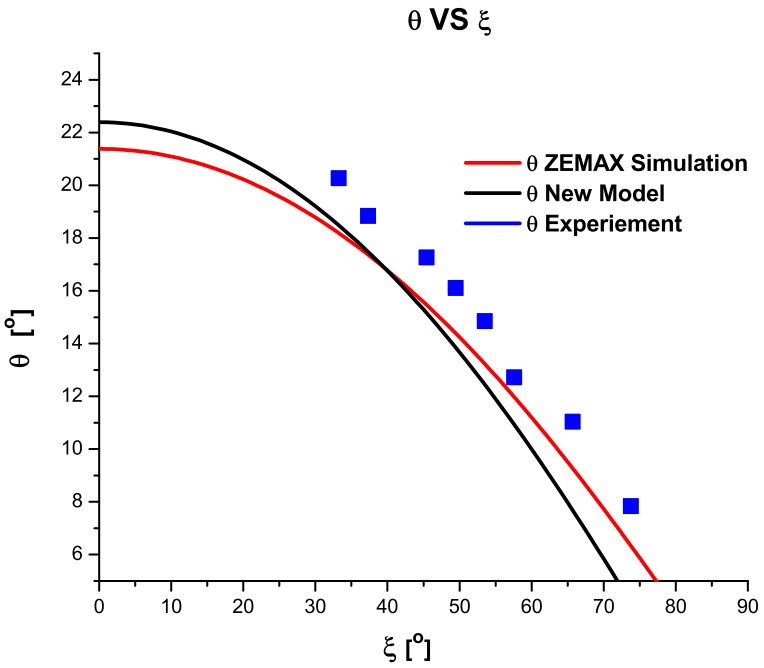

Figure 4.6: The relationship between deflection angle θ and rotation angle ξ. Black line shows the result of the new theoretical model; red line shows the result of the ZEMAX simulation; blue line shows the result of the experimental measurement.

4.1.4 Conclusion and Future Works

This study demonstrates that our endoscopic probe has sufficient resolution to locate and image CCs exiting SC in ex vivo human cadaver eyes. It may potentially be adapted to visualize the anterior chamber intra-operatively to provide guidance for surgeries such as bypass stent implantation.

Motion artifact, a common problem existing in OCT images, results from the relative movement between tissue target and OCT instrument. During stent implantation, eyelids are usually immobilized by clamps. Since the probe is inserted via a corneal incision, the probe's position relative to TM and SC are relatively constant. To further decrease this artifact, higher frame rates (>24 frames/s) need to be achieved for real-time video operation by utilizing OCT systems with faster A scan rates. This upgrade combined with improved eye immobilization procedures during surgeries will minimize the motion artifacts.

As mentioned above, volumetric scan patterns can be designed to enable three-dimensional OCT imaging. Integration of this imaging device with other surgical tools may ultimately provide intra-operative assistance to surgical procedures that could benefit from real-time imaging guidance.

4.2 Live animal vitrectomy

Vitrectomy is an ophthalmic procedure, where some or all of the vitreous humor are removed from the eye. Often times it is one important precursor within a more complicated eye surgery. Successful vitrectomy benefits many retinal surgeries, such as vitreous floaters, retinal detachment, macular pucker, diabetic retinopathy.

During this procedure, the complete removal of the vitreous humor is extremely crucial as the long-term prognosis for patients highly depend on the complete removal of vitreous humor around retinal tears and holes. However, the direct visual inspection is difficult in this situation. As shown in Figure 7, currently surgeons will typically illuminate the posterior chamber with a light pipe, while use a vitrector to dissect the vitreous substances and another pipe to suck the vitreous humor out. Because the vitreous is transparent, it is hard to distinguish its remnant on retina from other part of the tissue. Therefore, an intraoperative tool that can help examine the remnant on top of retina will be very beneficial to the success of the entire surgery.

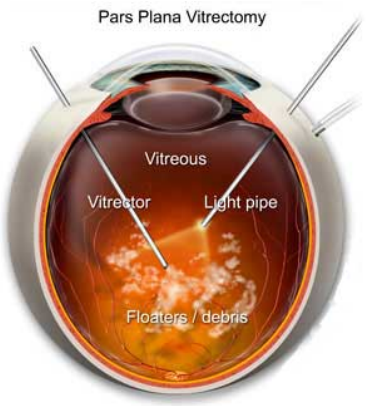

Figure 4.7: Illustration of the vitrectomy procedure

Due to its tomographic feature, OCT can assist in this examination in that it can generate depth-resolved images to show the layer structures of retina and beyond. In this capacity, compared to commercial external OCT systems, a forward-imaging OCT endoscopic probe can be placed in close proximity to the retinal surface, avoiding the intervening through the cornea, anterior chamber and crystalline lens. More importantly, the endoscopic probe can be used during the surgery to provide physicians a real-time feed-back, informing of the location and size of the remnant vitreous humor. While on the other hand, without this type of visual guidance, during the operation, surgeons have to remove the vitreous humor based on their practice experience and the chance of complete removal of vitreous humor is not guaranteed.

PARS probe, designed as an endoscopic probe, is well suited for this purpose, as it has the same form factor as the light pipe currently used in vitrectomy. Surgeons can potentially reuse the same

cannula for the light pipe and insert PARS probe to visualize the retinal surface and locate any residual vitreous humor. This process is depicted in the following figure.

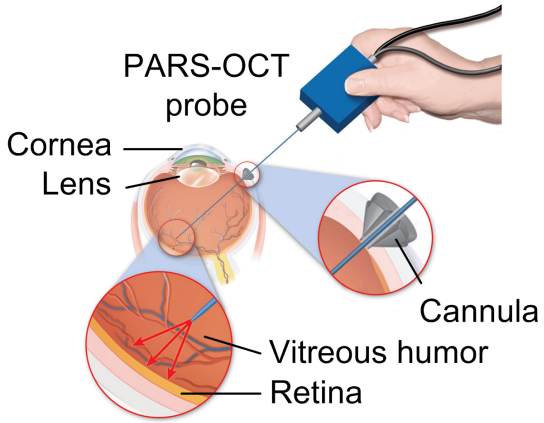

Figure 4.8: Illustration of PARS aiding vitrectomy

With this goal in mind, as detailed in last chapter, we designed and fabricated a prototype hand-held PARS with an overall diameter of 1.6 mm and 500 micron GRIN lens. To demonstrate its feasibility of aiding vitrectomy, we carried two sets of imaging experiments: ex-vivo porcine eye retina imaging and vitrectomy on live rabbit.

4.2.1 *ex vivo* porcine eye retina imaging

The sample imaged was enucleated porcine eyes. The eyes were harvested and saved appropriately before the experiment to ensure the integrity of the tissue. As shown in the following figure, during the experiment, the cornea, the lens, the anterior chamber, and their surrounding tissue were dissected off from the whole globe. After the posterior chamber is exposed, vitreous humor was removed, leaving the retinal inside the globe shell.

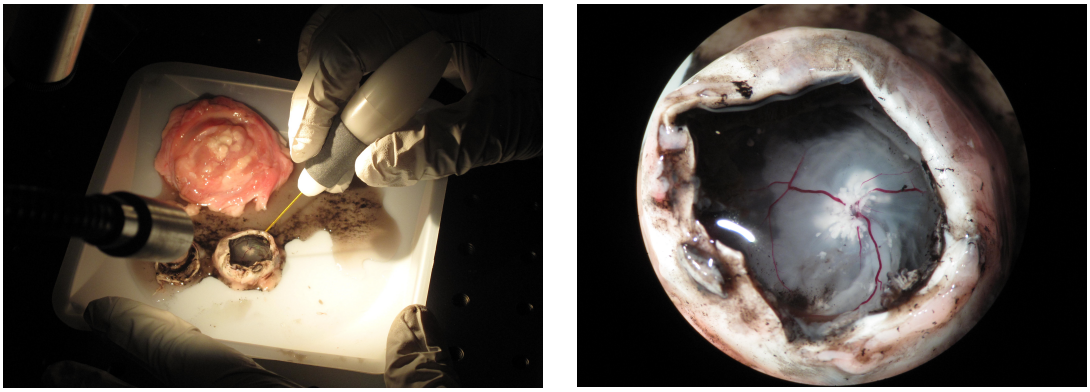

a **b**

Figure 4.9: PARS probe imaging an enucleated porcine eye

We imaged different parts inside the globe shell, including: retinal layers, optic nerve, blood vessels, vitreous, RPE, and some sub-retinal features.

First, we imaged the optic nerve and vessels using the probe. As shown in the following two images, the optic nerve area appear as a vertical well showing the structure near the nerve head. The holes under the retinal layer represent some prominent blood vessels.

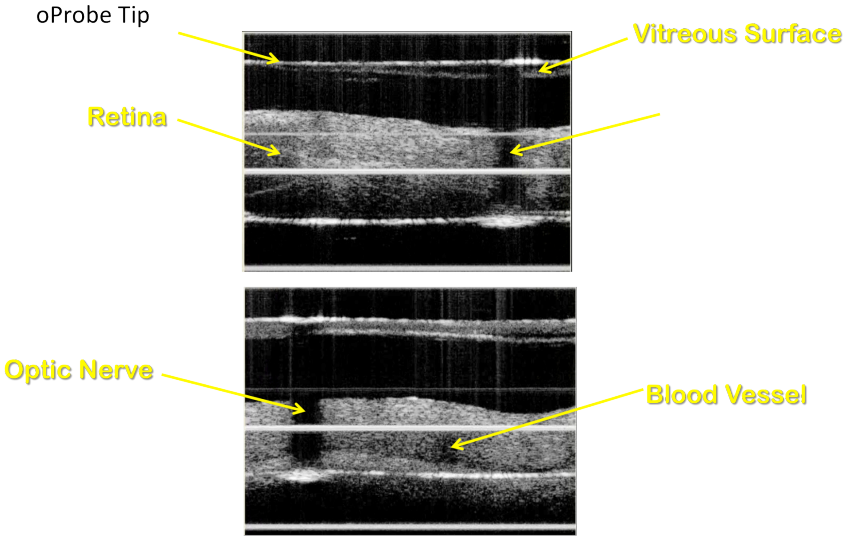

Figure 4.10: OCT image of optical nerve and blood vessel

Next, we compared the cases with vitreous remnant and saline injection. The purpose of this experiment is to test whether one can distinguish vitreous and saline as while vitreous is sucking off the globe and saline is injecting into the globe to hold its shape. As shown in the following figure, we did succeed in differentiating them. But it was because the floating pigment in the saline functioned as scatters. A more reliable way is still needed.

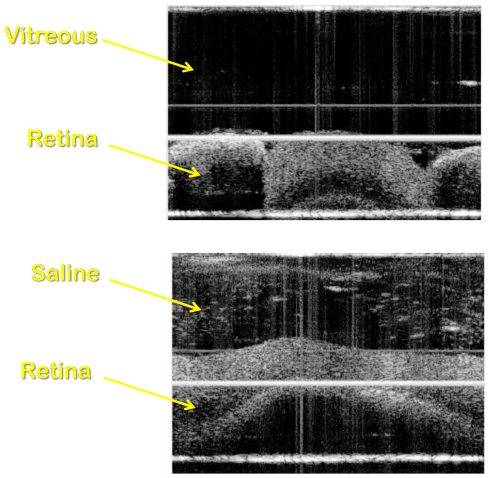

Figure 4.11: Comparison of vitreous and saline. The floaters in the saline were pigment

We also investigated a surgical situation that might occur during vitrectomy. Sometimes, sub-retinal bubbles will be introduced within the operation. We wanted to test whether the imaging probe can detect this type of abnormality. Therefore, we intentionally introduced a air bubble under the retina and imaged the areas in and out of the bubble. The results are compared below:

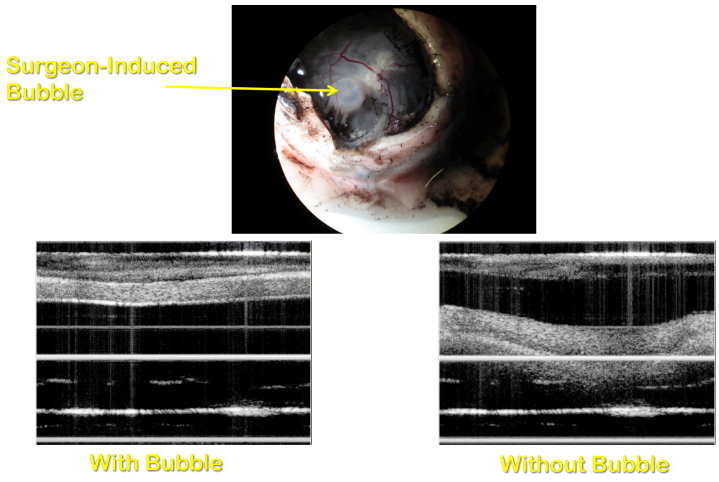

Figure 4.12: Sub-retinal bubble

The image around the bubble area is showing the retina layer is lifted up and stretched due to the internal air pressure, while the image out of the bubble area shows the retina in a natural status without tension and lifting.

4.2.2 OCT imaging on vitrectomized rabbit

After confirming the retinal imaging capability of the endoscopic probe, we continued experimental verification on an animal model. We chose rabbit as the model and carried a vitrectomy on a euthanized rabbit. The clinical surgery was performed first. The following figure shows the actual clinical of setting of the rabbit vitrectomy surgery.

After the majority of the vitreous humor was removed from the rabbit's eye, we inserted our probe into the globe to locate any vitreous remnant. The imaging results are shown below:

From the above figure, we can clearly see the retinal layers and some remnant vitreous. It mainly includes three different cases: continuous vitreous, where there are vitreous remnant covering the entire field of view; scattered vitreous, where there are some vitreous left on top of the retinal; no vitreous, where there is no vitreous remnant. These results once again verified the effectiveness of this probe in assisting vitrectomy.

a **b**

Figure 4.13: Vitrectomy on live rabbit

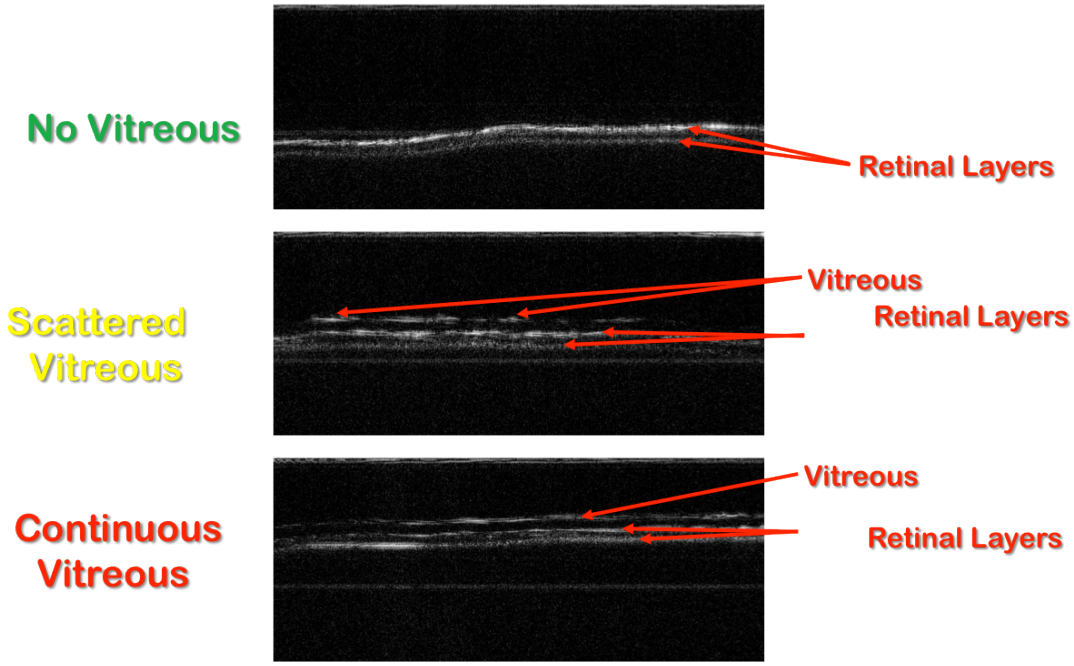

Figure 4.14: OCT images of vitrectomized rabbit

References

[1] R. Rosenquist, D. Epstein, S. Melamed, M. Johnson, and W. M. Grant, "Outflow resistance of enucleated human eyes at two different perfusion pressures and different extents of trabeculotomy.," *Current eye research*, vol. 8, no. 12, pp. 1233–40, Dec. 1989 (cit. on p. 45).

[2] G. Dvorak-Theobald, "Schlemm's Canal: Its Anastomoses and Anatomic Relations.," *Transactions of the American Ophthalmological Society*, vol. 32, pp. 574–95, Jan. 1934 (cit. on p. 45).

[3] C. K. Bahler, G. T. Smedley, J. Zhou, and D. H. Johnson, "Trabecular bypass stents decrease intraocular pressure in cultured human anterior segments.," *American journal of ophthalmology*, vol. 138, no. 6, pp. 988–94, Dec. 2004 (cit. on p. 45).

[4] L. Kagemann, G. Wollstein, H. Ishikawa, R. A. Bilonick, P. M. Brennen, L. S. Folio, M. L. Gabriele, and J. S. Schuman, "Identification and assessment of Schlemm's canal by spectral-domain optical coherence tomography.," *Investigative ophthalmology & visual science*, vol. 51, no. 8, pp. 4054–9, Aug. 2010 (cit. on pp. 45, 46, 51).

[5] D. Huang, E. Swanson, C. Lin, J. Schuman, W. Stinson, W. Chang, M. Hee, T. Flotte, K. Gregory, C. Puliafito, and A. Et, "Optical coherence tomography," *Science*, vol. 254, no. 5035, pp. 1178–1181, Nov. 1991 (cit. on p. 45).

[6] B. Povazay, K. Bizheva, B. Hermann, A. Unterhuber, H. Sattmann, A. Fercher, W. Drexler, C. Schubert, P. Ahnelt, M. Mei, R. Holzwarth, W. Wadsworth, J. Knight, and P. S. J. Russell, "Enhanced visualization of choroidal vessels using ultrahigh resolution ophthalmic OCT at 1050 nm," EN, *Optics Express*, vol. 11, no. 17, p. 1980, Aug. 2003 (cit. on p. 45).

[7] J. Ren, J. Wu, E. J. McDowell, and C. Yang, "Manual-scanning optical coherence tomography probe based on position tracking," *Optics Letters*, vol. 34, no. 21, pp. 3400–3402, 2009 (cit. on p. 47).

[8] J. Wu, M. Conry, C. Gu, F. Wang, Z. Yaqoob, and C. Yang, "Paired-angle-rotation scanning optical coherence tomography forward-imaging probe," *Optics Letters*, vol. 31, no. 9, p. 1265, May 2006 (cit. on pp. 47, 52).

[9] S. Han, M. V. Sarunic, J. Wu, M. Humayun, and C. Yang, "Handheld forward-imaging needle endoscope for ophthalmic optical coherence tomography inspection.," *Journal of biomedical optics*, vol. 13, no. 2, p. 020 505, Jan. 2008 (cit. on p. 47).

[10] R. Huber, D. C. Adler, V. J. Srinivasan, and J. G. Fujimoto, "Fourier domain mode locking at 1050 nm for ultra-high-speed optical coherence tomography of the human retina at 236,000 axial scans per second," EN, *Optics Letters*, vol. 32, no. 14, p. 2049, Jul. 2007 (cit. on p. 52).

Chapter 5

Optical Coherence Tomography Probe III – Electrical Scanning

This chapter is to present an investigation on a electrical scanning mechanism for OCT systems. The core of OCT B scan is beam steering. While both manual scanning and mechanical scanning involve some movement to physically move the beam, an apparatus utilizing a special EO effect can be a potential method for endoscopic OCT, which involves no moving parts and are intrinsically high speed and has random access capability.

5.1 KTN Crystal and Its Electro-Optic Effects

The electro-optic (EO) effect in crystals is a phenomenon where the refractive index is modulated by an externally applied electric field. Depending on the symmetry of a crystal, two major EO effects exist: the Pockels effect and the Kerr effect. The Pockels effect is a first-order effect and the change in the refractive index is linearly proportional to the applied electric field. The Pockels effect occurs only in noncentrosymmetric materials, such as lithium niobate. On the other hand, the Kerr effect is a second-order effect, where the change in the refractive index is proportional to the square of the applied electric field. Although the Kerr effect can effect in any material, only a few materials can exhibit a useful amount of index change, which include barium titanate, strontium titanate, strontium barium niobate, and potassium tantalate niobate. The refractive index change for the two effect are expressed as following:

$$\Delta n^{Pockels} = -\frac{1}{2} n^3 r_{ij} E(x) \tag{5.1}$$

$$\Delta n^{Kerr} = -\frac{1}{2} n^3 s_{ij} E(x)^2 \tag{5.2}$$

where the first equation describes the Pockels effect and the second accounts for the Kerr effect,

n is the refractive index, rij is the Pockels constant, and sij is the Kerr constant.

One important application of the EO effects is the optical beam deflection. Comparing with other technologies such as galvanic mirrors, polygon mirrors, microelectromechanical system (MEMS) mirrors, and acousto-optic deflectors, EO deflector can have a fast response and random access capability. By introducing linear phase retardation across the beam, they refract light beams. The deflection angle is controlled by the amount of EO-induced phase delay. A linear phase delay can be generated by a few different methods, which include forming an EO crystal [1], an electrode [2], or a ferroelectric domain into a prism shape [3]. The linearly graded refractive index can also be introduced by the linear distribution of the modulation index with properly designed electrodes [4].

KTN, a mixture or solid solution of potassium tantalate [KTaO3 (KT)] and potassium niobate [KNbO3 (KN)], exhibits a very large EO effect and has been attracting researchers' interest [5–7]. The crystal phases of KTN reply on both composition ratio (KT and KN) and the temperature. The phase change is as shown in the following plot. At cubic phase KTN has inversion symmetry and its dielectric property is paraelectric and the lowest order effect is the Kerr effect, while for the other phases it is ferroelectric and the Pockels effect occurs.

While in its cubic phase, KTN crystals are generally deemed to be an insulator since they do not have free electrons. But electrical conduction might be possible by electric field drift/diffusion [8], if there is an Ohmic electrical contact with the crystal so that electrons can be injected into the conduction band of the KTN crystal []. As true charges inside the crystal, the injected electrons terminate the electric field originating from the anode, and the electric field becomes nonuniform between the electrodes.

Here the electric field E(x) and the injected electron density Ni(x) are related by Gauss's law:

$$\frac{\varepsilon}{e}\frac{\mathrm{d}E(x)}{\mathrm{d}x} = N_i(x) \tag{5.3}$$

where x is the distance from the cathode, ε is the dielectric constant, and e is the unit charge of an electron. Using the current continuity law, we know the injected electrons drift to the anode and the current density J is connected to Ni(x) and E(x) as following:

$$J = eN_i(x)\mu E(x) \tag{5.4}$$

where μ is the electron mobility in the crystal. Combining the above two equations, we have a differential equation as follows:

$$E(x)\frac{\mathrm{d}E(x)}{\mathrm{d}x} = \frac{J}{\varepsilon\mu} \tag{5.5}$$

Solving this equation, we get a few very indicative results:

1. The $E(x)$

$$E(x) = \frac{3}{2} E_0 \sqrt{\frac{x}{d}} \tag{5.6}$$

where $E_0 = \frac{V}{d}$. This suggests that the electrical field distribution across the electrodes follows a square root law.

2. The refractive index change

Since the Kerr effects obeys the square law, as following:

$$\Delta n(x) = -\frac{1}{2} n^3 s_{ij} E(x)^2 \tag{5.7}$$

Substituting the $E(x)$ formula we got above into it, we have:

$$\Delta n(x) = -\frac{9}{8} n^3 s_{ij} \left(\frac{x}{d}\right) E_0^2 \tag{5.8}$$

This indicates that there has been built a linear the refractive index change profile across the electrodes. And if a beam passes it, it will be deflected and the deflection angle can be calculated from above equation as:

$$\theta \cong L \frac{\mathrm{d}}{\mathrm{d}x} \Delta n(x) = -\frac{9}{8} n^3 s_{ij} \frac{L}{d} E_0^2 \tag{5.9}$$

This phenomenon with the electrical field and refractive index change is illustrated as below:

Since the optical deflection in this mode involves the injection of electron, this effect has been termed as space-charge-controlled electro-optic effect.

In practice, the KTN deflector demonstrated a wide deflection angle of $\pm 125\, mrad$ ($\pm 7.16^o$ with a low electric field of $\pm 500\, V/mm$ and a short interaction length of $5\, mm$ [9, 10]. This is enabled by the successful growth of KTN crystals of optical quality with volumes of over $30\, cm^3$ (e.g., $40 \times 40 \times 20\, cm^3$ by the top seeded solution growth method [11].

In summary, we draw the following diagram to show the intrinsic logic behind this effect.

5.2 OCT Imaging Based on Beam Deflection in KTN Crystal

The essence of optical endoscopes lies in the method how the probing beam is scanned. We realized that a perfect beam deflection is introduced by linear optical phase retardation, and the slope of the optical phase profile determines the deflection angle. Therefore, to have a scanning beam, one needs to generate a time-varying optical phase retardation or profile. The OCT endoscopes, both

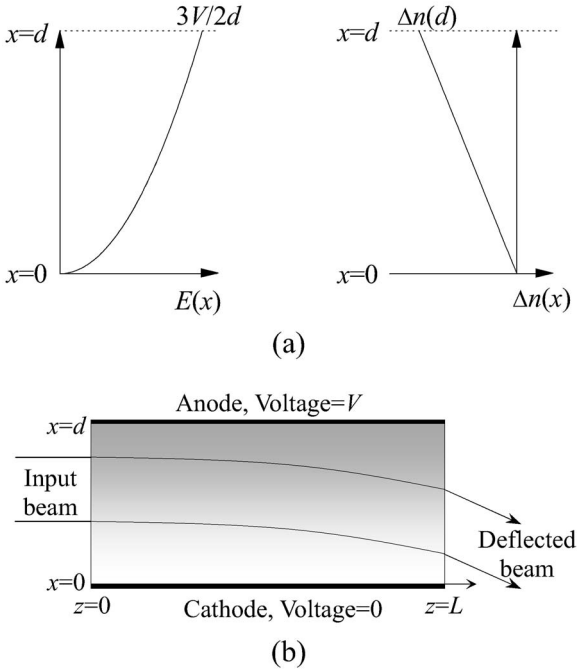

Figure 5.1: KTN Principle(a) Electric field and refractive index distributions. (b) Beam deflection by linearly graded refractive index. The gray scale schematically shows the linearly graded refractive index induced by the Kerr effect and the space- charge effect.

manual and mechanical scanning, we investigated previously achieved this by physically actuating certain optical elements, thus moving the entire atoms lattice of the material. Here, we can't help raise a question: "Can we achieve that by only moving some smaller particles, such as electrons?" And the answer is Yes.

Indeed the EO effect of KTN crystal is very inspiring when redesigning a novel OCT endoscope. First, by moving a smaller particle – electron, the KTN crystal can generate the linear phase profile very fast. The achieved the scanning speed has gone beyond several hundred KHz. Second, the elimination of complex mechanical parts make a smaller and lighter endoscope possible. Third, since there are no moving parts involved within this type of scanning, the probe based on it should be much safer for many delicate surgical applications. Fourth, as we described in last section, the KTN deflectors do not have to follow a predefined the scanning orbit, like most of mechanical probes do, the endoscope based on it can have random access capability, meaning the beam can virtually switch from one direction to another at user's discretion. One can also program the scanning pattern easily by designing appropriate scanning voltage. And this feature is particularly desirable for certain diagnosis and treatment combined situation.

Although KTN based OCT endoscopes have many desirable features that have not been carried by mechanical methods, there are several technical hurdles that needs to be overcome before they can

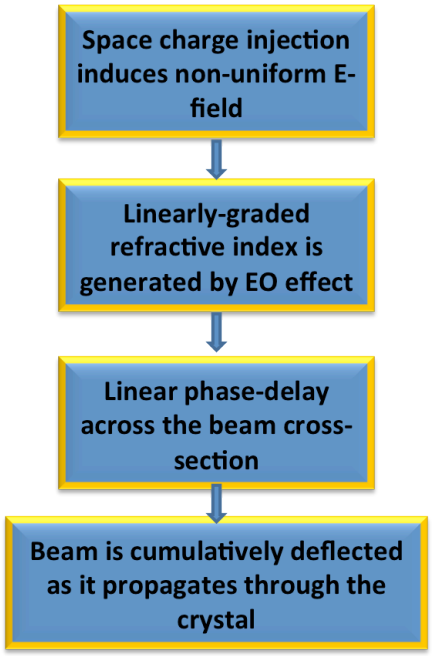

Figure 5.2: Space-charge-controlled EO effect principle diagram

actually work as a potential candidate for clinical applications. Among them, chromatic dispersion is the most important one.

KTN crystal is a dispersive medium. Most of OCT setup described previously are fiber-based and centered at 1310nm. As the single mode glass fibers, like SMF-28 corning, have their zero dispersion wavelength at 1310nm, the dispersion compensation of those setup are usually unnecessary unless the optical path length is extremely long. However, after introducing the KTN crystal into the system, it results in a significant dispersion in the wavelength band we used. Therefore, an appropriate dispersion estimation and compensation is a must for the system to operate well. This part of investigation will be discussed in the next chapter.

5.3 Design and Implementation of a Bench-top KTN OCT System

Based on the above idea, we designed a bench-top KTN OCT system to verify the feasibility of KTN scanning for OCT. We utilized a two dimension/axis KTN deflector from NTT-AT to build the setup. The following figure shows the schematic of the deflector.

The crystal inside has a length of 4mm along the optical axis but an effective optical path length of 12mm due to a triple pass configuration. The half wave plate is used to rotate the polarization of the beam to align with the crystal main axis. The first collimation lens is to couple light from

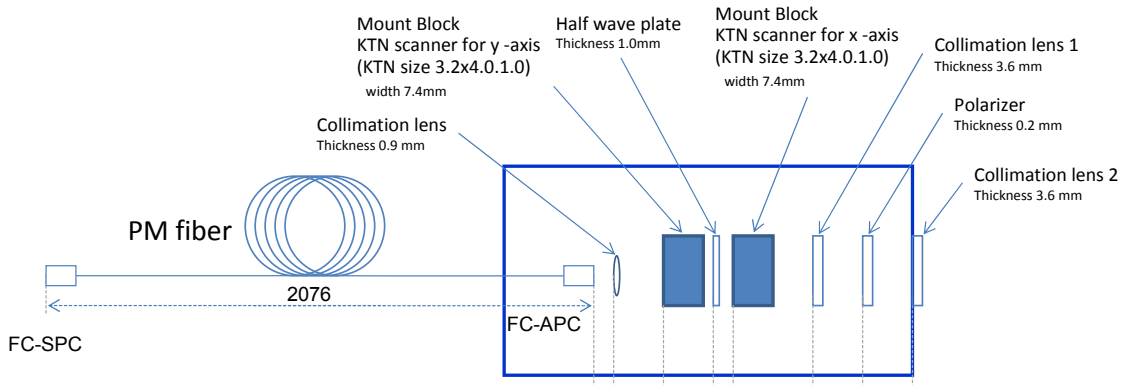

Figure 5.3: Structure of the KTN deflector

the delivery fiber to the crystal. The second and the third cylindrical lens are to compensate the lensing effect of the crystal.

The following schematic shows the electrical and optical configuration of the KTN scanner in our experiment.

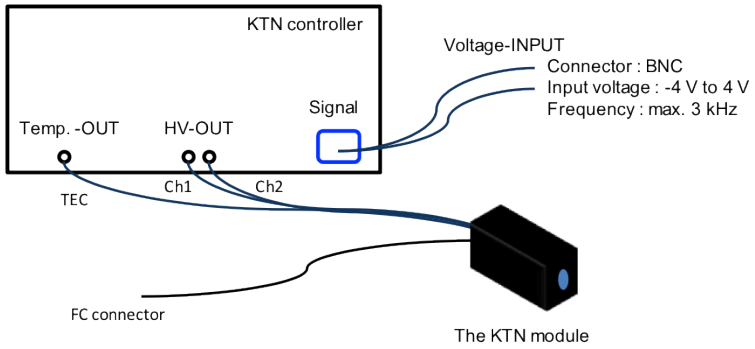

Figure 5.4: Structure of the KTN scanner

Every crystal is packaged into a temperature-controlled module so that their temperature can be individually adjusted by the TEC output of the controller, which ensures that the crystals are always in the cubic phase [12]. The temperature for each crystal and their capacitance is listed below:

Table 5.1: KTN 2-D module operating temperature

Ch#	Preset Temperature	Capacitance
1(Vertical)	42.0 ℃	2.00 nF
2(Horizontal)	45.0 ℃	2.00 nF

The controller also takes input signal and amplifies it 100 times and output to the HV-OUT, providing the driving voltage to the electrode sandwiching the crystals. And the system maximum

driving voltage was +/-400 volts and the bandwidth was 3 KHz.

The following figure shows the deflection angle versus the applied voltage for this deflector.

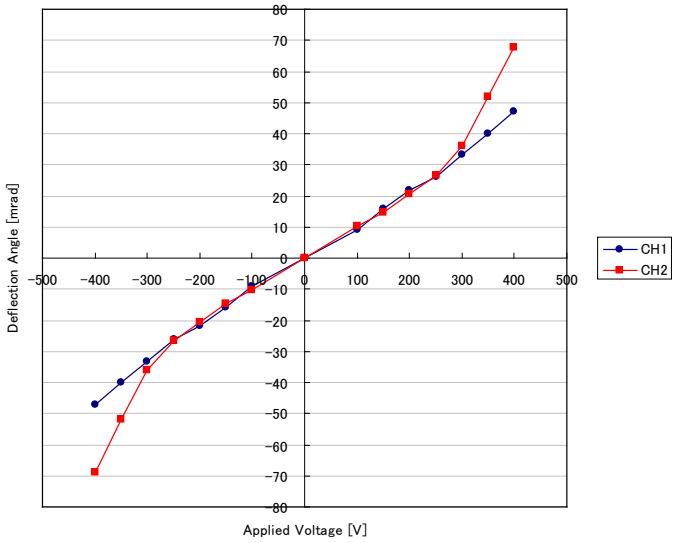

Figure 5.5: Deflection angle versus applied voltage

With the maximum driving voltage, we were able to achieve a maximum deflection angle of 140 mrad, which is equal to 8 °.

As explained before, since there exist the electron injection into the crystal, one might consider the current consumption of this deflector. In fact, the consumed current is mainly due to the capacitance of the crystals, which means that the current inside the KTN crystal is negligible compared with the driving current of the capacitor. In our application, the driving frequency is usually below 100Hz, which results in a current about 1uA. The dependence of the current and working frequency is plotted below.

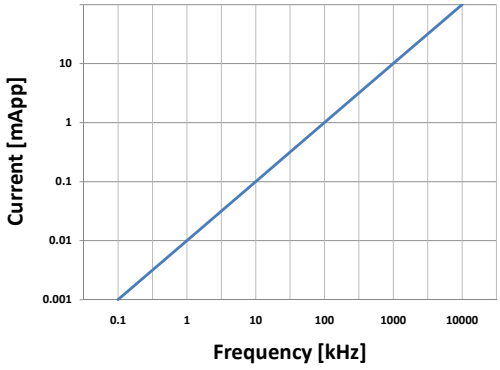

Figure 5.6: KTN crystal current consumption

The major challenge of building such a system is the focusing optics. This is because the output

beam size from the crystal is 500 micron. And the largest magnification of currently available scanning objective is about 10x. This combination yields a lateral resolution around 80 microns. This does not only make the lateral resolution much larger than the axial resolution but also result in a small object-side NA. This reduces the light collection from sample thus significantly decreases the system sensitivity.

Therefore, a set of relay telescope has been designed and implemented to solve this problem. The schematics is shown below:

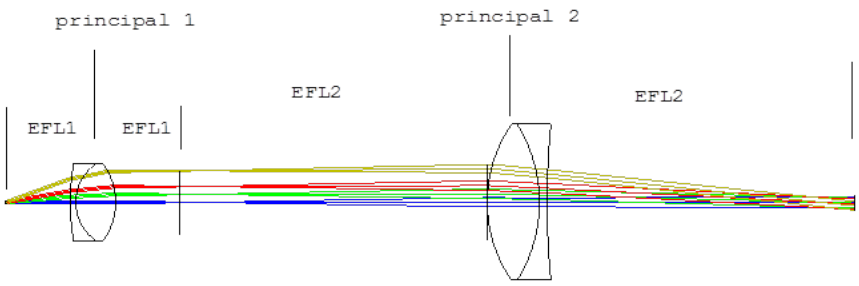

Figure 5.7: The relay telescope for bench top KTN OCT setupn

In this design, we used two achromatic lenses to build a conjugate optics. By overlapping the back focal plane of the two lenses and placing the pivot point of the KTN at the front focal plane of the lens with shorter focal length, the system essentially reproduce the original pivot point with a magnification equal to the ratio of the focal lengths of the two lens. In our experiment, we selected a combination of 250mm and 60mm, yielding a magnification of 4.16. After this relay telescope, we placed a scanning objective to focus light to its working distance. In the following demonstration, we selected the LSM02 - 10X OCT Scan Lens (EFL=18 mm) from Thorlabs Inc. A photo of the bench top system is shown below:

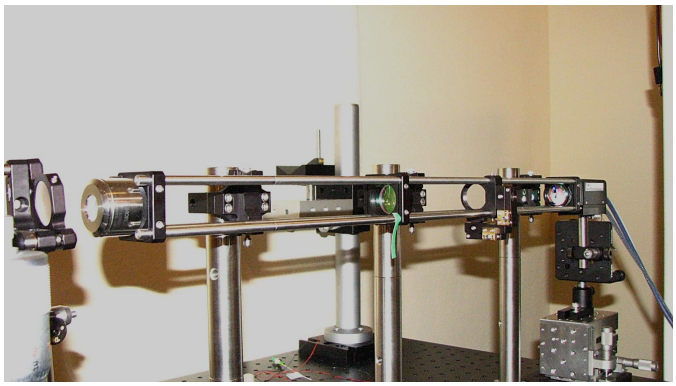

Figure 5.8: Photograph of the bench top relay telescope

In this study, we built a MI/MZI hybrid interferometer as shown below. In this design, the sample arm appears to be of a Michelson type interferometer, but the reference arm appears to be of a Mach–Zehnder type interferometer. Therefore, we eliminate the reflection mirror and associated free space optics and make the entire setup more portable and robust.

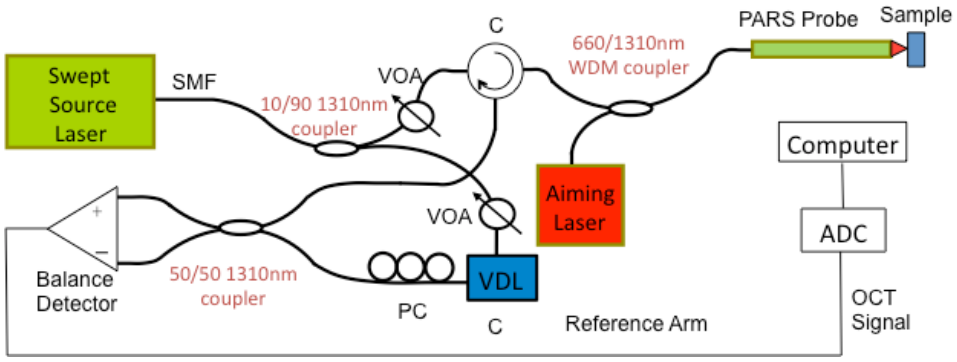

Figure 5.9: Swept source OCT setup used in the KTN experiment

5.4 Proof-of-Principle Experiments

To examine the bench-top KTN OCT system, we carried two types of investigations: system characterization and biological sample imaging.

5.4.1 System characterization

First, we measured the maximum reflected power from the sample arm via a circulator when a plane mirror is placed in front of the objective. Generally speaking, the reflected power peaks where the mirror is placed at the waist of the beam with its surface normal aligned to the beam optical axis. Therefore, this measurement allowed us to find the focal plane of the probing beam.

Table 5.2: Reflected power measurement

Location $[mm]$	0	0.5	1	*1.03 (Focus)*	1.5	2	2.5	3
Power $[dBm]$	-10.20	-10.57	-9.72	*-9.44*	-10.70	-12.58	-15.47	-16.82

Table 5.2 shows the result of this measurement. The origin of this measurement is at a distance of 6.7 mm to the front edge of the objective. Therefore, we found the best reflection occurred at 7.7 mm from the objective. The result also indicates that the falloff of reflection profile along the

beam propagation direction is less than 7.5 dB for the entire 3 mm imaging range. This profile is more flatter than those of typical endoscopic needle probes[13].

Next, we employed a beam profiler (`BeamMap2-4XY-InGaAs, Dataray Inc.`) to measure the beam profiles along the optical axis. The results are shown in Fig. 5.10.

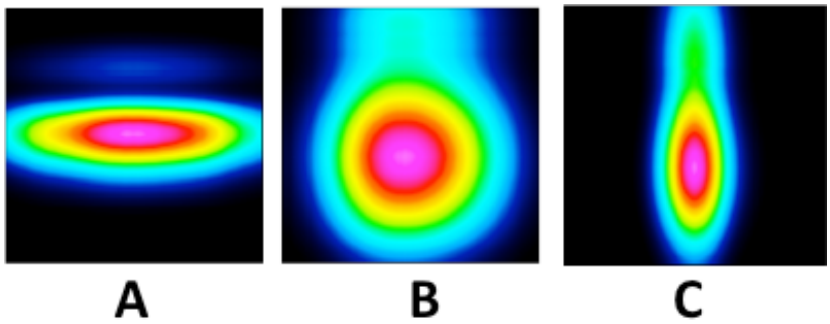

Figure 5.10: Profile of the bench top KTN OCT probing beam. A: The narrowest Y width was measured to be about 25μm. B: The profile where both X and Y width measured to be 44μm. C: The narrowest X width was measured to be about 24μm. Distance: O-A 5.66mm; A-B 1.72mm; B-C 1.05mm. O: the location of the objective.

Fig. 5.10 actually discloses the detail structure of the output beam from the system. We can clearly see the beam has significant astigmatism. Profile A was measured at a distance of 4.66 mm to the objective where the vertical width of the beam reaches its minimal around 25 μm. While the beam continues propagating, the vertical width expands wider but the horizontal width starts shrinking. Profile B was measured at the location where the two width were equal to around 44 μm. Profile B was measured to be 6.3 mm away from the objective. After passing this *'equal-point'*, the vertical width continues increasing and the horizontal width decreasing. At Profile C, 7.3 mm away from the objective, the horizontal width reached its minimal around 24 μm. After passing C, the beam diverges along both directions.

The effect of this astigmatism has two folds. First, as shown above, it introduces non-symmetric PSF for the depth resolved image, which results in resolution difference along two directions of the cross-section. This might potentially distort some features of the samples under test. At the same time, it might reduce the light collection efficiency due to the narrowed effective capture angle. This will cause a decrease on system sensitivity. However, we also notice the fact that both beam widths (vertical and horizontal) were below 40 μm for a rather long depth (2.7 mm). This distance is almost equal to the typical imaging window of current OCT systems commercialized. This indicates that, on the other hand, the astigmatism in fact helps extend the depth of field.

To study the overall system performance, we inspected its PSFs at different imaging depths. As compared in Fig. 5.11, all the PSFs keep a good integrity over the entire imaging window. The maximal reflected power is also plotted as the black line. The falloff between 1 mm and 2.5 mm is

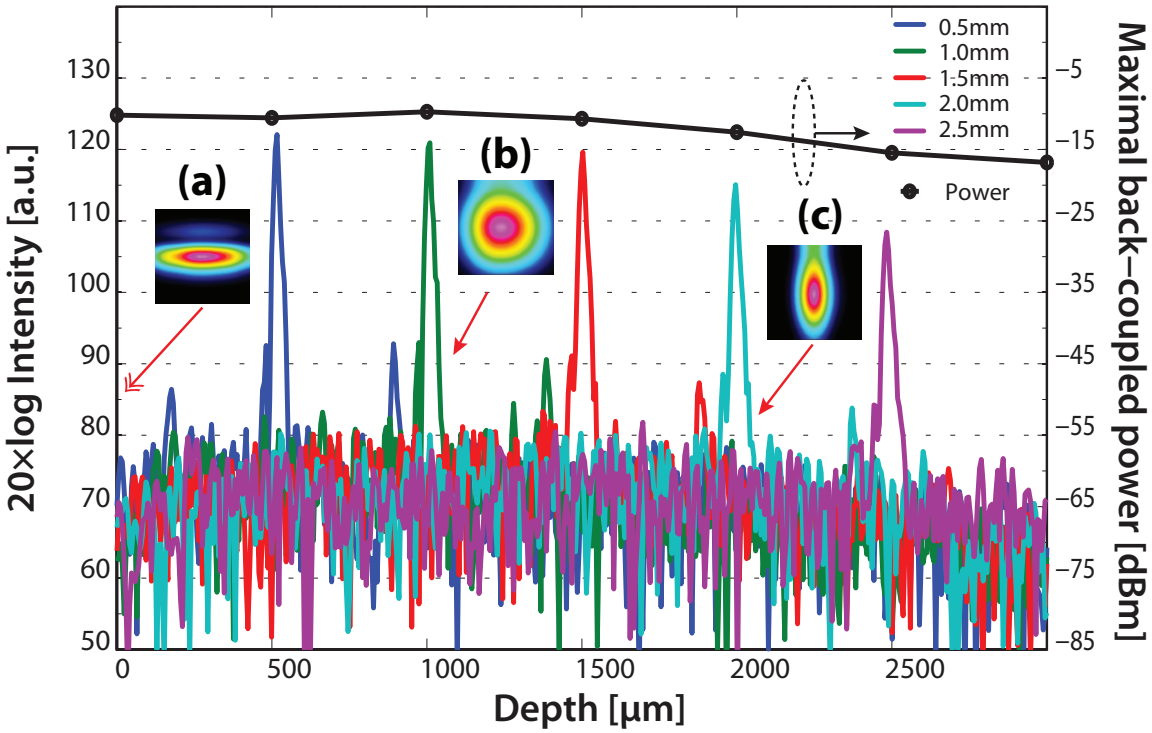

Figure 5.11: Point spread functions of the KTN OCT system. The black line represents the maximal reflected power. Insets (a)∼(c) are the beam profiles measured at three different depths.

$\sim 14\,dB$, which consists of two contributions. First the inherent coherent falloff was measured to be $\sim 7\,dB$. As read from the black line, the decreased reflected power adds to another $\sim 7\,dB$ drop. The insets also show the beam profiles at three different locations. One can see it evolve from a horizontal-oriented ellipse to a circle and to a vertically-oriented ellipse eventually. This manifests its astigmatism. We also notice that the highest PSF, the strongest reflections occurs roughly at the location of *'equal-point'* where the widths along two directions are equal (Fig. 5.10.B). It is worth noting that these PSFs plotted in Fig. 5.11 are generated after dispersion compensation using the approach discussed in Chapter 6.

We further characterized the beam quality when it gets deflected to different angles by the KTN crystal. Because of the beam astigmatism, Fig. 5.12 depicts the beam waists of the horizontal direction under different applied voltages, while that of the vertical direction has a similar behavior. As represented as the blue line, the FWHM of the beam waist ranges from $38\,mm$ to $25\,mm$. The beam waist of the vertical direction sits in another location along the optical axis closer to the objective but has a similar range as can be anticipated from Fig. 5.10 and Fig. 5.11. Besides the reasonable narrow beam width this system offers, the insets in Fig. 5.12 also prove that the probing beam has kept a good integrity when scanning across different angles with different applied voltages.

Rayleigh length is another measure of the beam. It is the distance along the optical axis between the waist and the plane where the cross section area is doubled[14]. An illustration of Rayleigh length

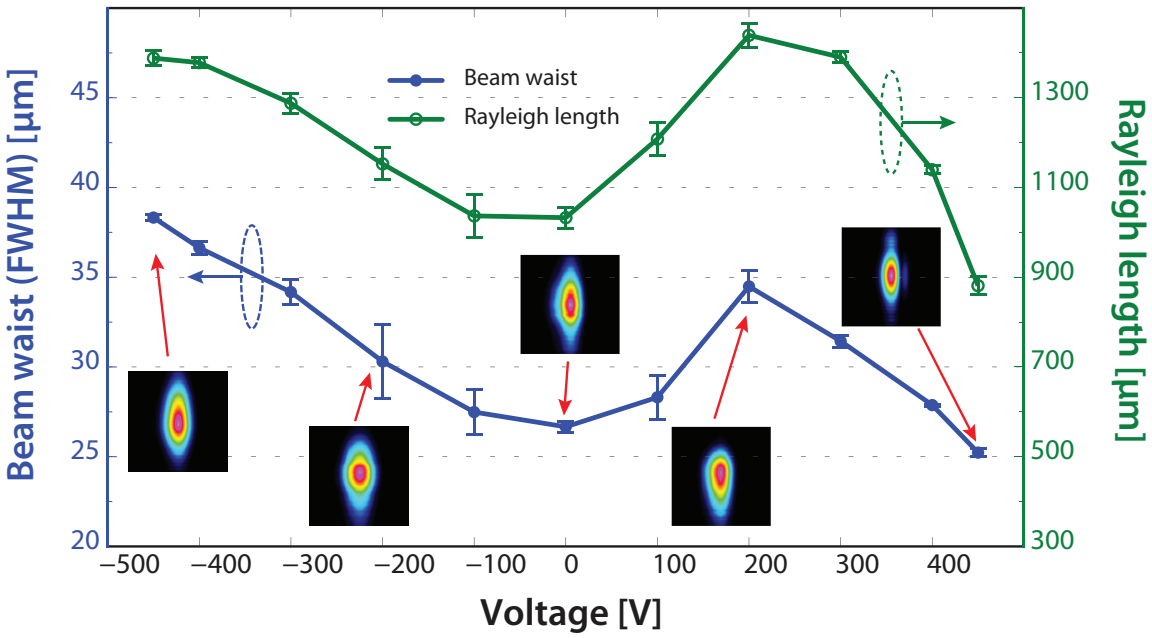

Figure 5.12: Beam quality of the KTN OCT system. The blue line is the FWHM of the horizontal beam waist. The green line is the Rayleigh length. Beam profiles at several selected locations are displayed in insets.

and other parameters under a Gaussian beam case is shown in Fig. 5.13 [15].

The relationship between the Rayleigh length and the beam width is expressed in Eq. (5.10), where z_R is the Rayleigh length, ω_0 is the beam width, and λ is the wavelength.

$$z_R = \frac{\pi\omega_0^2}{\lambda} \tag{5.10}$$

This quadratic relationship between z_R and ω_0 can be appreciated as the multiplicative effect of two facts: First, ω_0 is reverse-proportionally related to the spread angel Θ. Second, the area of the

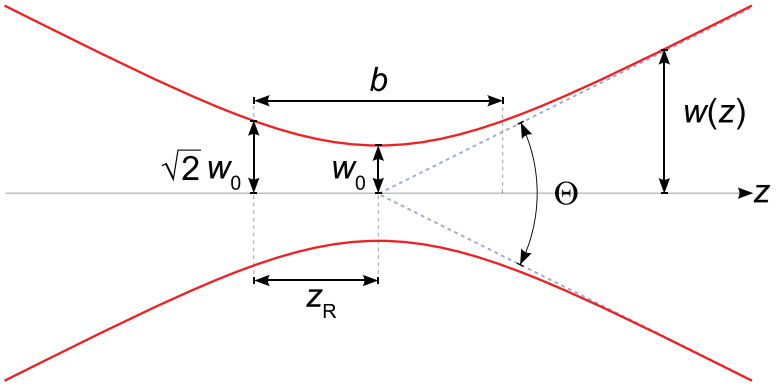

Figure 5.13: Gaussian beam width $\omega = (z)$ as a function of the axial distance z. ω_0: beam waist; b: confocal parameter; z_R: Rayleigh length; Θ: total angular spread

cross-section where z_R locates is obviously linearly related to ω_0, as shown in Fig. 5.13.

This relationship has also been manifested in Fig. 5.12. The green line shows the measured Rayleigh length of the probing beam under different voltages. It varies roughly from $1.4\,mm$ to $0.9\,mm$. Despite the inaccuracies of the measurement, which is represented as the corresponding error bars associated with both FWHM line and Rayleigh length line, the trends of Rayleigh length and beam width agree with that anticipated from Eq. (5.10). Here, we also want to mention the definition of the beam width ω_0 in Eq. (5.10) is different from FWHM. It is defined as $1/e^2$ width, which represents the radius where the optical intensity drops the $1/e^2$ of its peak value. And the two widths are related as Eq. (5.11).

$$2\omega_0 = \frac{\sqrt{2}\text{FWHM}}{\sqrt{\ln 2}} \approx 1.699 \times \text{FWHM} \tag{5.11}$$

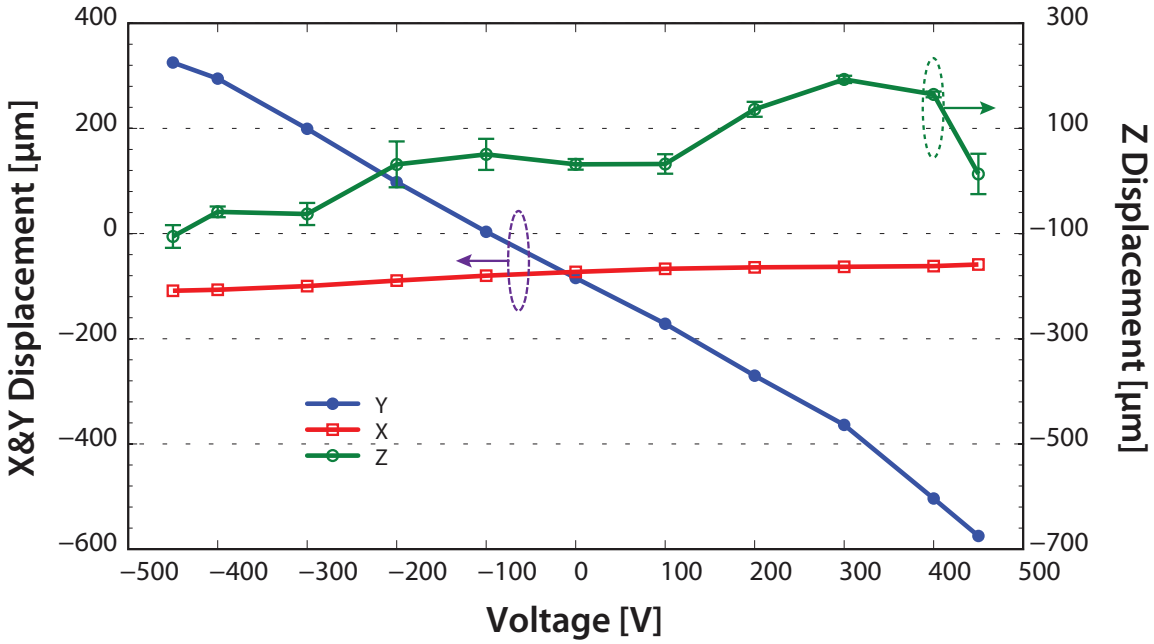

Figure 5.14: Beam focus displacements of the KTN OCT system. The red line is the displacement along X direction. The blue line is the displacement along Y direction. The green line is the displacement along Z direction. Notice that despite of the different offsets, the scales of the two vertical axis are the same.

We also investigated the spatial trajectory of the beam focus when scanning. This information will not only disclose the lateral scan pattern (displacement along X and Y directions) but also the shift of the working distance (displacement along Z direction) of the scanning system. The results are plotted in Fig. 5.14. The X and Y displacements measurement were very accurate with negligible variances. The measurement along Z direction is inherently less precise in practice, which is quantified by the measurement variance shown as the error bars. The scales of the two vertical axis are set to be identical so that it is easy to fairly compare the displacements along all three

axis and enables a good visual perception. As plotted as the blue line in Fig. 5.14, the major scan direction is Y, along which the beam scans over a distance of $970\,\mu m$. This value defines the field of view of the current system. Another important feature is that the displacement along Y is almost linearly related to the applied voltage, while there dose exhibit a minor saturation effect in the region where the applied voltage $> \pm 450\,V$. There was a minor displacement ($< 100\,\mu m$) along X direction as well. It is due to the slight misalignment between the coordinates of the scanner and that of the measurement plane. The displacement behavior along Z direction is very informative as well, as drawn in the green curve. It does have a maximal variance of $\sim 300\,\mu m$, which indicates some drift of the working distance while scanning. This shifting of beam focus will introduce some nonuniformity to the lateral resolution of cross-sectional images. But considering the imaging depth is $3\,mm$ ($10\times$ of the maximal variance), the impairment is minor. The angle dependency of lensing effect of the crystal can account for this effect. Further study will be necessary to provide a more in-depth understanding of this phenomena.

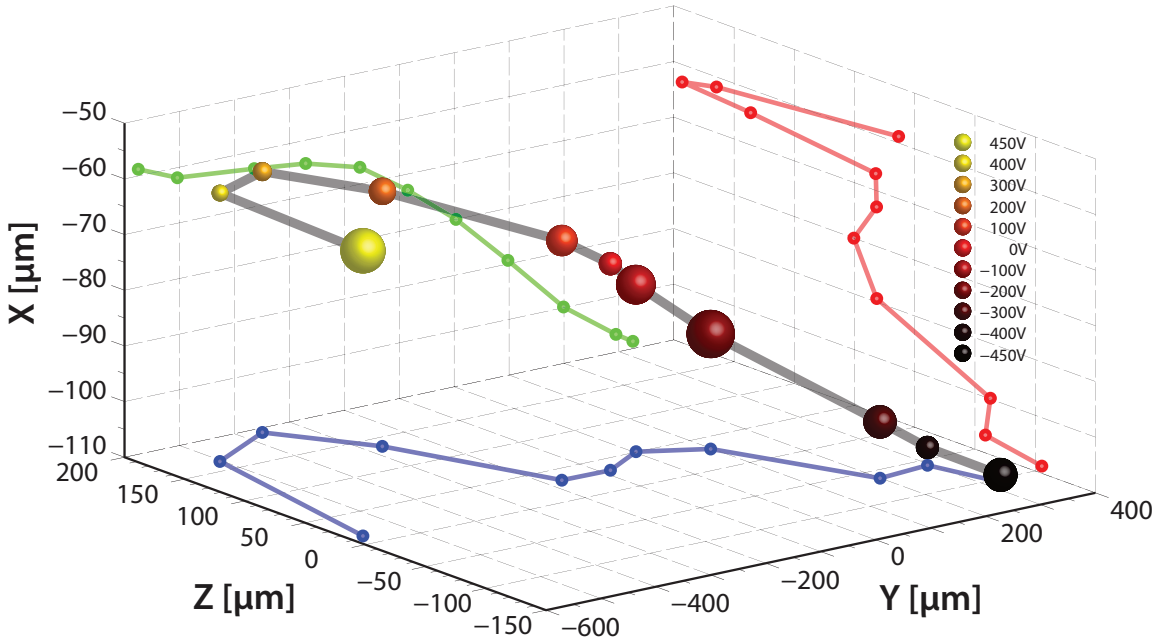

Figure 5.15: Beam focus trajectory of the KTN OCT system. The black line is the actual trajectory in 3D. The blue line is the projection of the trajectory onto the YZ plane; the red line is the projection of the trajectory onto the XZ plane; the green line is the projection of the trajectory onto the XY plane. The radius of the data spheres represents the relative measurement variance. Notice that the scales for the three axis have been adjusted individually to show the trajectory with optimal visualization

A 3D rending of the trajectory is also included in Fig. 5.15 to better visualize the actual beam scanning in action. While the black line presents the 3D trajectory of beam focus while scanning, the blue, red, and green lines are its projections onto YZ, XZ, and XY respectively. The scales of X and Z axis have been intentionally adjusted to zoom in the detail feature of the trajectory, which

otherwise will be nominated by the displacement along Y direction thus difficult to be disclosed. The radius of the data spheres symbolizes the relative measurement variance, which is estimated as the l_2 norm of the standard deviation of the measured displacements along all three directions, as expressed in Eq. (5.12).

$$\text{Radius} = \sqrt{\text{STD}_X^2 + \text{STD}_Y^2 + \text{STD}_Z^2} \tag{5.12}$$

5.4.2 Biological sample imaging

After the examination of the probing beam, we imaged several biological samples with this KTN OCT system to check its imaging capability. We first imaged human finger skin.

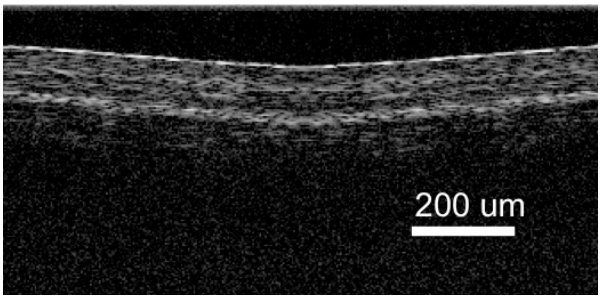

Figure 5.16: Human finger skin OCT image by KTN scanning

The above figure shows the layer structures clearly. And we next imaged the ex-vivo retina from a porcine eye.

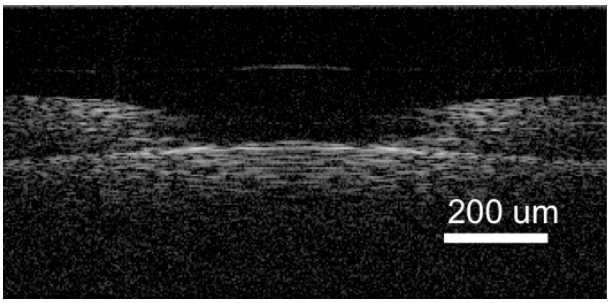

Figure 5.17: OCT image of a ex-vivo porcine eye retina

This image depicted the folded retina layer and even shows the interface between the vitreous remnant and air, which is very instructive for vitrectomy procedure. We further applied this imaging system to a 54-stage Xenopus-lavies tadpoles. In the following figure, we show several images of the tadpole's gill structures and cardio system. The top row images are the raw image obtained directly from the KTN OCT system. The bottom row images are the images after dispersion compensation. As one can see, the uncompensated images were all distorted heavily and could not disclose any

useful information of the sample. On the other hand, after compensation, the images show clearly the desired physiological structures. This sharp comparison tells us the importance of dispersion compensation and the need to build a data processing engine that can compensate dispersion in real time so that user can get feedback in a timely manner. The detail of the dispersion compensation technique will be discussed in next chapter.

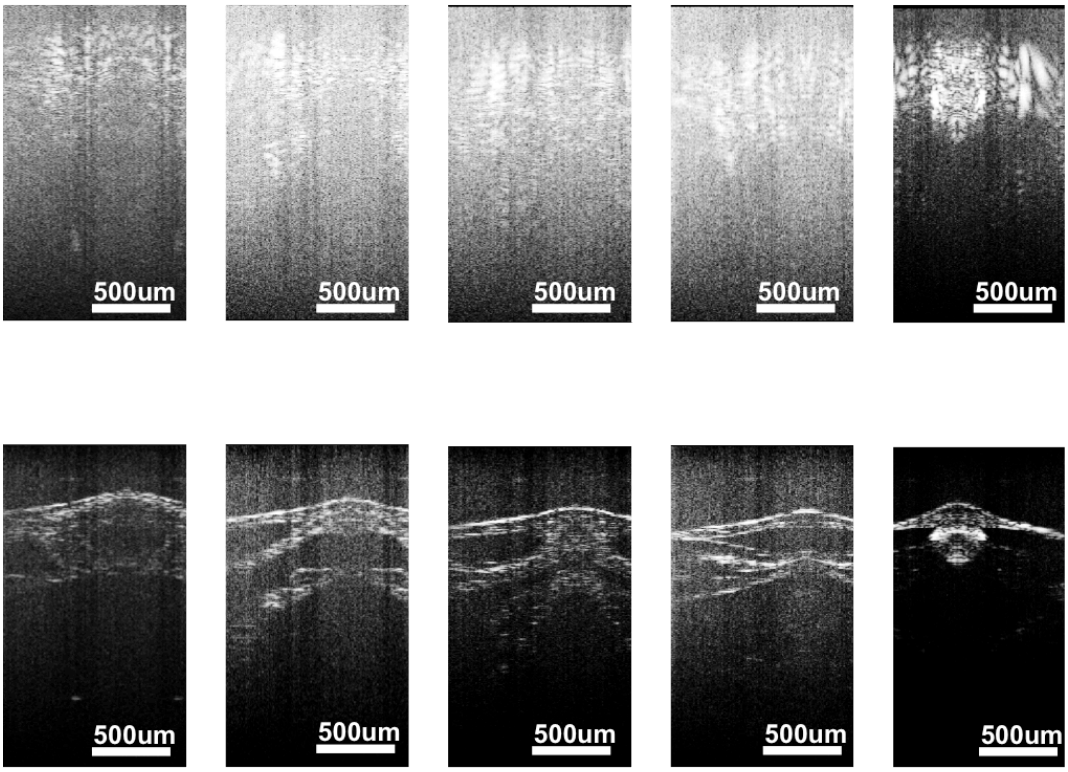

Figure 5.18: OCT images of a 54 stage Xenopus laevis tadpole by the bench top KTN system. Top row shows the raw images; bottom row shows the dispersion-compensated images

5.5 Design of Endoscopic KTN Probe

The above experiments have demonstrated the major advantages of this non-mechanical scanning method. Combining all of its merits, we can produce a new type of endoscopic OCT probe based on KTN crystal.

Figure 14 illustrates a schematics of such a probe. The prototype consists of three major elements: collimating optics, KTN crystal, and focusing optics. The collimating optics is used to collimate the beam coming from the delivery optical fiber and provide a plane-wave like beam input to the next stage. Then the KTN deflector steers the collimated beam in a pre-programmed manner. The deflected beam will then be passed through the last element. The design of the focusing optics should have many varieties depending on the desired scanning requirements.

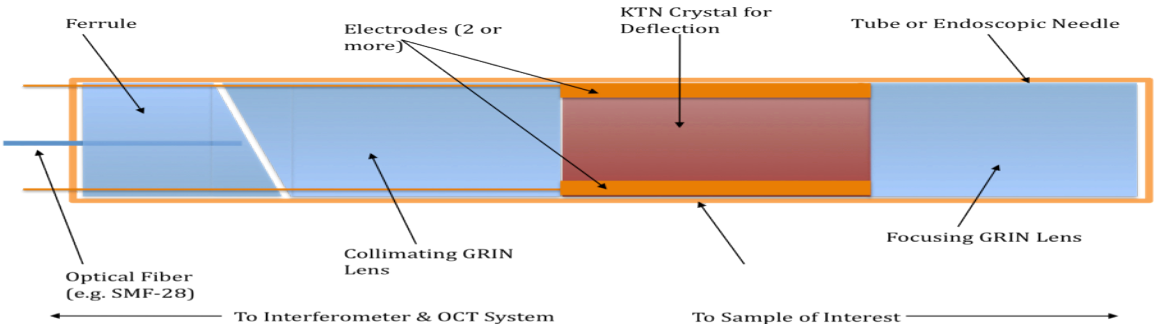

Figure 5.19: Schematics of endoscopic probe based on KTN deflector

In order to encase all elements into a small diameter probe, we choose GRIN lens as the major building block for collimating and focusing optics. The collimating optics can be relatively standard since one can always use a quarter pitch GRIN lens to connect the end of the delivery fiber and collimate the incoming beam. It is worth mentioning that extra half pitches might have to be added to the quarter pitch in some designs. This is because that the physical length of quarter pitch GRIN lens might be too short to make a robust mechanical structure and the very short piece of GRIN also increases the difficulties of fabrication. The NAs of the GRIN lens are usually larger than that of the delivery fiber. In order to improve the final resolvable points and make most of the cross-section of the KTN crystal, we very often need to make the size of the collimated beam equal to that of the crystal.

The design of the focusing optics should have many varieties depending on the desired scanning requirements. Several parameters are of great interest, which include working distance, spot size, and depth of focus. They are all correlated as design tradeoffs. Usually smaller spot size (better lateral resolution) comes with shorter working distance and shallower depth of focus. When design a KTN based endoscope, we need to first determine the optical requirement for a specific application and decide the desired value for those parameter, then optimize them accordingly.

References

[1] F. S. Chen, "Light Modulation and Beam Deflection with Potassium Tantalate Niobate Crystals," en, *Journal of Applied Physics*, vol. 37, no. 1, p. 388, Jan. 1966 (cit. on p. 61).

[2] K. Nashimoto, S. Nakamura, T. Morikawa, H. Moriyama, M. Watanabe, and E. Osakabe, "Fabrication of electro optic PbZr, TiO3 heterostructure waveguides on Nb doped SrTiO by solid phase epitaxy," *Applied Physics Letters*, vol. 74, no. 19, p. 2761, 1999 (cit. on p. 61).

[3] D. A. Scrymgeour, Y. Barad, V. Gopalan, K. T. Gahagan, Q. Jia, T. E. Mitchell, and J. M. Robinson, "Large angle electro optic laser scanner on LiTaO3 fabricated by in situ monitoring of ferroelectric-domain micropatterning," *Applied Optics*, vol. 40, no. 34, p. 6236, 2001 (cit. on p. 61).

[4] S. Hisatake, K. Shibuya, and T. Kobayashi, "Ultrafast traveling wave electro optic deflector using domain engineered LiTaO3 crystal," *Applied Physics Letters*, vol. 87, no. 8, p. 081 101, 2005 (cit. on p. 61).

[5] S. Triebwasser, "Study of Ferroelectric Transitions of Solid-Solution Single Crystals of KNbO3-KTaO3," *Physical Review*, vol. 114, no. 1, pp. 63–70, Apr. 1959 (cit. on p. 61).

[6] J. A. VAN RAALTE, "Linear Electro-Optic Effect in Ferroelectric KTN," *Journal of the Optical Society of America*, vol. 57, no. 5, p. 671, May 1967 (cit. on p. 61).

[7] W. Haas and R. Johannes, "Linear Electrooptic Effect in Potassium Tantalate Niobate Crystals," *Applied Optics*, vol. 6, no. 11, p. 2007, Nov. 1967 (cit. on p. 61).

[8] H. B. Michaelson, "The work function of the elements and its periodicity," *Journal of Applied Physics*, vol. 48, no. 11, p. 4729, 1977 (cit. on p. 61).

[9] K. Nakamura, J. Miyazu, M. Sasaura, and K. Fujiura, "Wide angle, low voltage electro optic beam deflection based on space charge controlled mode of electrical conduction in KTa[sub 1-x]Nb[sub x]O[sub 3]," *Applied Physics Letters*, vol. 89, no. 13, p. 131 115, 2006 (cit. on p. 62).

[10] K. Nakamura, J. Miyazu, Y. Sasaki, T. Imai, M. Sasaura, and K. Fujiura, "Space charge controlled electro optic effect: Optical beam deflection by electro optic effect and space charge controlled electrical conduction," en, *Journal of Applied Physics*, vol. 104, no. 1, p. 013 105, Jul. 2008 (cit. on p. 62).

[11] BONNER, WA, DEARBORN, EF, and VANUITER.LG, "GROWTH OF POTASSIUM TANTALATE-NIOBATE SINGLE CRYSTALS FOR OPTICAL APPLICATIONS," vol. 44, no. 1, 1965 (cit. on p. 62).

[12] D. Rytz and H. Scheel, "Crystal growth of KTa1-xNbxO3 (0 x 0.04) solid solutions by a slowcooling method," *Journal of Crystal Growth*, vol. 59, no. 3, pp. 468–484, Oct. 1982 (cit. on p. 65).

[13] J. Wu, M. Conry, C. Gu, F. Wang, Z. Yaqoob, and C. Yang, "Paired-angle-rotation scanning optical coherence tomography forward-imaging probe," *Optics Letters*, vol. 31, no. 9, p. 1265, May 2006 (cit. on p. 69).

[14] A. E. Siegman, *Lasers*. University Science Books, 1986, p. 1283 (cit. on p. 70).

[15] Wikipedia, *Rayleigh length* (cit. on p. 71).

Chapter 6

Dispersion Compensation Techniques for KTN Based OCT Systems

This chapter is to present an investigation on the techniques of dispersion compensation for KTN based OCT system. The results actually can be generalized to a generic optical interferometer.

6.1 Chromatic Dispersion and Its Effect in OCT systems

Chromatic dispersion mismatch between the two arms of an optical interferometer has been a critical concern that needs to be addressed for many wideband applications. For example, the axial resolution of optical coherence tomography (OCT) systems will be impaired by the unbalanced dispersion between the reference and the sample arms[1]. Multiple methods have been proposed and implemented to mitigate these negative effects. Those approaches can be divided into two major categories: physical compensation and numerical compensation, where the former one involves using an extra tunable dispersive device to balance the mismatch[2], while the latter one usually employs a post-process algorithm to make corrective operation on the acquired signals[3–5]. While physical compensation often provides a fast solution without any extra computation cost, it generally requires an extra optical element to be inserted into the setup and the residue high order dispersion mismatch could be a problem for ultra-wide band applications. This Letter is to present an analysis on dispersion mismatch estimation for numerical compensation and propose a polynomial fitting based approach. In our experimental demonstration, the method reduced the computation complexity and improved the estimation accuracy. The method is suited for systems where a significant specular reflection is achievable.

To analyze the dispersion mismatch between the two arms of an interferometer, a wideband light source or a scanning laser can be employed as the input and the output intensity interference fringes can be acquired spatially by using a spectrometer and an array of optical detectors, such as

CCD or temporally by one single high-speed photodetector, such as PIN diode. The phase profile of the fringes in wavenumber domain (k domain) around k0 at the center of the spectrum can be approximated as a Taylor series, as shown below:

$$\Phi(k) \approx \Phi(k_0) + \left.\frac{\mathrm{d}\Phi}{\mathrm{d}k}\right|_{k_0} (k-k_0) + \frac{1}{2}\left.\frac{\mathrm{d}^2\Phi}{\mathrm{d}k^2}\right|_{k_0} (k-k_0)^2 + \cdots + \frac{1}{n!}\left.\frac{\mathrm{d}^n\Phi}{\mathrm{d}k^n}\right|_{k_0} (k-k_0)^n \tag{6.1}$$

If the fringe is caused by a specular reflection and the optical path difference between the arms comes from a single dispersive sample, then $\Phi(k)$ can be simplified as: $\Phi(k) = L\beta(k)$, , where L is the sample length and $\beta(k)$ is its lightwave propagation constant. Since L is constant, $\Phi(k)$ is actually a polynomial of k whose coefficients represent the derivatives of the propagation constant $\beta(k)$. The slope of the phase profile, the first order coefficient of the polynomial, can be derived as $cL(\,\mathrm{d}\beta/\,\mathrm{d}\omega) = cL/v_g(k)$ where c is the light speed in vacuum, ω is the angular frequency, and v_g is the group velocity. In fact this slope represents the group delay. If the group velocity is constant, the slope represents the physical length L. This is the basic prerequisite for Fourier Domain OCT (FD-OCT) systems. On the other hand, if L is fixed, the slope then represents the group velocity. This enables us to measure the dispersion mismatch.

6.2 Method of Dispersion Estimation for Wide-band Optical Interferometers

A numerical dispersion compensation method for FD-OCT systems based on Hilbert transform was proposed[6] and has been broadly implemented since then[7, 8] due to its simplicity and effectiveness. This type of methods search the best coefficients a2 and a3, (effectively the second $(1/2)(\,\mathrm{d}^2\Phi/\,\mathrm{d}k^2)|_{k_0}$ and the third order $(1/6)(\,\mathrm{d}^3\Phi/\,\mathrm{d}k^3)|_{k_0}$) coefficients of Eq. 6.1, based on a certain sharpness metric function. The optimal coefficients maximize the metric function, making the images sharpest. As sharpness is a rather qualitative description of an image, multiple metric functions can be constructed subjectively for different criterions, such as the total number of points in its axial (A) scan over a predefined threshold[6]. Another criteria can be to maximize the amplitude of the most significant spike.

This type of image sharpening based methods is particularly suitable for the applications where a significant specular reflection is impossible to create. However, they have several significant drawbacks. First, the criteria behind the metric functions are phenomenological and do not directly originate from the physical nature of dispersion.

In fact, different subjectively selected metric functions yield quite different optimized a2, a3. It could be difficult to tell which one is closer to the real dispersion. Second, as will be demonstrated

later, the searching process can easily reach local optimals for simple metric functions. Thus a careful selection of the searching range and step is critical. A sophisticated metric function based on information entropy was demonstrated to have a smoother profile[9]. However, it has to reply on computation on cross-section images thus the results can be suspectible to scanning mechamism and sample structures. Lastly, to increase the chance that a search can eventually find the global optimal, a wide range of a2 and a3 has to be covered and the computation cost can be substantial. This makes dynamic dispersion compensation difficult.

For the applications where there exists a significant specular reflection, such as the foveal surface in human eyes, or where an external specular refection can be introduced for calibration, the above problems can be well solved by using a polynomial fitting method. This method is based on the idea that a polynomial fitting of the phase profile yields the best estimation of the coefficients in the Taylor expansion (Eq. 6.1) in the least squared sense. Similar to the previous approach, this fitting method also utilizes the Hilbert transform to abstract the phase profile from the interference fringes. However, the abstracted phase is the wrapped principle value due to the 2 ambiguity. Therefore, a critical step is to unwrap the acquired phase profile to restore the actual phase profile accumulating along the entire band. Next, one can then apply a polynomial fitting to the unwrapped phase profile and obtain the estimated coefficients. As discussed earlier, the coefficients are related to the derivatives of propagation constant , representing properties of dispersion mismatch. Specifically, the second order coefficient is linearly related to the group velocity dispersion (GVD) parameter D, as expressed below:

$$D = \frac{\mathrm{d}\beta}{\mathrm{d}\omega \cdot \mathrm{d}\lambda} = -\frac{\mathrm{d}^2\Phi}{\mathrm{d}k^2}\frac{2\pi}{cL\lambda^2} \tag{6.2}$$

where λ is the wavelength. The above relationship suggests that this method can be practically used to measure dispersion properties of unknown material when being placed in the arms of an interferometer.

6.3 Measurement and Numerical Compensation in KTN Crystal

To test the above method, we built a swept source OCT system. The swept laser was centered at 1310nm with a wavelength scanning range of about 100nm and a scan rate of 5KHz. We introduced an initial dispersion mismatch by placing in the sample arm a small piece of potassium tantalate niobate [KTa1?xNbxO3(KTN)] crystal. The physical path length in the crystal was 12mm. The setup was mostly fiber based and did not contain any dispersion compensation element. The overall dispersion mismatch between the two arms can be primarily attributed to the KTN crystal and an

objective lens in the sample arm since the GVD parameter D of glass fiber (Corning SMF-28) reaches its minimal around 1310nm. The method can be applied to the systems with pre-compensation where the mismatch might come from different elements though.

A plane mirror was used to provide a single specular reflection at the sample arm. We measured the OCT fringe signals generated by the mirror at two different axial positions. At each position, the fringes for two different polarization states of the probing beam were collected to examine the polarization dependence of the dispersion. To study the dispersion of the two elements (the KTN crystal and the objective lens) individually, we also measured the fringe signal without the lens.

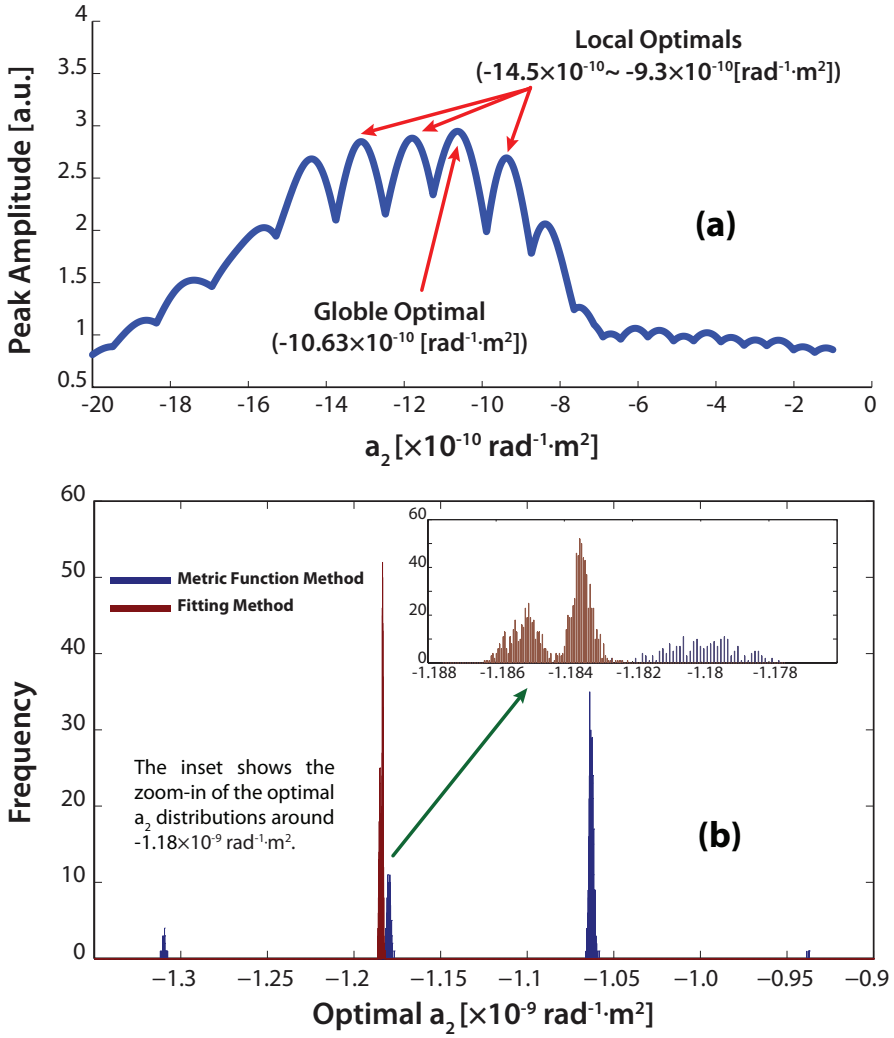

Figure 6.1: Instability of metric function based methods (a) the global and local optimal values (b) the comparison of the optimal coefficient histograms by both methods.

To compare the searching method based on metric functions and the polynomial fitting method, we applied both to the acquired data sets. For a fair comparison, only the second and the third order coefficients were estimated. In Figure 1(a), a typical metric function of a2, defined as the peak

amplitude of the spike generated by the mirror, is plotted and was used as an example throughout this study. One can clearly see that it contains rather complicated structure and is non-monotonical. More importantly, this function has multiple local optimal values spaced densely together with the global optimal over a considerable wide range. This indicates that if the searching range is not wide enough or the step is not fine enough, the searching would have a substantial chance to end up with one of these local optimums. And it would be difficult to select an appropriate set of the range and the step that can ensure a successful finding of the global optimal value for an unknown dispersion mismatch. On the other hand, if an excessively wide range and an exaggeratively fine step are used, the added computation can be substantial. In addition, for ultra-wide band applications where higher order dispersion need to be considered, the joint search for multiple coefficients increases the computation complexity exponentially.

Even if the global optimal was found for one fringe data, the dense distribution of local optimal values suggests that the found optimal value is highly sensitive to measurement noise. The found optimal value can switch among several local optimal values when the disturbance from external noise exists. This effect has indeed been disclosed in our experimental results. Fig. 1(b) shows a comparison between the histograms of the optimal a2 estimated by both methods, where we applied them to the same data set of 1024 fringes while the entire setup remained fixed. The distribution of the optimal coefficient from the searching method spans a much wider range than that from the fitting method. It also peaks at several discrete values, indicating this method will likely output different optimal values for the same dispersion mismatch. This instability makes dispersion mismatch measured by this method relatively unreliable when compared to the fitting method.

Table 6.1: GVD Measurements

GVD	Position 1		Position 2	Without Lens
[ps/nm·km]	Polarization A	Polarization B		
Fitting	602.1	604.7	599.4	581.9
Searching	557.1	504.3	574.5	515.1

In Table 6.1 , with the help of Eq. 6.2, we show the averaged GVD measurement by both methods. For the fitting method, the results for different polarization states at Position 1 are very close to each other. This indicates that the overall dispersion properties of the optical elements in the interferometer has weak dependency on polarization, although the KTN crystal exhibits significant birefringence.

The result at Position 2 is also very close to those at Position 1, both yielding a D of around 600 ps/(nm*km) for the KTN crystal at 1310nm range. This is because moving the mirror in vacuum

only results in an extra linear phase profile and has no impact on the second order derivative – GVD parameter D.

On the other hand, for the same three cases, there exists a very large variation of the GVD measured by the metric function method, which once again shows its instability. We also computed the statistics on the results estimated from the 1024 fringes acquired at Position 1 with Polarization A . While the standard deviation for the fitting method is 0.47 ps/(nm*km), that for the metric function method grows much larger – 32.34 ps/(nm*km).

Finally, we notice that there is a relatively small difference 20ps/(nm*km) from the data acquired without the objective lens, which is primarily due to the dispersion of the lens. We can now conclude that the overall GVD of the system was dominated by the KTN crystal.

Upon obtaining the dispersion mismatch, we numerically compensated the broadening of the point-spread function (PSF) of the OCT system. After an ideal compensation, the phase profile caused by a single specular reflection should turn to be a straight line. Given that, we subtracted the second and the third order terms. It was this nonlinearity that resulted in the chirping of the fringe signals and the broadening of the PSF. The phase correction terms are plotted in Fig.Figure 2(a); the corresponding phase profiles after compensation are plotted together with the original unwrapped profile in Fig.Figure 2(b). The PSFs are also compared in Fig.Figure 2(c). While the uncompensated PSF has an effective FWHM of around 92 ?m ?m ; the PSF after fitting method compensation has a width of less than 16 m ?m, which is close to 12 ?m ?m, the original PSF width without the crystal. The difference can be attributed to the residual high order dispersion. We found that the PSF by searching method appears a little wider than that by the fitting method, while it underwent much more computation. In this example, the joint search of both parameters (a2 and a3) took about 20000 times longer than the entire polynomial fitting process.

It is also worth mentioning that the selection of the mirror's location relative to the zero delay point is very important to achieve an accurate measurement. First, the mirror should not be placed very far from that point. It is mainly limited by the finite sampling rate of the system. For those locations, the frequency of the fringe signal might be so high that the actual accumulated phase difference between two adjacent samples is much larger than and the ambiguity during the phase unwrapping procedure is inevitable. When recovering for a wide wavelength range, the resulting phase error of the multiples of 2 accumulates quickly, making the deviation of the unwrapped phase profile unacceptable. Second, the mirror would rather not be placed too close to the zero delay point as well. The actual instantaneous frequency of the fringe signal changes its sign at the frequency where the slope of the phase profile is equal to zero. When this takes place, the phase profile will switch from accumulating phase to dissipating phase or vice versa. However, the phase calculation based on the Hilbert transform will still interpret the dissipating phase as accumulating phase by using its conjugate counterpart, which makes the profile deviates from its actual value. Therefore,

to make a good measurement, the actual phase profile needs to be monotonical and the maximum slope should be less than /?k.

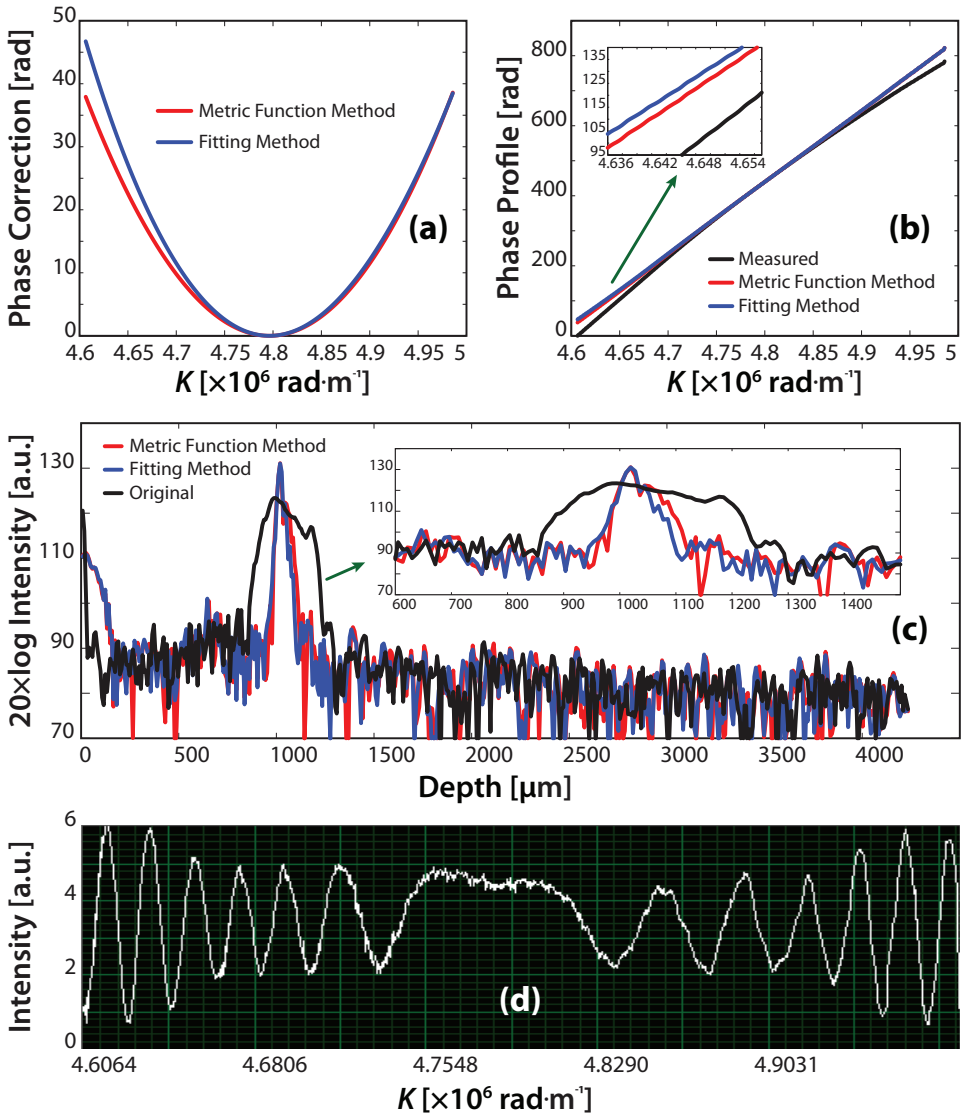

Figure 6.2: Dispersion mismatch estimation. (a) the phase correction (b) the phase profiles (c) the point-spread functions (d) fast dispersion estimation

Although the frequency switching problem in the near zero delay region prohibits the application of the polynomial fitting method, it inspires a fast estimation on the second order coefficient – the GVD parameter D. Figure 5 shows such an example resulting from the OCT system used in this work. One can see that the frequency switching occurs roughly at the center of the wavelength range, which should yield a symmetric quadratic profile for GVD dominating case, which is indeed true for most cases. Counting the number of the periods from the switching point will give a rough estimation on how much phase difference for the half range. Using the simple expression and Eq.

2, one can easily compute a2 and D. For the example shown in Fig.Figure 5 , we can count about 6.5 periods that are equal to 13 . And the ?k for the half wavelength scanning range is about 1.9e5. These give an estimation of D as 576 ps/(km*nm).

In summary, we proposed a polynomial fitting method to estimate dispersion mismatch. Its benefits on both computation complexity and reliability were experimentally demonstrated. This approach can potentially facilitate many applications requiring dynamic dispersion measurement, which include optical imaging, communication, and sensing.

References

[1] C. K. Hitzenberger, A. Baumgartner, W. Drexler, and A. F. Fercher, "Dispersion Effects in Partial Coherence Interferometry: Implications for Intraocular Ranging," en, *Journal of Biomedical Optics*, vol. 4, no. 1, p. 144, Jan. 1999 (cit. on p. 79).

[2] W. Drexler, U. Morgner, F. X. Kärtner, C. Pitris, S. a. Boppart, X. D. Li, E. P. Ippen, and J. G. Fujimoto, "In vivo ultrahigh-resolution optical coherence tomography.," *Optics letters*, vol. 24, no. 17, pp. 1221–3, Sep. 1999 (cit. on p. 79).

[3] J. F. de Boer, C. E. Saxer, and J. S. Nelson, "Stable carrier generation and phase-resolved digital data processing in optical coherence tomography.," EN, *Applied optics*, vol. 40, no. 31, pp. 5787–90, Nov. 2001 (cit. on p. 79).

[4] A. Fercher, C. Hitzenberger, M. Sticker, R. Zawadzki, B. Karamata, and T. Lasser, "Numerical dispersion compensation for Partial Coherence Interferometry and Optical Coherence Tomography.," *Optics express*, vol. 9, no. 12, pp. 610–5, Dec. 2001 (cit. on p. 79).

[5] D. L. Marks, A. L. Oldenburg, J. J. Reynolds, and S. A. Boppart, "Digital Algorithm for Dispersion Correction in Optical Coherence Tomography for Homogeneous and Stratified Media," EN, *Applied Optics*, vol. 42, no. 2, p. 204, Jan. 2003 (cit. on p. 79).

[6] M. Wojtkowski, V. J. Srinivasan, T. H. Ko, J. G. Fujimoto, A. Kowalczyk, and J. S. Duker, "Ultrahigh-resolution, high-speed, Fourier domain optical coherence tomography and methods for dispersion compensation," *Optics Express*, vol. 12, no. 11, p. 2404, May 2004 (cit. on p. 80).

[7] P. Puvanathasan, P. Forbes, Z. Ren, D. Malchow, S. Boyd, and K. Bizheva, "High-speed, high-resolution Fourier-domain optical coherence tomography system for retinal imaging in the 1060 nm wavelength region.," *Optics letters*, vol. 33, no. 21, pp. 2479–81, Nov. 2008 (cit. on p. 80).

[8] K. Zhang and J. Kang, "Real-time numerical dispersion compensation using graphics processing unit for Fourier-domain optical coherence tomography," English, *Electronics Letters*, vol. 47, no. 5, p. 309, Mar. 2011 (cit. on p. 80).

[9] Y. Yasuno, Y. Hong, S. Makita, M. Yamanari, M. Akiba, M. Miura, and T. Yatagai, "In vivo high-contrast imaging of deep posterior eye by 1-microm swept source optical coherence tomography and scattering optical coherence angiography.," *Optics express*, vol. 15, no. 10, pp. 6121–39, May 2007 (cit. on p. 81).

Chapter 7

Conclusion

7.1 Summary

Endoscopic OCT extends to many applications that traditional OCT would never had a chance to explore. These do not only include a high resolution imaging checkup for some organs that other imaging modality, such as ultrasound, CT, or MRI, cannot offer; but also an intraoperative assistance that can provide a real-time guidance during a surgery inside the operation room.

Numerous efforts have been made towards the research and development of OCT endoscopes. Among all different approaches, the core problem of this field is that how to implement beam steering and focusing (thus OCT B scan) within a very limited space. As two basic functional modules, a good amount of methods for light steering and focusing have been well studied in the fields of optics and photonics. Therefore, people keep investigating these methods and their variation in this particular setting, which has huge potential benefits for the society of health care.

As OCT B scan methods evolve, many approaches have been proposed and implemented. They can be divided into two major categories: manual scanning and mechanical scanning. While manual scanning is a very natural way to scan a sample with a hand-held device, mechanical scanning is still the most popular beam steering method in optics. Many mature devices are using galvanic mirrors, polygon mirrors, and acousto-optic deflectors. Modern devices have started to deploy microelectromechanical system (MEMS) apparatus as well.

The research in this thesis has explored both categories. By introducing an optical tracking system, we designed and implemented a hand-held probe. Unlike any mechanically actuated OCT imaging probes, this method tracks the position and orientation of a handheld probe in real time. While the probe is swept over region of interest by a user, the collected A-scans and the time-varying probe position information can be combined to form 2D or 3D OCT images. With great flexibility, this approach allows a remarkably simple construction for the optical probe. Its 3D volumetric scanning capability can be combined with other developed handheld devices as well. Therefore, this manual is a flexible approach that particularly suitable for imaging guidance for relatively large

surgical site.

Mechanical scanning is a practical and mature method and has been applied to some ophthalmic procedures with more applications to be explored. In this capacity, we developed a type of forward-imaging probe, termed as PARS. To better learn its behavior, we studied the scanning pattern in a great detail. Theoretical modeling, software simulation, and experimental measurement have been carried out and results agree well with each other. We also designed a new generation hand-held PARS probe with diameter ranging 21-23 gauge, which is one step closer to the clinical application. We have applied our prototype PARS probe to locate the collector channel to assist in glaucoma stent implantation. Clear images with quantitative structure information were obtained. We also used this probe to examine the vitreous remnant during live animal vitrectomy and results were promising.

Besides the previous two categories, we devised and demonstrated a novel scanning without any moving parts involved. This approach is based on the space-charge-controlled EO effect in KTN crystal. As the scanning is virtually achieved by the motion of electron, the speed is much faster. It also avoids complex mechanical parts, enabling smaller and lighter devices. Without moving parts, it makes many surgical applications safer. More importantly, it has random access capability, which might be the best fit for diagnostic and therapeutic combined applications. Thus, scanning based on the EO effect is a high speed method with no moving parts, towards to the future of many endoscopic clinical applications.

7.2 Future Studies

The resolution of the hand-held probe based on tracking can be improved by increasing the frame rate of the tracking system. Some different variants of POSIT algorithm can be implement to compare their performances.

For the PARS probe, we can explore volumetric scanning by employing different rotating modes. And faster speed (¿10 frames/s) for video rate operation is also well desired. Combining the probe with other intraoperative surgical tools is also very beneficial to surgeons. Besides technology development, more applications, such as orthopedics, are waiting to be explored.

The non-moving KTN scanning has a great promise for the future endoscopic probes. More works on integrate this crystal into an endoscopic setting need to be carried out. Focuses will be at issues like electrical isolation for safety concerns, temperature stabilization for maintaining crystal phase. We can also explore the versatility of this device by employing different voltage modulation to achieve different scanning pattern. More interesting applications would be those use OCT imaging to locate target and use the random access feature to aim at it for later treatment.